CERN 2000-008
28 July 2000
Proton Synchrotron
Division

ORGANISATION EUROPEENNE POUR LA RECHERCHE NUCLEAIRE
CERN-EUROPEAN ORGANIZATION FOR NUCLEAR RESEARCH

A 3 TeV e^+e^- Linear Collider Based on CLIC Technology

CLIC

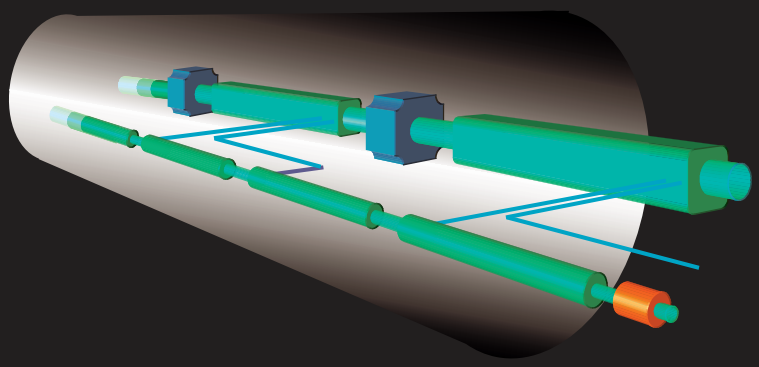

The CLIC Study Team

Editor:
G. Guignard
GENEVA 2000

ISSN 0007–8328
ISBN 92–9083–168–5

CERN 2000–008
28 July 2000
Proton Synchrotron
Division

ORGANISATION EUROPÉENNE POUR LA RECHERCHE NUCLÉAIRE
CERN EUROPEAN ORGANIZATION FOR NUCLEAR RESEARCH

A 3 TeV e^+e^- LINEAR COLLIDER BASED ON CLIC TECHNOLOGY

The CLIC Study Team

R.W. Assmann, F. Becker, R. Bossart, H. Burkhardt, H. Braun, G. Carron, W. Coosemans, R. Corsini, E.T. D'Amico, J.-P. Delahaye, S. Doebert, S. Fartoukh, A. Ferrari, G. Geschonke, J.-C. Godot, L. Groening, G. Guignard (Editor), S. Hutchins, J.-B. Jeanneret, E. Jensen, J. Jowett, T. Kamitani, A. Millich, O. Napoly[1], P. Pearce, F. Perriollat, R. Pittin, J.-P. Potier, A. Riche, L. Rinolfi, T. Risselada, P. Royer, T. Raubenheimer[2], F. Ruggiero, R. Ruth[2], D. Schulte, G. Suberlucq, I. Syratchev, L. Thorndahl, H. Trautner, A. Verdier, I. Wilson, W. Wuensch, F. Zhou and F. Zimmermann

1. Saclay, France
2. SLAC, Stanford, USA

GENEVA
2000

CERN–Service d'information scientifque–RD/1004–1500–juillet 2000

Abstract

A possible design of a multi-TeV e^+e^- linear collider is presented. The design is based on the CLIC (Compact LInear Collider) two-beam technology proposed and developed at CERN. Though the study has shown that this technology is applicable to a linear collider with centre-of-mass energies from 500 GeV or less up to 5 TeV, the present report focuses on the nominal energy of 3 TeV. First, a short overview is given of the physics that could possibly be done with such a collider. Then, the description of the main-beam complex covers the injection system, the 30 GHz main linac, and the beam delivery system. The presentation of the RF power source includes the beam-generation scheme, the drive-beam decelerator, which consists of several 625 m long units running parallel to the main linac, and the power-extraction system. Finally, brief outlines are given of all the CLIC test facilities. They cover in particular the new CLIC test facility CTF3 which will demonstrate the feasibility of the power production technique, albeit on a reduced scale, and a first full-scale single-drive-beam unit, CLIC1, to establish the overall feasibility of the scheme.

External Collaborations

The CLIC study team would like to acknowledge the very many important contributions made to the CLIC study over the years by collaborators from external laboratories. Many of them spent time at CERN as visitors working day-by-day with the CLIC study members, others worked with the team remotely from their home institutes.

Institutes that have in the past, or that are presently collaborating with the CLIC study team, are as follows: Berlin Technical University (Germany), CESTA (France), Daresbury (U.K.), DESY (Germany), INFN/LNF (Italy), Jefferson National Laboratory (USA), JINR and IAP (Russia), KEK (Japan), LAL (France), LLBL/LBL (USA), MIT (USA), RAL (U.K.), Royal Institute Technology, Stockholm (Sweden), SLAC (USA).

Contents

1 General Introduction

1.1 Prospects for physics[1]

As at other accelerator laboratories, the top priorities at CERN in the 21st century will be experiments probing beyond the Standard Model [1.1]. Indeed, this is surely the only responsible motivation for major new accelerators.

Problems beyond the Standard Model may conveniently be gathered into three major classes: those of *Mass, Unification* and *Flavour*. What is the origin of the particle masses, are they due to a Higgs boson, and, if so, why are they so small, perhaps because of supersymmetry? Is there a simple group framework containing the strong, weak and electromagnetic gauge interactions, and does it predict new observable phenomena such as proton decay and neutrino masses? Why are there so many types of quarks and leptons, and how can one understand their weak mixing and CP violation, perhaps because they are composite or have extra symmetries?

There are good reasons to expect a wealth of new physics in the TeV range, in particular that connected with the origin of particle masses. This new physics might include an elementary Higgs boson, but most physicists would expect the new physics to be more complex, perhaps including new spectroscopy of supersymmetric particles or other excitations.

The first exploration of the TeV energy range will be made with the Large Hadron Collider (LHC), and what it will find cannot be foreseen. However, it is impossible to expect that experiments at the LHC will actually answer all the questions concerning this new physics. For example, research physicists are likely to want more information about any kind of Higgs boson than what the LHC can tell us. Moreover, if Nature chooses supersymmetry, it can be expected that the LHC will reveal a number of supersymmetric particles but not all of them. And if Nature chooses to replace an elementary Higgs boson by new strong interactions, the hints that the LHC would provide should be followed up by other experiments.

Many of the open questions may best be addressed by a lepton–antilepton collider. All the centre-of-mass energy may be made available for the elementary-particle collisions, the experimental environment is relatively clean and all quanta with electroweak interactions are produced democratically with similar cross-sections. An example of the complementarity between hadron collisions and lepton collisions has been provided by the SPS proton–antiproton collider, in which the $W^{\pm}$ and Z^0 bosons were discovered, and LEP, which made possible precision measurements of their properties and tests of the standard electroweak theory.

Various laboratories are proposing electron–positron colliders with centre-of-mass energies between 0.5 TeV and 1 TeV. These would be able to explore in detail the properties of any relatively light Higgs boson and have a chance of producing lighter supersymmetric particles, but would probably not be able to explore all the supersymmetric spectrum, nor study in detail any new strong interactions. Complete coverage of these issues, and hence full complementarity with the LHC, probably requires a lepton–antilepton centre-of-mass energy of 2 TeV or more.

The technology required to collide electrons and positrons at energies ranging from 0.2 TeV (for some overlap with LEP) up to a maximum of approximately 5 TeV (in stages) has been developed within the CLIC study, at CERN and elsewhere, and a road map has been drawn up for completing within several years the R&D necessary to establish the possibility of an e^+e^- collider with E_{CM} of the order of 3 TeV. The alternative of colliding muons and antimuons is also being explored. In particular, CERN is conducting studies of the intense proton source that would be needed for such a muon collider, as well as aspects of the production and capture of muons, aimed at establishing the feasibility of a neutrino factory based on muon storage rings. Bringing muons into collision would, however, require additional R&D on cooling and other issues, so construction of any muon collider is likely to be on a longer time-scale than the Compact LInear Collider (CLIC).

A preliminary list of key CLIC physics processes to be studied is given in Table 1.1. This Table shows the clear complementarity between the physics prospects for the LHC and CLIC. In particular, CLIC has unique prospects for new electroweakly-interacting particles. Some preliminary studies of CLIC physics have already been made. The design of CLIC has now reached the stage where more detailed studies are required, in particular of the interface between the beam delivery system and the experimental area. It is also important to be satisfied that the CLIC beam-energy spread, initial-state radiation and beamstrahlung permit experimental investigation of the full richness of the available physics. Table 1.2 shows a list of benchmark physics processes that are now being studied in greater detail by the CLIC Physics Study Group [1.2]. In each case, the most important challenges offered by the CLIC environment are noted.

---

1. Section written by J. Ellis, CERN.

Table 1.1: A comparison of some of the capabilities of the LHC and CLIC at the high-energy frontier. Note the instances where photon beams (γ) and polarization (P) might be advantages for CLIC.

Physics topics	**LHC**	**CLIC**
Supersymmetry		
Heavy Higgses H, A	No?	Yes: γ
Sfermions	$\tilde{q}$	$\tilde{\ell}$
Charginos	No?	Yes: P
SUSY breaking	Some	More
Strong Higgs sector		
Continuum	< 1.5 TeV	< 2 TeV
Resonances	Scalar, vector	Vector, scalar
Extra dimensions		
Missing energy	large E_T	Yes
Resonances	q*, g*	γ*, Z*, e*

Table 1.2: Examples of benchmark physics processes for CLIC

Physics channel	**CLIC challenges**
Heavy Higgs H^0	Luminosity
Strong symmetry breaking	$\gamma\gamma$ bkg, hermiticity
Anomalous W couplings	$\gamma\gamma$ bkg
$e\ \bar{\nu}\ W$	$\gamma\gamma$ bkg
Heavy (H^0, A^0, $H^{\pm}$) Higgses	($dL/d\sqrt{s}$), pairs, $R_{\text{beam-pipe}}$
SUSY $\tilde{g}$, $\tilde{q}$	$\gamma\gamma$ bkg, hermeticity, $R_{\text{beam-pipe}}$
$\tilde{\chi}^+\tilde{\chi}^-$	$\gamma\gamma$ bkg, hermeticity
$\tilde{\ell}^+\tilde{\ell}^-$	($dL/d\sqrt{s}$), hermeticity
Contact interactions	$\sqrt{s}$, L
Z′ (M ≤ 3 TeV)	($dL/d\sqrt{s}$), L
Z′ (M > 5 TeV)	Pairs, $R_{\text{beam-pipe}}$
Extra dimensions	$\gamma\gamma$ bkg, hermeticity

For each of these processes, the first question is whether a process is observable. The second question is how accurately it can be measured, e.g., at threshold.

One of the main issues is the spread in centre-of-mass collision energies at CLIC. This involves two components: the intrinsic beam energy spread and the spread induced by Initial-State Radiation (ISR) and beamstrahlung. The former is essentially Gaussian, whereas the latter has a long 'tail' down to large energy losses. Another issue is how well the beam energy can be calibrated. Among the physics topics where these effects are important are the following.

– *An s-channel resonance, such as a Z′*
If this Z′ decays only into Standard Model particles, one expects that

$$\frac{\Gamma_{Z'}}{m_{Z'}} \sim \frac{\Gamma_Z}{m_Z} \ ,$$

with a modest increase due to the accessibility of $Z' \to \bar{t}t$ decays. In this case, one might expect that the beamstrahlung spread would not be so important, but that the knowledge of the beam energy spread and its calibration error would be.

– *An S-wave threshold for pair production of some new particle species*

Here the situation may depend upon whether the event has missing energy or not. In the latter case, one might again guess that the beamstrahlung spread would not be so important, but that calibration of the beam energy and its intrinsic spread would be. In the missing energy case, the beamstrahlung energy loss might also be important.

– *A P-wave threshold for pair production of some new particle species*

Examples without missing energy include charged-Higgs pair production, associated production of scalar and pseudoscalar Higgses h or H + A in the MSSM, and an example with missing energy could be pair production of smuons $\tilde{\mu}$. In these cases, the beamstrahlung energy loss might be relatively more important.

– *Associated production of Z + H*

A new issue here is the finite decay width of the Z and/or H. The beam energy spread could be important here, beamstrahlung less so.

– W^+W^- *fusion processes, in particular heavy Higgs production*

Here one would need to understand the roles of missing p_T and p_L. In this connection, one could expect that beamstrahlung would be important.

An important set of issues concerns the hermiticity of the possible detector, particularly in the forward and backward regions. The dead angle θ around the beam pipe is critical for several physics processes, for example for measurements of processes with missing energy, such as $\tilde{\mu}$ pair production. The resolution in p_T is

$$\Delta p_T \sim \theta \, E_{CM}$$

where θ is a dead angle around the beam axis. It will be necessary to understand the physics loss as a function of this dead angle.

These detailed studies are currently under way, but, on the basis of preliminary physics studies already made, one may anticipate that CLIC will be able to complete the exploration of TeV-scale physics that the LHC initiates.

1.2 Overview of the linear collider

A high-energy (0.5–5 TeV centre-of-mass), high-luminosity (10^{34}–10^{35} $cm^{-2}s^{-1}$) e^+e^- Compact LInear Collider (CLIC) is being studied at CERN [1.3], [1.4] as a possible new high-energy physics facility for the post-LHC era [1.5]. The general parameters and an overall layout are given in the Appendix. The maximum energy of 5 TeV is well above those presently being proposed by other linear collider studies. The physics experiments require a luminosity of at least 10^{34} cm^{-2} s^{-1} at 1 TeV c.m. and this luminosity should increase at higher energies [1.4]. Although the design study has been optimized for 3 TeV centre of mass, the collider could start operation at a lower energy and then be upgraded in stages. The design is such that these upgrades can be made without major modifications. CLIC is based on the Two-Beam Acceleration (TBA) method in which the RF power for sections of the main linac is extracted from a secondary, low-energy, high-intensity electron beam running parallel to the main linac. The power is extracted from the beam by special Power Extraction and Transfer Structures (PETS). For a 3 TeV collider, there are 22 such drive-beams, each of which provides enough power to accelerate the main beam by ~70 GeV. All the drive-beams are generated in a centrally located facility. The only difference between the drive-beam generation schemes for high and low colliding beam energies is the length of the modulator pulse (the installed hardware is exactly the same). This means that the entire drive-beam generation system has to be installed in the first stage. The overall layout of CLIC is sketched in Fig. 1.1. Two interaction points (IPs) are foreseen, one for e^+–e^- and one for γ–γ. For a c.m. energy of 3 TeV and an accelerating gradient of 150 MV/m, and allowing ~10 km for the Beam Delivery (BD) area, CLIC would cover a total length of approximately 38 km. The generation, acceleration and delivery of the main beams (see the upper half of Fig. 1.1) and the micro-alignment system are described in Section 2. The drive-beam complex, and the production of 30 GHz RF power (see the lower half of Fig. 1.1) is presented in Section 3. Sections 4 and 5 are devoted, respectively, to machine protection questions, and to the CLIC test facilities which are intended to demonstrate the feasibility of the TBA scheme.

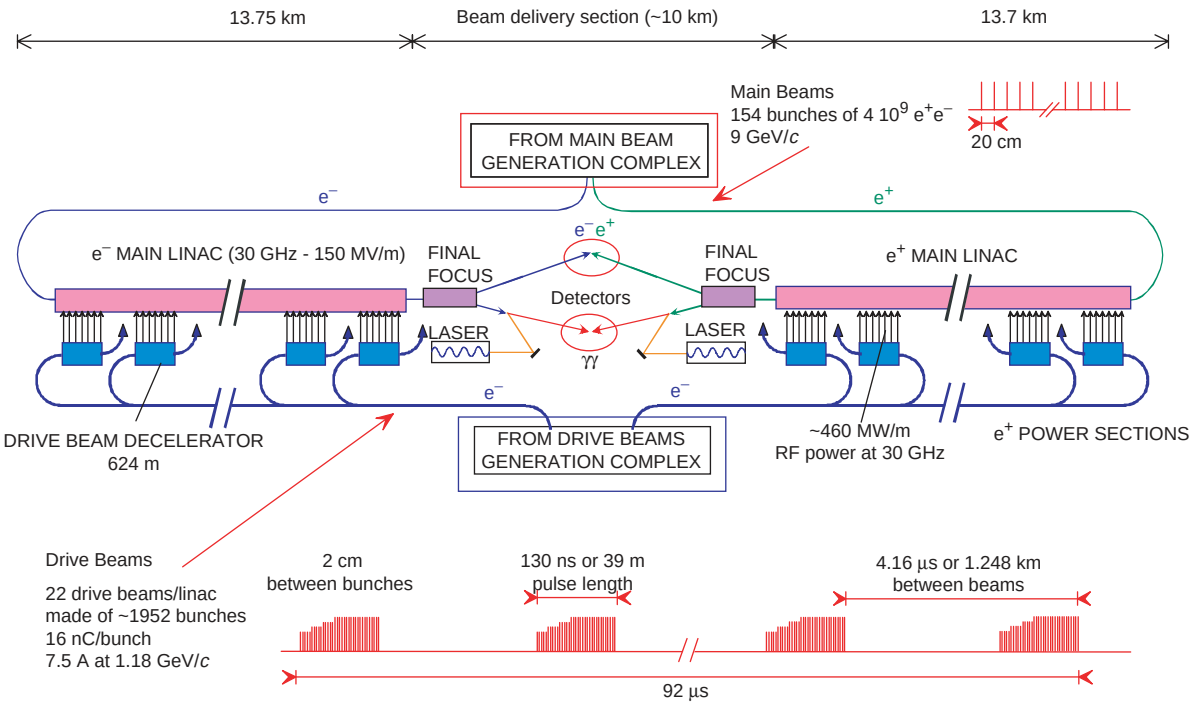

Fig. 1.1: *Overall layout of CLIC for a centre-of-mass energy of 3 TeV.*

A big advantage of the TBA scheme is that, since there are no active components such as modulators or klystrons, both linacs can be housed in a single small-diameter tunnel. This results in a very simple, cost-effective and easily extendable arrangement (Fig. 1.2). The tunnel cross-section shows the two linacs installed on a common concrete base. The various transfer lines fixed to the roof carry the main- and drive-beams from the generation complexes to their respective injection points (Fig. 1.1).

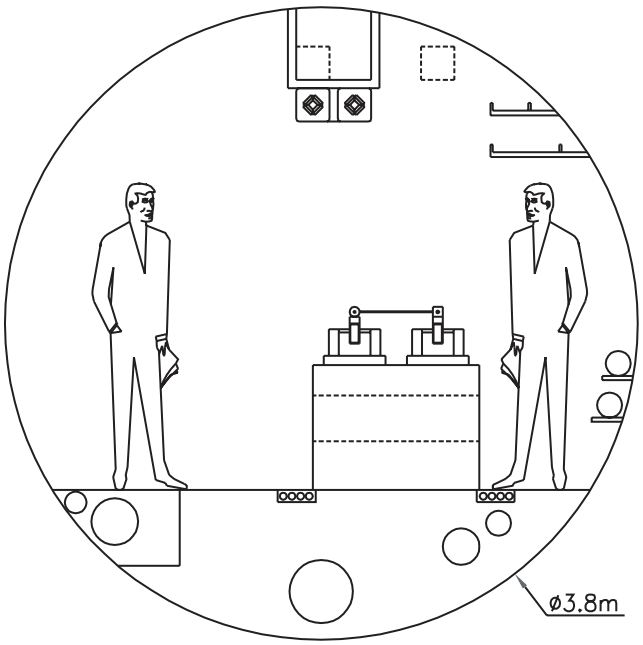

Fig. 1.2: *CLIC tunnel cross-section.*

Among the different tehcnological ways of building a linear collider, the CLIC study explores the technical feasibility of two-beam acceleration using high-frequency, room-temperature, travelling-wave structures. A high RF frequency has been chosen in order to be able to operate at a high accelerating gradient which reduces the length, and in consequence, the cost of the linacs. The choice of 30 GHz is considered to be close to the limit beyond which standard technology for the fabrication of accelerating structures can no longer be used. The main drawback of

operating at a high RF frequency is that the accelerator iris aperture is very small (~4 mm), leading to the generation of strong wakefields and the related dilution of the transverse emittance. The effects of these strong wakefields can be minimized by a judicious choice of beam and linac parameters. These parameters have been optimized using general scaling laws derived from linear collider studies covering more than a factor 10 in frequency [1.6]. The optimization uses a figure of merit *M,* defined at a given energy as the luminosity normalized by the beamstrahlung parameter δ_B and the wall-plug power consumption P_{AC}. In the low-beamstrahlung regime (Y<<1, Y being the critical photon energy normalized to the beam energy), the factor *M* depends only on the mains-to-beam power transfer efficiency η_b^{AC} and the vertical normalized emittance ε_{ny}^* at the IP. In the high-beamstrahlung regime (Y>>1), the factor *M* depends, in addition, on the (r.m.s.) bunch length σ_z. To obtain stable beam operation with an infinite number of bunches, and to minimize the energy spread at the end of the linac, the charge per bunch and the bunch length must be scaled with RF frequency $\omega/2\pi$, mean-loaded gradient G_a and initial normalized emittance ε_{ny0} (before blow-up) like [1.6]

$$N_b \propto \omega^{-6/5} G_a{}^{2/3}\, \varepsilon_{ny0}{}^{1/3} \quad \text{and} \quad \sigma_z \propto \omega^{-2/3} G_a{}^{-1/3}\, \varepsilon_{ny0}{}^{1/3}\,.$$

For CLIC at 30 GHz this gives $N_b = 4 \times 10^9$ and $\sigma_z = 30\ \mu m$. After fixing these two quantities, the RF-to-beam transfer efficiency η_b^{RF} is optimized (assuming a large number of bunches) by adjusting the field attenuation constant τ via the accelerating structure length L_{st}, according to the following law and its corollary

$$\tau_{opt} \propto \omega^{-1/15} G_a{}^{1/3} \varepsilon_{ny0}{}^{-1/3} \quad \Rightarrow \quad \eta_b^{RF} \propto \omega^{1/30} G_a{}^{-1/6} \varepsilon_{ny0}{}^{1/6}\ ,$$

which makes η_b^{RF} nearly independent of the accelerating gradient and of the RF frequency. This optimum corresponds to $\tau_{opt} = 0.675$ and $L_{st} = 0.5$ m. In spite of the reduced charge per bunch and of the high gradient, the efficiency remains high because the time between bunches is small and the shunt impedance of the structure is high. In addition, the effects of the wakefields and the consequent beam emittance blow-up are effectively made independent of the frequency with the chosen values of N_b, σ_z and τ. At higher frequencies this requires stronger focusing, tighter alignment tolerances of the cavities and position-monitors, and a sufficiently large momentum spread for BNS damping[1] [1.7].

At 3 TeV, in the high-beamstrahlung regime (Y>>1) which, if the other parameters are kept constant, gives a larger luminosity, then both the factor of merit and the total luminosity increase with ω but are independent of G_a, according to Ref. [1.6]

$$M = \frac{L}{P_{AC}} \frac{U_f^{1/2}}{\delta_B^{3/2}} \propto \frac{\eta_b^{RF}}{\sigma_z^{1/2} \left(\varepsilon_{ny}^*\right)^{1/2}} \propto \frac{\omega^{1/3}}{\varepsilon_{ny0}^{1/2} \left(1 + \Delta\varepsilon_{ny}/\varepsilon_{ny0}\right)^{1/2}} \quad \text{and} \quad L \propto \frac{\omega^{1/3} P_{AC}}{\left(\beta_y^*\right)^{1/2} (\varepsilon_{ny0} + \Delta\varepsilon_{ny})^{1/2}}$$

where U_f is the final energy of the main beam, L the luminosity and β_y^* the vertical betatron amplitude at the IP.

Hence, limiting the power consumption at 3 TeV requires operating CLIC with Y>>1 and with an extremely low vertical (normalized) beam-emittance which implies a very small growth of this emittance during acceleration. The other important beam parameters are deduced from constraints in the interaction region. The horizontal beam size at the IP is adjusted to get a good trade-off between the total luminosity and the fractional luminosity near the nominal c.m. energy. The vertical beam size is limited by the synchrotron radiation and the chromaticity generated in the IP quadrupole doublets. These conditions on the spot size and beam optics considerations determine the betatron-function amplitudes at the crossing point and in consequence the precise values of the emittances. With such modest bunch charges, the only way to obtain the specified high luminosity is to operate in a multibunch mode and at a repetition rate of the order of 100 Hz. The resulting main-beam and linac parameters corresponding to CLIC at 3 TeV c.m. are listed in Table 1.3.

1. Termed after the names of the authors of the method.

Table 1.3: Main-beam and main-linac parameters for CLIC at 3 TeV c.m.

Main-beam parameters at IP		
Luminosity (with pinch)	L	10.0×10^{34} cm^{-2} s^{-1}
Luminosity (in 1% of energy)	$L_{1\%}$	3.0×10^{34} cm^{-2} s^{-1}
Beamstrahlung mom. spread	δ_B	31%
Beamstrahlung parameter	Υ	8.1
Number of photons/electron	N_γ	2.3
Number of particles/bunch	N_b	$4.0 \times 10^9 e^\pm$
Number of bunches/pulse	k_b	154
Bunch spacing	Δ_b	20 cm
	Δt_b	0.666 ns
Transverse emittances	$\gamma\varepsilon_{x/y}$	680/20 nm·rad
Beta functions	$\beta_{x/y}$	8/0.15 mm
r.m.s. beam size (no pinch)	$\sigma_{x/y}$	43/1 nm
Bunch length	σ_z	30 μm
Enhancement factor	H_D	2.24
Beam power per beam	P_b	14.8 MW
Main-linac parameters		
Centre-of-mass energy	E_{CM}	3 TeV
Linac repetition rate	f_{rep}	100 Hz
RF frequency of linac	$\omega/2\pi$	30 GHz
Acceleration field (loaded)	G_a	150 MV/m
Energy overhead		8%
Active length per linac	L_A	10.74 km
Total two-linac length	L_{tot}	27.5 km
RF power at structure input	P_{st}	229 MW
RF pulse duration	Δt_p	102 ns
Number of drive-beams/linac	N_D	22
Number of structures per linac		21 470
AC-to-RF efficiency	η_{RF}^{AC}	40.3%
RF-to-beam efficiency	η_b^{RF}	24.4%
AC-to-beam efficiency	η_b^{AC}	9.8%
AC power for RF production	P_{AC}	300 MW

References

Prospects for physics (Section 1.1)

[1.1] J. Ellis, Physics goals of the next century at CERN, CERN-TH-2000–050 (2000).

[1.2] The Physics Study Group for CLIC, http://clicphysics.web.cern.ch/CLICphysics/

Overview of the linear collider (Section 1.2)

[1.3] J.-P. Delahaye et al., The CLIC study of a multi-TeV e^+e^- linear collider, Proc. Part. Accel. Conf. (PAC99), New York, 1999, Eds. A. Luccio and W. MacKay (IEEE Computer Soc. Press, Piscataway, N. J., 1999). http://preprints.cern.ch/cgi-bin/setlink?base=preprint&categ=cern&id=ps-99-005

[1.4] International Linear Collider Technical Review Committee Report, Ed. G. Loew, SLAC-R-95–471 (1995). http://www.slac.stanford.edu/pubs/slacreports/slac-r-471.html

[1.5] J. Ellis, E. Keil and G. Rolandi, Options for future colliders at CERN, CERN-EP/98–03, CERN-SL 98–004 (AP) and CERN-TH/98–33 (1998). http://preprints.cern.ch/cgi-bin/setlink?base=preprint&categ=cern&id=SL-98-004

[1.6] J.-P. Delahaye, G. Guignard, T. Raubenheimer and I. Wilson, *Scaling laws for e^+/e^- linear colliders,* Nucl. Instrum. Methods Phys. Res. **A 421** (1999) 369–405. http://preprints.cern.ch/cgi-bin/setlink?base=preprint&categ=cern&id=PS-97-051

[1.7] V.E. Balakin, A.V. Novokhatsky and V.P. Smirnov, VLEPP: transverse beam dynamics, Proc. 12th Int. Conf. on High Energy Accel., Fermilab, 1983, p. 119.

2 Main-Beam Generation, Acceleration and Delivery

2.1 Introduction

As explained in the general introduction, a single tunnel will house both linacs which sit on the same supporting block (Fig. 1.2). The work carried out on the micron-displacement system for the main linac is based on the principle that support girders are installed on micro-movers which in turn lie on the concrete block. The ends of two adjacent girders are on a common platform which assures continuity of position between units that form a string. Four accelerating structures, fixed to the girder via V-supports, are mounted on each girder. At the front of each girder there is a beam-position monitor for beam-based correction of the trajectory. This arrangement defines the 2.23 m long basic module of the main linac. Since the drive-beam runs parallel to the main linac and must regularly power two accelerating structures from one decelerating structure, the main-linac module defines the length of one drive-linac module. The latter includes two decelerating structures and two quadrupoles forming a FODO cell. Figure 2.1 gives a sketch of the module layout for both linacs.

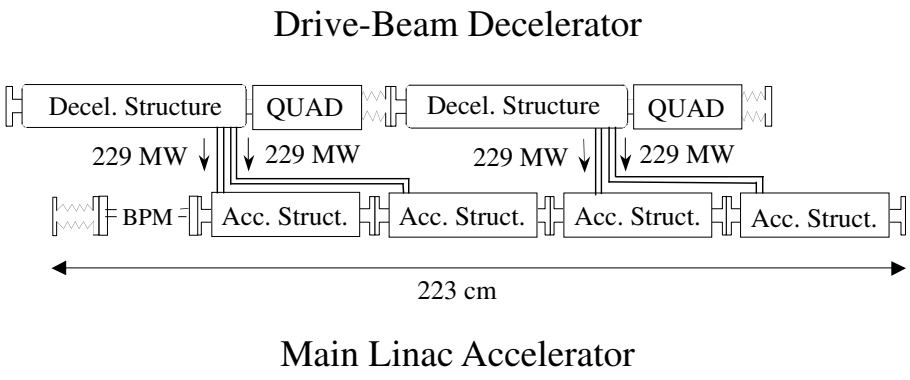

Fig. 2.1: *One basic main-beam module and one drive-beam module.*

The main linac contains more than 6300 of these modules, most of them supporting the four structures indicated on Fig. 2.1. However, since the beam has to be focused, some structures are removed at regular intervals to liberate space for the quadrupoles of a FODO lattice. As in most linear collider designs, the focusing is scaled with the energy such as to keep the stability margin by BNS damping approximately constant and this is done by linac sectors, with, however, a regular lattice in each sector. Hence, in many main-beam modules of the type sketched in Fig. 2.1, between one and a maximum of four structures are replaced by a quadrupole of corresponding length and these particular modules are separated by a variable number of basic modules, depending on the sector considered. All these quadrupoles are supported independently of the string of girders and their positions are optimized by using the signals from the beam-position monitors.

High luminosity implies small normalized emittances, in particular in the vertical plane. Therefore, a specific design of the damping rings is necessary, based on the 'Theoretical Minimum Emittance' lattice and straight sections equipped with wiggler magnets. The beam energy in these rings (1.98 GeV) results from considerations about the use of polarized beams, damping times, and intrabeam scattering. The energy is then increased in a booster linac operating at 3 GHz, a frequency at which the effects of the wakefields on the emittance are reduced with respect to those expected in 30 GHz structures. Taking into account the beam stabilization in the main linac by BNS damping and trajectory correction, an injection energy of 9 GeV has been selected as a reasonable balance of the contributions to emittance growth of the booster linac and main linac in the low-energy region. However, the emittance control in the booster linac has not yet been studied and the related results could lead to a modification of the booster-linac operating frequency and of the energy of injection into the main linac. The main effort was put on the most critical question of the preservation of the normalized emittances in the main linac and detailed simulations were done to study it. Numerical and graphical data are often given only for the vertical emittance which is much smaller than the horizontal one. Present results indicate that the emittances can be well controlled by using correction and adjustment techniques which are feasible. For other areas of the beam transport and acceleration, such as the booster linac, the transfer lines and the beam delivery system (BDS), there are educated guesses of the emittance growths, based on other studies or preliminary investigations. However, additional potential sources of blow-up, which are likely less critical and have not yet been analysed, are not included. The current estimates of the emittance growths at different locations in the linear collider are summarized in Table 2.1.

Table 2.1: Transverse normalized-emittance estimated growths at different stages of acceleration, transfer and delivery

Places where the emittance growth occurs	**Horizontal $\Delta\gamma\varepsilon_x$ [nm·rad]**	**Comments on $\Delta\gamma\varepsilon_x$**	**Vertical $\Delta\gamma\varepsilon_y$ [nm·rad]**	**Comments on $\Delta\gamma\varepsilon_y$**
Blow-up in beam delivery system	35	Total blow-up in BDS assumed to be about 5%	2	Total blow-up in BDS assumed to be about 10%
Blow-up in the main linac	25	After several static corrections	1	After several static corrections
	6	$\Delta\gamma\varepsilon_x$ **per day,** due to time-dependent effects	1	Blow-up due to jitter of injection and quadrupoles
		(Both associated with wakefields and misalignments)	1	$\Delta\gamma\varepsilon_y$ **per day,** due to ground motion effects (wakefields, noise and misalignments)
Blow-up in the transfer lines, booster linac and bunch compressor	60	Synchrotron radiation in turn-round & compressor	1	Wakefields in booster linac
	40	Booster linac from 2 to 9 GeV and transfer lines	1	Scattering and ion trapping in transfer lines

Table 2.2: Longitudinal phase-space parameters at different stages of compression and acceleration

Location	**Energy spread $\Delta E/E$ [%] Uncorrel. Correl.**	**Comments**	**Bunch length σ_z [mm]**	**Comments**
At the IP	Negligible 1	Total width of the energy distribution given by the FF acceptance	30	r.m.s. bunch length at the collision
At the exit of the main linac	Negligible 0.35	r.m.s. energy-spread (change of ϕ_{RF} before exit). Total < ± 0.5%	30	
In the main part of the linac	Decreasing 0.55 with E	r.m.s. correlated energy spread for BNS damping. (Uncorrelated energy spread is negligible after accel.)	30	
At the linac entrance	Negligible	Correlated energy spread at injection	30	Bunch length after the second compression
	1.8	Max. uncorrelated energy spread at injection, after total bunch compression		
Bunch compressor	0.22 Negligible	E-spread at 2nd compressor entrance (9 GeV)	250	Bunch length after the first compression
	0.98 Negligible	E-spread at 1st compressor exit (2 GeV)	250	
At the exit of the damping ring	0.07 Negligible	E-spread required in D.R. to keep $\Delta E/E$ < 1.8% in the main linac	3000	Bunch length expected at the D.R. extraction

Considering the absolute normalized emittances, the calculated values corresponding to the target luminosity of Table 1.3 are 680 nm·rad and 20 nm·rad in the horizontal and vertical case, respectively. The ratio of 34 is adjusted in order to balance the total luminosity versus the luminosity in 1% of energy and to control the background. The vertical value of 20 corresponds to a beam size of 1 nm at the IP. In the actual design of the final focus, however, achieving this beam size in the presence of the beam energy-spread and chromatic correction might require an even smaller vertical emittance. At the injection of the main linac, a $\gamma\varepsilon_y$ as small as 5 nm·rad has been assumed as a starting point for the study, i.e. of the same order as the expected blow-up in the linac for a three-day period (see Table 2.1), while $\gamma\varepsilon_x$ is between 550 and 600 nm·rad. This means that the total effective emittance and the vertical one should be in this case as small as 450 and 3 nm·rad at the exit of the damping rings. It is not known today if these extremely low values can actually be delivered, since the design of the damping rings is not advanced enough. However, comparing the target emittances at the IP, their assumed values at the damping ring exit, and the expected blow-ups, there is a margin of the order of 50 nm·rad horizontally and 8 nm·rad vertically. These margins account for the possibly larger emittances at the damping ring extraction (coupling, intrabeam scattering, non-linearities, etc.), the needs for a smaller vertical emittance in the IP (see the argument above), and the neglected sources of perturbations.

In the longitudinal phase-space, the evolution of the parameters is summarized in Table 2.2. These figures take into account the bunch compression-rate required, the maximum uncorrelated energy-spread acceptable at the main linac injection, and the correlated energy-spread necessary for emittance preservation in the linac. They assume in addition isochronous achromatic bends in the transfer lines, whose residual effects on the bunch-length are currently neglected.

2.2 Injection system

2.2.1 Basic parameters

The bunch spacing in the main-beam train imposes an RF acceleration frequency of 1.5 GHz. The RF guns and all the linacs are L-band except the Booster Linac which is S-band. The particle production is 61.6×10^{12} $e^{\pm}$/s, with the present parameters. A total incoherent energy spread of $\Delta E/E = \pm 1\%$, for the L-band pre-injector, corresponds to a maximum r.m.s. bunch length of $\sigma_z = 3$ mm. The same bunch length is assumed from the RF gun up to the first bunch compressor located downstream from the damping ring. Two stages of bunch compressors are foreseen (Section 2.2.5). The first, at the damping ring exit, works at 3 GHz while the second, at the entrance of the main linac, works at 30 GHz.

The normalized transverse beam emittances at the IP are imposed by the luminosity, and their expected growths are given in Table 2.3. The damping rings have to be designed to cope with the emittances consequently requested at the ring extraction, given the maximum emittances provided by the lepton sources. The maximum single-bunch charge is 5% higher than the charge at the IP in order to allow for beam losses in the injector complex and collimation at the entrance of the main linac. Table 2.3 summarizes the CLIC injector basic parameters.

Table 2.3: Injector basic parameters at different stages

General parameters	
At main linac injection	
Energy	9 GeV
No. of particles per bunch	0.42×10^{10} $e^{\pm}$
Bunch length	30 mm
Energy spread	1.8%
Transverse emittance (ε_x)	600 nm·rad
Transverse emittance (ε_y)	$5 \leq \varepsilon_y \leq 13$ nm·rad
At damping ring exit	
Energy	1.98 GeV
No. of particles per bunch	0.42×10^{10} $e^{\pm}$
Bunch length	3000 mm
Energy spread	0.082%
Transverse emittance (ε_x)	450 nm·rad
Transverse emittance (ε_y)	$3 \leq \varepsilon_y \leq 11$ nm·rad

General parameters	
At damping ring entrance	
No. of electrons per bunch	0.5×10^{10}
No. of positrons per bunch	0.64×10^{10}

2.2.2 Overall injection complex

The general layout of the main-beam injection complex is given in Fig. 2.2. This complex is composed of two systems.

i) The electron production system:

The laser system and the photocathode RF electron gun generate a 10 MeV, low-charge beam. The pre-injector linac provides an energy gain of 190 MeV and an e^- beam energy at the exit of 200 MeV. The injector linac accelerates the beam by 1.78 GeV, giving a final energy of 1.98 GeV. This linac accelerates alternately the train of electrons and the train of positrons. A DC dipole magnet separates the e^- beam from the e^+ beam. It also allows the beam to be sent towards a dump where some beam instrumentation will be implemented. Then, there are, successively, the damping ring for e^-, the first stage of the bunch compressor working at 3 GHz and 1.98 GeV, the booster linac accelerating alternately e^- and e^+ beams up to 9 GeV, the transfer line, and finally the second stage of the bunch compressor working at 30 GHz and 9 GeV at the entrance of the e^- Main Linac.

ii) The positron production system:

The laser system and the photocathode RF electron gun generate a 10 MeV, high-charge beam. The e^- Primary Beam Linac sends a 2 GeV beam onto the e^+ target. Following the conventional positron source, which receives the high-intensity primary e^- beam, the e^+ Pre-injector Linac accelerates e^+ (and secondary e^-) up to 200 MeV. The injector linac (common to e^- and e^+) provides a 1.78 GeV energy gain. Then, follow the pre-damping ring and the damping ring for e^+. The rest of the system consists of the same kind of compressors and transfer lines as in the electron system and includes the common booster linac.

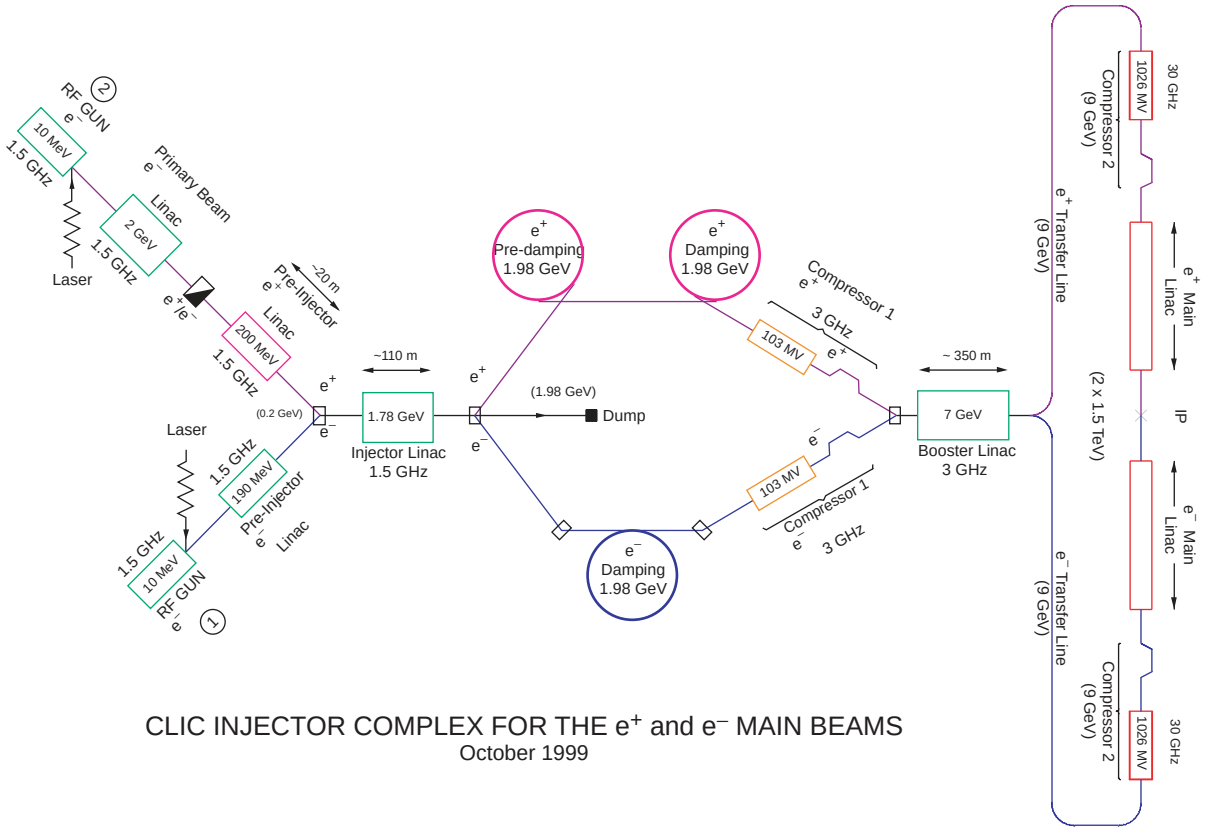

Fig. 2.2: *Sketch of the injection complex.*

2.2.2.1 Electron source for the main linac

The RF gun should produce 1 nC/bunch. The charge of 6.25×10^9 e^-/bunch takes into account the transfer efficiency between the RF gun, at 10 MeV, and the damping ring exit, at 1.98 GeV. A total charge of 154 nC is not an issue for an RF gun based on a Cs_2Te photocathode if one uses non-polarized electrons, but it should be studied for polarized electrons. The emittances scale approximately linearly with the charge for a given RF wavelength. At 1.5 GHz, the RF gun should work with an electric field of 50 MV/m. The expected normalized emittance [2.1] is between 4 and 7×10^{-6} rad·m (cylindrical symmetry).

The use of a second RF photo-injector, for the e^- beam, is envisaged. It will allow beam profile studies and could be used as a spare RF gun or as a polarized e^- source. The severe requirement on the vertical emittance of the electron damping ring could indeed be relaxed if the beam profile was shaped in order to get an asymmetric electron beam coming out from the photocathode.

Since CLIC also requires polarized electrons, they can be generated by using GaAs photocathodes and the SLC source is the reference, which is based on a DC gun with a GaAs photocathode. However, it has to be demonstrated that the electron beam characteristics required for CLIC are obtainable with the same technology. A review has been made of the polarized RF guns [2.2], but more work remains to be carried out in order to establish the feasibility of a polarized RF gun with the CLIC parameters.

2.2.2.2 Positron source for the main linac

Based on the assumptions developed in Ref. [2.1], the RF gun should deliver 2×10^{10} e^-/bunch. A linear scaling with the charge provides an emittance of 13×10^{-6} rad.m (both planes) for the 2.2 nC/bunch needed to create the train for positron production. The positron source for the CLIC is a conventional one based on an electromagnetic shower created by electrons impinging on a high-Z material target. The design takes into account the experience gained from the SLC source. The source and its associated 2 GeV linac meet the specifications for the 1 TeV option. The strategy developed for CLIC is explained in Ref. [2.1]. The radius of the incident electron beam is 1.6 mm (factor 2 compared to SLC) and the e^+ beam is accelerated at 1.5 GHz in a structure twice as large as that of the SLC with a uniform magnetic field in the solenoid. The normalized yield is 0.30 $e^+/e^- \times$ GeV at the exit of the e^+ pre-injector linac. The charge per bunch for the primary electron beam is 1.35×10^{10} e^-/bunch. The incoming e^+ emittances (edges) into the pre-damping ring are 0.06 rad.m in both planes. This value is based on ETRANS simulations [2.3].

A possibility to produce positrons by a channelling process is under development. However, the thermal and radiation effects due to the high-intensity incident electrons should not affect the crystal structure. Preliminary and encouraging results have been obtained with the SLC 30 GeV beam [2.4].

The maximum charge required for the positron production described above is 493 nC in 154 bunches. A quantum efficiency of 1.5% (at $\lambda = 262$ nm) on the photocathode implies a laser energy of 156 μJ at the same wavelength. The maximum charge required for the electron production (for the collisions) is a factor 3 smaller. The maximum charge produced, today, by a Cs_2Te photocathode, in CLIC Test Facility 2 (CTF2), is 750 nC in 48 bunches. Therefore for both photo-injectors of the CLIC injection complex the charge is not an issue.

The train-to-train and bunch-to-bunch charge jitters required must remain below 0.5% and 1% r.m.s., respectively. The transverse laser spot size on the photocathode should have a diameter variation smaller than 1%.

2.2.2.3 The linacs

Based on the NLC studies for the positron capture and beam loading compensation, the e^+ pre-injector linac (~20 m long) accelerates the particles up to 200 MeV with a loaded gradient of 24 MV/m and the energy at the end of the e^- pre-injector linac is the same. The energy gain in the e^- primary-beam linac is a free parameter that will be adjusted for a good trade-off between cost and efficiency. The injector linac (1.5 GHz) is based on a loaded gradient of 17 MV/m and is approximately 110 m long in order to accelerate both beams to 1.98 GeV. The Booster linac (3 GHz) has a loaded gradient of 21 MV/m and is approximately 350 m long in order to boost both beams up to 9 GeV. The RF pulse is 10 ms long and accommodates two consecutive SLED (compression system) pulses. The first is for e^+ acceleration and the second is for e^- acceleration.

2.2.3 Positron production

The yield at the exit of the e^+ pre-injector (200 MeV) is 0.59 e^+ per drive electron which is two times the maximum bunch intensity desired at the IP. The normalized yield, at 200 MeV, is 0.30 $e^+/e^- \times$ GeV. The e^+ target is 15.4 mm long. For $W_{75}Re_{25}$ material, it corresponds to 4.5 χ_0 (radiation length). The beam power on the target is

67 kW and the deposited energy 220 J. The 22 kW power deposited in the target corresponds to 33% of the beam power. The density in the CLIC target of $\approx 0.5 \times 10^{12}$ GeV/mm^2 is a factor 4 below the failure threshold due to single pulse heating, which is 2×10^{12} GeV/mm^2 for a $W_{75}Re_{25}$ target. However, according to the recent experience of SLC e^+ target failure, careful attention will be necessary in the design of the e^+ target. Two L-band sections are foreseen for the beam loading compensation. The positron collection system is based on the Adiabatic Matching Device (flux concentrator). For reasons of reliability and high level of radiations, a second e^+ source could be implemented near the first one, but with an independent access. Table 2.4 presents the CLIC parameters for the positron source and compares them to those of SLC and NLC.

Table 2.4: Positron source parameters for different linear collider studies

General parameters	**Unit**	**SLC**	**NLC**	**CLIC**
Centre-of-mass energy	TeV	0.1	1	1
No. e^+ per pulse at IP	10^{10}	3	99	62
No. of bunches per pulse	–	1	90	154
Pulse duration	ns	3000	126	140
Bunch spacing	ns	–	1.4	0.667
Repetition frequency	Hz	120	120	100
Primary beam				
Energy	GeV	30	6.22	2
No. e^- per bunch	10^{10}	3	1.5	1.35
No. e^- per pulse	10^{10}	3	135	208
Beam power	kW	17	161	67
Linac frequency	GHz	2.856	2.856	1.5
r.m.s. spot size on target	mm	0.8	1.6	1.6
Pulse energy density	10^{12} GeV/mm^2	0.52	1.04	0.5
Positron target				
Material	–	$W_{75}Re_{25}$	$W_{75}Re_{25}$	$W_{75}Re_{25}$
Thickness	χ_0	6	4	4.5
Energy deposition	J/pulse	–	188	220
Mean deposited power	kW	5	23	22
Capture system				
Adiabatic matching device	–	Yes	Yes	Yes
Energy acceptance	MeV	20	20	20
Wavelength of accel. RF	m	0.1	0.21	0.20
Minimum iris radius	mm	9	20	20
Accelerating gradient	MV/m	30	25	24
No. e^+ per bunch	10^{10}	8.7	3.1	0.8
Yield				
Yield at e^+ pre-injector exit (200 MeV)	$e^-/e^+ \times$ GeV	0.05	0.33	0.30

2.2.4 Damping rings

2.2.4.1 Introduction

The CLIC damping ring complex provides positron and electron bunch trains at a repetition period of 10 ms with a normalized emittance of 430 nm·rad in the horizontal and 3 nm·rad in the vertical plane (Table 2.5). For the positron beam, with a pre-accelerator normalized emittance of 42×10^6 nm·rad in both planes, the vertical emittance reduction will be a factor close to 10^7 which requires 10 damping times in order to have the beam emittances close to the equilibrium emittances of the ring, while the horizontal emittance will be reduced by a factor 10^5. To decouple the wide aperture requirements for the incoming positron beam from the final emittance requirements of the main linac, a collector ring with a large dynamic acceptance and relatively large equilibrium emittances is used to pre-damp the incoming beam. Then after six damping times the beam is injected into a final damping ring with very small

equilibrium emittances adapted to the main linac injection. In the case of electron production, taking into account the incoming normalized emittances of 7000 nm·rad provided by the high brilliance injector linac, a single ring similar to the final positron damping ring will be sufficient.

At each repetition period a train of damped bunches is extracted from these damping rings, and at the same time a new train coming from the injector linac or from the positron source is injected. For a damping ring of circumference C accommodating a bunch train of length l_s (including space for the injection and ejection fast kicker rise and fall times), transferring the beam at a repetition frequency f_r, we define the *reduced damping time* $\tau_r = \tau_{x,y}/C$ which has to satisfy in both planes $\tau_r < 1/(n_\tau\, l_s f_r)$, n_τ being the number of damping times necessary to damp the incoming emittance to the acceptable level ε_{target}.

2.2.4.2 Choice of the beam energy

The optimum beam energy must not be determined from optical considerations, but rather be based on Intra-Beam Scattering (IBS) and polarization. The polarized lepton option requires an energy of $(n{+}0.5) \times 0.44$ GeV to avoid depolarizing resonances. The γ^3 dependence of the normalized equilibrium emittance of a lattice prevents energies larger than 2 GeV. In order to avoid strong IBS, an energy of 1.98 GeV has been chosen.

2.2.4.3 Wiggler effects and energy spread

The total radiation loss in the presence of wigglers with a given field, for a fixed value of τ_r, is independent of the ring structure and of the value specified for the target emittance ε_{target} [2.5]. In Fig. 2.3 the required wiggler length for a well-defined reduced damping time is shown for different combinations of arc and wiggler field. The quantity R_{ra} will be used in the following to denote the ratio of the total losses around the ring to the losses in the arcs.

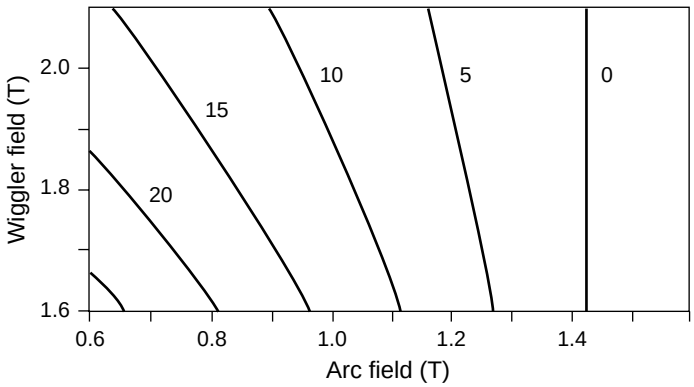

Fig. 2.3: *Wiggler field vs. arc bend field for a given reduced damping time of 44 μs/m and different wiggler lengths (m) at 1.98 GeV.*

Even though they are installed in a dispersion-free straight section, the wigglers will create local dispersion and thereby generate additional emittance. The aim of a very low ring equilibrium emittance, and thus a small wiggler contribution to the emittance, requires a short wiggler period. Furthermore, increasing the wiggler length or field will not reduce indefinitely the ring equilibrium emittance as it will become dominated by the wiggler contribution to the emittance (Fig. 2.4).

2.2.4.4 Arc cells

As proposed in Ref. [2.6] the arcs are made of detuned Theoretical Minimum Emittance (TME) cells. The dispersion and β_x functions in the bending magnets are chosen larger than those required for the minimum emittance, in order to increase the dispersion both in the bending magnets (and consequently the momentum compaction α) and at the potential sextupole locations.

A given detuning ratio ε_r of the actual equilibrium emittance to the minimum possible emittance may be achieved by different combinations of D_x and β_x at the centre of the bending magnets. It is important to select the combination yielding the largest possible D_x value for a given ε_r, as a large momentum compaction α is required to maximize the impedance threshold. In this case the lattice parameters in the centre of the bending magnet are entirely determined [2.6], and given by

$$\beta_x = \varepsilon_r \frac{l_{bend}}{2\sqrt{15}} \qquad D_x = (1 + \frac{2}{\sqrt{5}}\sqrt{\varepsilon_r - 1})\frac{\theta\ l_{bend}}{24} \quad ,$$

where θ and l_{bend} are the deflection angle and the length of the bending magnet.

Using the above expressions the momentum compaction factor of a ring containing exclusively regular TME cells depends only on the cell length l_{cell}, the bending magnet parameters and the detuning ratio ε_r.

$$\alpha = \frac{1}{12}\frac{l_{bend}}{l_{cell}}\theta^2\,(1+\sqrt{\frac{\varepsilon_r^{\,2}-1}{5}}) \quad .$$

The horizontal cell phase advance depends only on the emittance detuning ratio. A value of $\varepsilon_r = 3.9$ is proposed for the three rings of the 3.0 TeV option (Table 2.5). This yields sufficiently large D_x values.

2.2.4.5 Momentum compaction and impedance turbulence threshold

The ring used in the analytical calculations has a race-track shape. It consists of two 180° arcs, made of bending magnets of length l_{bend} in regular arc cells of length $l_{cell} \sim 2\,l_{bend}$ and a constant space required for the focusing part of the cell. Two long straight sections house the injection/ejection system and the RF cavity, with a total length assumed to be the sum of a fixed part of ~18 m and a variable part of 1.8 times the wiggler length. The wigglers are distributed among the two straight sections in order to minimize the ring dimensions. Using this geometry the expression for the momentum compaction shown above may be corrected for the presence of the two long straight sections.

The number of regular arc cells required to produce the target emittance and the reduced damping time, taking into account the wiggler effects, can now be evaluated. It is a function of the wiggler characteristics (field, period), of the emittance detuning ratio chosen and, obviously, of the target emittance and the beam momentum.

As σ_e has a weak dependence on the ratio R_{ra}, the turbulence impedance threshold, calculated with the usual formula $(Z/n)_{thr} = \alpha\,(2\pi)^{3/2}\,E\,\sigma_e^{\,2}\,\sigma_s/(N_b\,e^2\,c)$, will show approximately the same behaviour as α. Large R_{ra} ratios yield large $(Z/n)_{thr}$ and α values, and small arc bend fields (Fig. 2.5). This allows an increase of l_{bend} and larger values for D_x and β_x, easing the chromaticity correction.

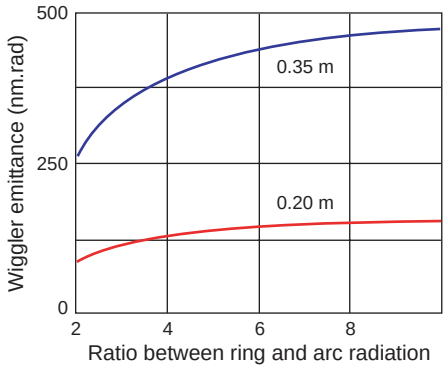

Fig. 2.4: *Wiggler contribution to the normalized emittance, vs. R_{ra}, for B_{wig} = 1.73 T, $<\beta_x>$ = 2.5 m at 1.98 GeV and τ_r = 35 μs/m for wiggler wavelengths 0.35 m and 0.20 m.*

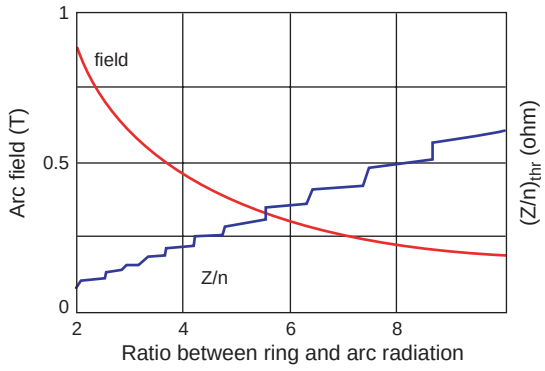

Fig. 2.5: *$(Z/n)_{thr}$ and arc field vs. R_{ra}, for B_{wig} = 1.73 T, $<\beta_x>$ = 2.5 m at 1.98 GeV and τ_r = 35 μs/m, a normalized emittance of 1.9×10^{-6} m assuming σ_s = 3 mm and 4.2×10^9 particles per bunch.*

2.2.4.6 Ring parameters

The proposed Electron (EDR) and Positron (PDR) Damping Rings are assumed to have the same ring, cell and wiggler geometry. The ring has a racetrack shape with two long straight sections, the lengths of which are included in the circumference equal to 485 m. These sections contain in common the RF cavities, the wiggler magnets, and the injection and extraction insertions. The chosen emittance detuning ratio ε_r of 3.9 yields reasonable values for the momentum compaction and the strength of the chromaticity correction. Further optimization of the damping ring parameters requires detailed modelling of the effects of the wigglers, intra-beam scattering, errors and misalignments.

The Positron Collector Ring (PCR) is assumed to operate at the same beam energy as the damping rings. Although the damping time parameters are similar to those of the damping rings, the large target emittance requires a much smaller number of arc cells. With a circumference of only 155 m, the collector ring could be installed inside the damping rings (Table 2.5).

Table 2.5: Tentative collector and damping ring parameters

Parameter	Unit	EDR	PDR	PCR
Ring momentum	GeV/c	1.98	1.98	1.98
$\gamma\,\varepsilon_{target}$	10^{-6} m·rad	0.43	0.43	60
τ_r	μs/m	43.7	53.0	43.7
n_τ		6	5	6
ε_r		3.9	3.9	3.9
N_{cell}		72	72	18
B_{arc}	T	0.3	0.3	1.0
$B_{wiggler}$	T	1.81	1.60	1.80
L_{bend}	m	1.92	1.92	2.30
L_{cell}	m	5.84	5.84	6.61
Circumference	m	485	485	155
α	10^{-3}	0.49	0.49	7.3
σ_e	10^{-3}	0.75	0.69	0.71
$(Z/n)_{thr}$	Ω	0.13	0.11	1.72

2.2.5 Bunch compressors and transfer lines

The damping ring is designed to deliver a beam at the energy of 1.98 GeV, bunched at the RF frequency of 3 GHz, of relative r.m.s. energy spread $\leq 0.082\%$ and of r.m.s. bunch length of 3 mm. The required bunch length in the main linac should be 30 μm in order to reduce the dilution effect of transverse wakefields on the vertical emittance. The corresponding compression rate is 100 which cannot be obtained by a single compression stage because at the energy of 1.98 GeV the r.m.s. energy spread will rise to 8.2%, too large to transport the beam through the injector complex, and at the energy of 9 GeV the R_{56} becomes –0.166 m implying either a short and strongly radiating chicane or a long one with too high values of the maximum β optical function.

Thus two stages of compression are proposed: one at 1.98 GeV and one at 9 GeV, the latter in order to benefit from a higher gradient and a larger RF frequency [2.7]. A compromise has to be found between an acceptable r.m.s. energy spread at the exit of the first stage and the R_{56} required by the second stage. The compression factor of 12 of the bunch compression first stage has been chosen because the r.m.s. energy spread at the exit is an acceptable value of about 1% and the resulting R_{56} of the second stage is relatively small (–0.014 m). The first pseudorotation in the longitudinal phase-space is obtained through RF systems working at a phase equal to $k\pi$, which linearly correlate the momentum with the position of the particles in the bunch. This rotation requires integrated RF voltages of 103 MV at 3 GHz and of 1026 MV at 30 GHz for each compressor stage, respectively. The second pseudorotation in the longitudinal phase space is achieved by a magnetic chicane consisting of two parts, one being the mirror image of the other. Each part is composed of two rectangular dipoles, of length L_m and bending angle θ, separated by a drift space of length L. The chicanes have been optimized to reduce the maximum values of the β Twiss function. Their optical functions are shown in Fig. 2.6 and Fig. 2.7.

The parameters of the two bunch compressors [2.8] obtained to first order have been inserted into a longitudinal tracking program to investigate how the beam will behave when the higher-order magnetic effects (of the chicane) and the strong wakefields are taken in account. Figure 2.8 and Fig. 2.9 show the longitudinal phase space before the compressor (horizontal scatter plot), after the RF pseudo-rotation (oblique scatter plot) and at the exit of the chicane (vertical scatter plot) for the first and second stage, respectively. The high-order effects are small, only slightly lengthening the bunch by one micron.

The effect of the coherent radiation has not been investigated but a rough estimate suggests that it should be negligible. Numerical tracking has to be carried out to confirm this. The present design might be slightly modified to reduce its consequences.

Since the injection complex is foreseen to be in a central position (Fig. 2.2) each beam (e^- and e^+) has to be transported at 9 GeV to the entrance of the second bunch compressor, before injection in the main linac. These two transfer lines consist of regular FODO cells, with sufficiently low vacuum (~ 10^{-10} Torr) in order to prevent ion-trapping instability. Removal of the beam halo generated in the injector complex is foreseen in these transfer lines, either by conventional spoilers and collimators or by resonant drift in nonlinear fields; both techniques remaining to be studied and compared.

The 360° turn-round consists of 48 isochronous modules [2.9], each one made of three identical dipoles (1 m long) and of four quadrupoles. Symmetric triplets match the modules between them. The overall diameter of the turn-round is 430 m approximately, in order to limit to 60 nm·rad the horizontal emittance growth due to the synchrotron radiation. All the other major bends can be built on the same basis.

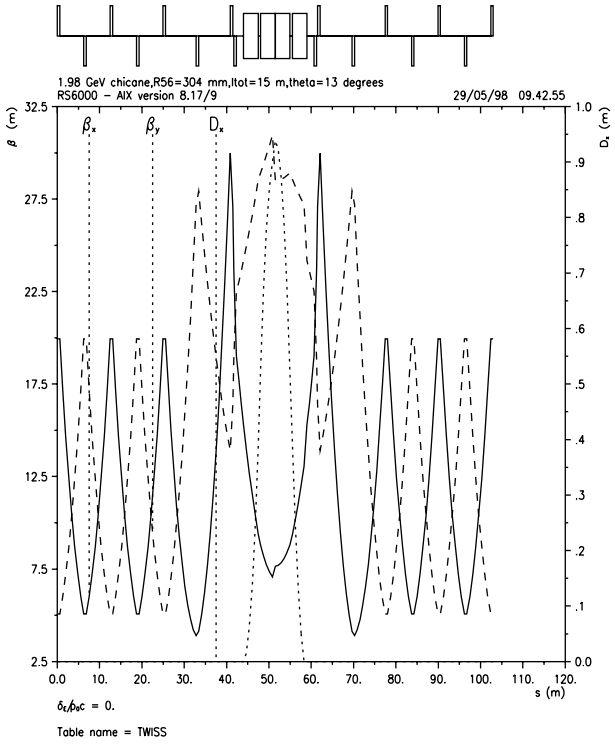

Fig. 2.6: Optical functions in the first chicane.

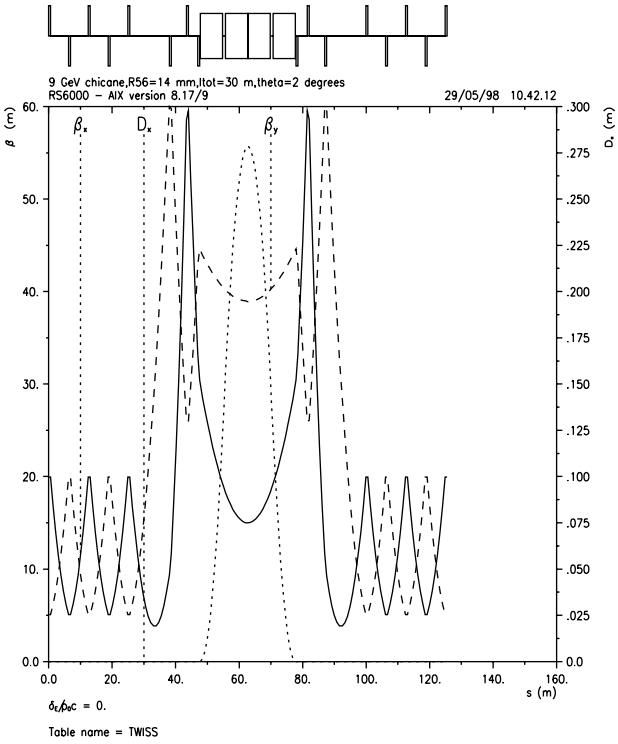

Fig. 2.7: Optical functions in the second chicane.

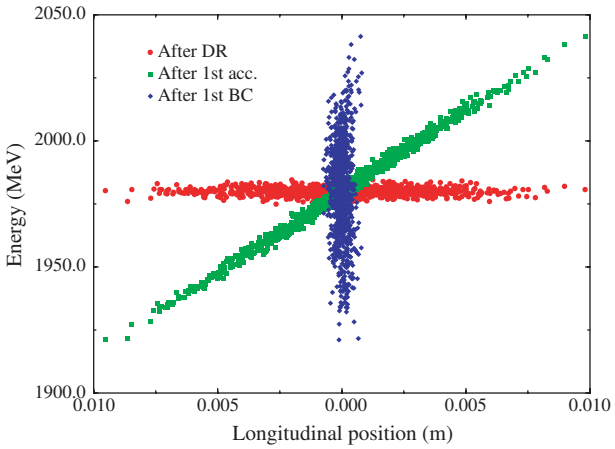

Fig. 2.8: Longitudinal phase space in the first stage.

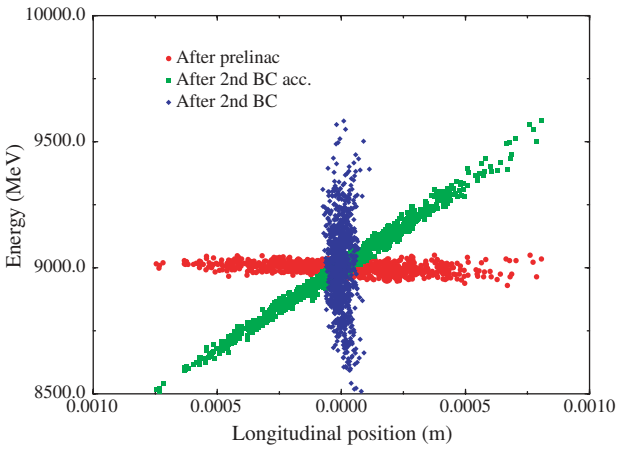

Fig. 2.9: Longitudinal phase space in the second stage.

2.3 Main linac

2.3.1 The main linac lattice

The main linac accelerates the beam from 9 GeV to 1.5 TeV. In order to facilitate the matching of the layout of the drive beams and the main beam the two are built of 2.23 m long modules. Each main linac module contains four 0.5 m long accelerating structures. Between one and four of these structures may be replaced by a quadrupole to provide the necessary focusing. A beam-position monitor (BPM) is placed at the head of each girder. The beam line consists of twelve sectors, each containing FODO cells of equal length and phase advance [2.10]. The main

characteristics of the linac lattice, made of these 12 sectors with constant cells and of matching insertions between the sectors, are given in Table 2.6. In order to keep the fill factor about constant, the target values of the focal length f and the quadrupole spacing L are scaled from the initial values $f_0 = 1.5$ m and $L_0 = 2.5$ m with the energy E as $L(E) = L_0(E/E_0)^{1/2}$, $f(E) = f_0(E/E_0)^{1/2}$. The actual values in each sector are adjusted to the hardware geometry, see Fig. 2.10. The phase advance is about 70° per cell but varies slightly from sector to sector. This small value allows a better compromise to be found between time-dependent and static effects. The matching of one sector to the next is achieved by adjusting the strengths of the last three quadrupoles of the previous sector and the first two of the following one. The fill factor is 78%.

Table 2.6: Lattice-geometry parameters in each sector of the linac

Sector no.	No. of quads/ sector	Quad. length (m)	Cell length (m)	Sector length (m)
1	160	0.5	4.46	364.8
2	82	0.5	8.92	373.9
3	82	1.0	8.92	373.9
4	160	1.0	13.38	1094.4
5	152	1.0	17.84	1386.2
6	88	1.0	22.30	1003.2
7	62	1.5	22.30	706.8
8	152	1.5	26.76	2079.4
9	148	1.5	31.22	2362.1
10	94	1.5	35.68	1714.6
11	56	2.0	35.68	1021.4
12	88	2.0	40.14	1805.8

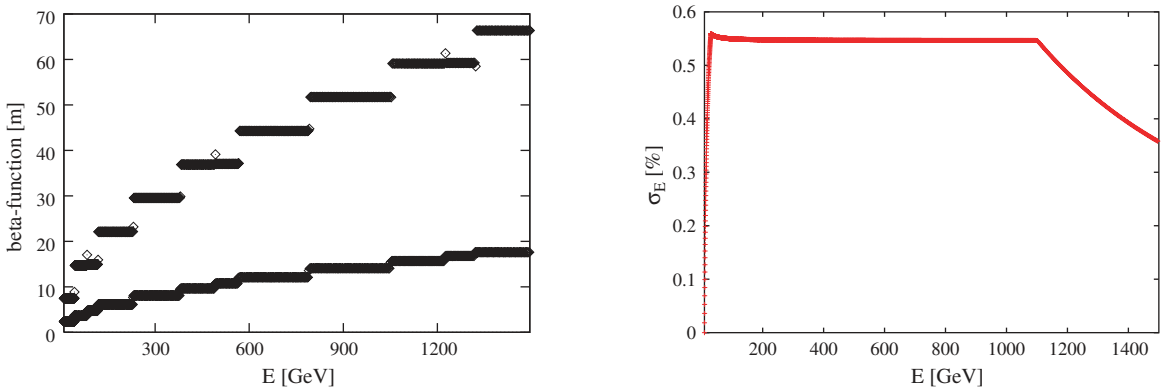

Fig. 2.10: *The beta-function and the beam energy spread along the main linac.*

The beam consists of a train of 154 bunches with a charge of 4×10^9 particles each that are separated by 20 cm. The bunch length is $\sigma_z = 30$ µm, the transverse emittances used for simulations are $\varepsilon_x = 680$ nm·rad and $\varepsilon_y = 5$ nm·rad and the increase of the vertical emittance should admittedly be less than 5 nm·rad.

In order to stabilize the beam, the so-called BNS damping is used. Between $E = 9$ GeV and $E = 30$ GeV the RF phase is set so as to create a relative energy spread in the bunch, which is maintained using another phase in the main part of the linac. In the last part, the RF phase is set so as to decrease the energy spread to a full width of 1% so that the beam can pass the final focus system. The optimum phases will have to be determined in practice. In the presence of ground motion, a larger energy spread leads to better results if a few feedbacks are used to re-steer the beam, while a smaller energy spread is advantageous if a one-to-one correction is used for the same purpose (see Fig. 2.16). For the present simulations $\Phi = 6°$ is used in the main part of the linac, leading to the energy spread shown in Fig. 2.10.

The control of the bunch-to-bunch energy spread requires the compensation of the beam loading in the main linac. It is proposed to achieve this compensation by generating a ramp in the RF power output of the Power Extraction and Transfer Structures (PETS) as explained in Section 3.1. Simulations show that a full bunch-to-bunch energy spread of less than 5×10^{-4} can be obtained in the main beam with the RF voltage resulting from a delayed phase-switching technique [2.11] (Fig. 2.11).

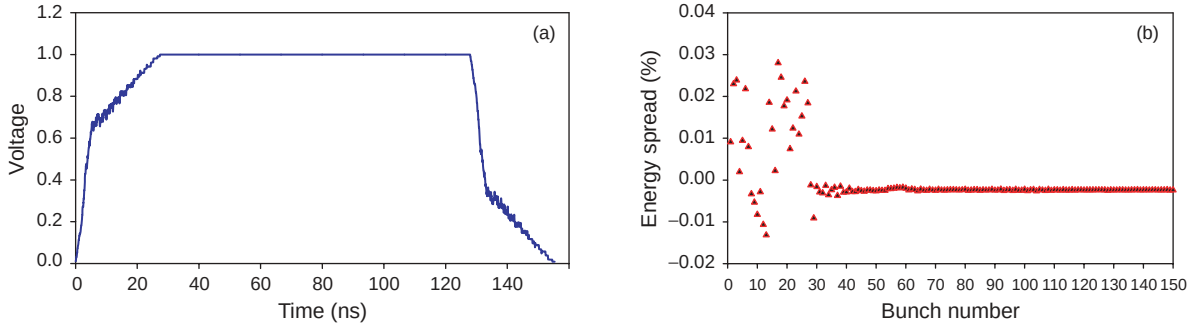

Fig. 2.11: *(a) RF voltage output from PETS when the delayed phase-switching technique is applied to the drive-beam pulse; (b) Energy spread along the main-beam pulse accelerated with the RF pulse shown in (a).*

The gradient in the structures is slightly less than 150 MV/m since some overhead is provided for feedback purposes. The single-bunch wakefields have been calculated in Ref. [2.12]. The longitudinal multibunch wakefields are assumed to be fully compensated. For the transverse multibunch wakefields a simple model is used, which takes into account only the wakefield amplitude.

2.3.2 Static trajectory correction

2.3.2.1 Beam-based alignment

Before correction, the beam-line elements will be pre-aligned by means of a sophisticated system of wires. As a result of this, the positions of all the linac components will be randomly scattered around the so-called averaged pre-alignment line. The system of wires foreseen allows misalignment r.m.s. amplitudes of the order of 10 μm. While this accuracy is relevant for the beam-position monitors (BPMs) and for the accelerating structures pre-aligned on every girder with respect to the BPMs (see Fig. 2.1), it is not really critical for the quadrupoles which are re-aligned with the beam as explained below; for instance, an initial 50 μm r.m.s. scattering is acceptable for quadrupoles. The relative misalignments of the girders are defined by those assumed for the BPMs.

This precision of 10 μm is, however, not sufficient to keep the growth of the vertical emittance smaller than 100% in the main linac. Therefore, beam-based alignment of the quadrupoles is necessary. The main proposed scheme is the ballistic alignment method [2.13]. In this method the beam line is divided into a number of bins containing 12 quadrupoles each that are corrected one after the other. In the first step of the correction all the quadrupoles in the bin are switched off, except the first one. The beam is then steered into the last BPM of the bin. The other BPMs are moved onto the trajectory of the beam. It has been verified that the beam divergence does not generate a transverse beam-size larger than ~ 75 μm r.m.s. over the length of a bin. In the second step, the quadrupoles are switched on again and a simple few-to-few correction is performed. This method allows all the BPMs in a bin to be aligned on a relatively straight line (see Fig. 2.12) and thus to reduce the dispersion to a very small value. The remaining emittance growth is almost entirely due to the wakefields of the structures that are scattered around the beam trajectory. It therefore depends very little on the RF phases chosen.

In the simulations, all elements are assumed to be scattered around a common axis following a normal distribution with a sigma of 10 μm for BPMs and structures and 50 μm for quadrupoles for the reasons explained above. The BPM resolution is 100 nm [2.14]. Beam jitter during correction, remanent fields of the quadrupoles when switched off and the shift of the quadrupole centre with field strength (from remanent to nominal field) are also possible error sources. In the simulation, a position jitter of the incoming beam of 0.1 σ is included. If the jitter is larger, one can average over a number of pulses. The size of the remanent field is sampled from a constant distribution between 0% and 2% of the nominal value. The shift of the centre is assumed to follow a Gaussian distribution with a sigma of 10 μm. The effect of these imperfections can be very large at the first correction step, but iterating the correction in a bin solves the problem almost completely [2.15]. The emittance growth simulated with PLACET [2.16] is about $\Delta\varepsilon_y/\varepsilon_y \approx 270\%$ (Fig. 2.12), which is still larger than the goal set. This method of correction is robust and will be the basic static correction applied when starting the linac.

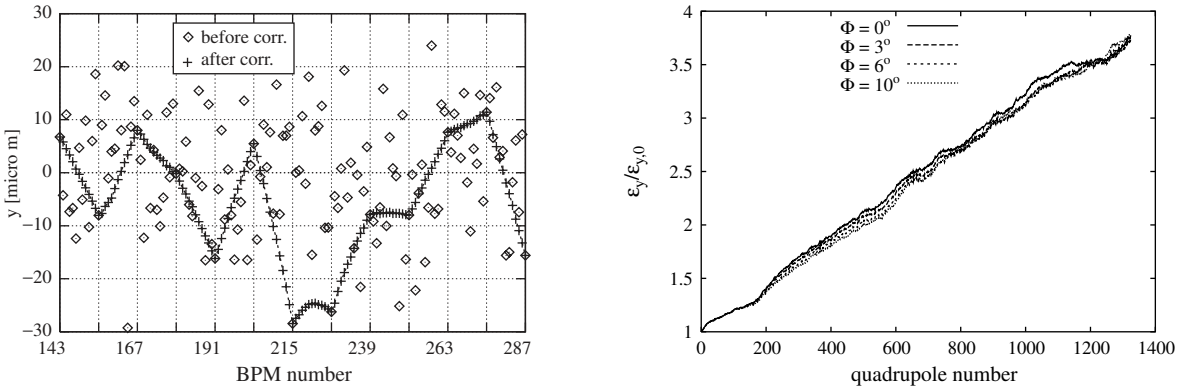

Fig. 2.12: *Left-hand side: The BPM positions before and after the ballistic correction. Right-hand side: The emittance growth after ballistic correction for different RF phases.*

2.3.2.2 Multi-step lining-up

The Multi-step Lining-up (ML) method [2.17] has in common with the ballistic method the idea to align the main components of the linac on a straight line defined by the beam. The ML method is also based on the observation that to align the quadrupoles on a reference line is more important than the actual choice of this line, provided the latter is not too far away from the average-alignment line determined by the positions of the components resulting from the pre-alignment. Instead of switching off the quadrupoles, the ML method relies on a small change of their strengths (several per cent) in a bin (linac section) and on measurements of trajectory differences, like in the dispersion-free correction [2.18]. This minimizes the heat-load variations and makes the remanent field and hysteresis effects negligible, though the magnetic centre of the quadrupoles might shift with the excitation level. The results are dependent only on the BPM resolution (as in the ballistic method), the beam is kept focused and close to the centre of the elements (reduced wakefield effects) and on-line corrections are feasible after matching the detuned section to the rest of the linac.

The sequence of the ML correction operations applied on the pre-aligned but scattered components of the linac is the following. At first, a single bunch is injected and successive trajectory corrections or beam-based re-alignments are applied in sections of the linac, according to the following procedure:

- Select successively bins of N quadrupoles where N is optimized for an accurate estimation of the reference line and of the bin-injection slope s_{inj} and off-set x_{inj}. The number N of quadrupoles is of the order of 12 to 15.
- Inject the beam on the nominal lattice (focal distance f_1) and measure the beam positions at the BPMs, averaged over 100 pulses (~1 s) in order to gain a factor 10 on the resolution and acquisition errors.
- Inject a beam with a detuned lattice in the bin considered (change the focal distance by ~5% to a new value f_2) and with betatron matching to the rest of the linac. Measure beam positions again.
- Run the ML algorithm [2.19] on the measured trajectory differences, getting rid of the absolute off-sets of the BPMs, and apply the following steps: i) Using the high resolution of the BPM (100 nm), calculate the quadrupole displacements $d_{\mathrm{q,k}} = \delta_{\mathrm{q,k}} - x_{\mathrm{inj}} - kLs_{\mathrm{inj}}$ (k is the quad-index and L the distance between quadrupoles) with respect to the injection line, still unknown; ii) Estimate the injection line parameters by a least-squares fit on the BPM readings corrected for the quadrupole misalignments. This provides the change of slope (kick) that steers the beam toward the reference line (close to the average pre-alignment line); iii) Move the first quadrupole of the bin (with a resolution better than 1 μm) in order to apply the computed kick. Displace all the quadrupoles by the estimated $d_{\mathrm{q,k}}$ in order to move them towards the reference line defined by the algorithm.
- Set back the nominal lattice f_1, suppress the bin-matching and inject a beam to measure the actual positions read by the BPMs. Move all the BPMs sitting at the head of each girder to the reference line, by zeroing their reading (within their resolution). This is a kind of 'calibration' of the measurement system. Moving the BPMs means moving the girders (Fig. 2.1), and the cavity position scattering is reduced to their initial pre-alignment imperfections on a single girder, decreasing accordingly the wakefield effects.
- At least one iteration of this process is needed because the lattice model used in the algorithm cannot include the wakefields.

This whole procedure is repeated bin after bin over the whole linac, before the full-intensity beam can be injected. Simulations of the emittance growth have been carried out with MUSTAFA [2.20]. Figure 2.13(a) shows the r.m.s. and maximum beam off-sets with respect to quadrupole centres and Fig. 2.13(b) the simulated blow-up, after ML correction and before emittance bumps (of the same order of that obtained after ballistic correction).

The multi-step lining-up is considered as a complement to the ballistic method. More studies will deal with the possibility to use ML for time-to-time corrections (keeping the quadrupoles ON and the beam transmission) when small deviations are observed in the BPMs because of component drifts after a static correction, and as a feedback if much smaller variations of the quadrupole strengths are considered (~0.5%). To maintain the measurement resolution needed, the quadrupoles might be forced to oscillate at a given frequency and the corresponding beam positions detected by notch filtering around the same frequency.

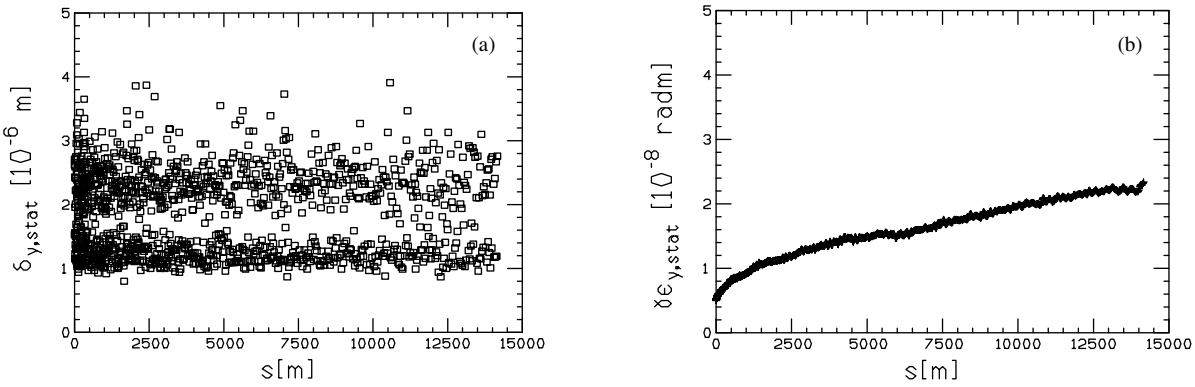

Fig. 2.13: *(a) r.m.s. and maximum beam off-sets with respect to the quadrupole centres; (b) Emittance blow-up along the linac, after ML correction.*

2.3.2.3 Emittance-tuning bumps

A further reduction of the emittance growth after ballistic or ML correction is necessary. A possible way to achieve this additional reduction consists of applying emittance-tuning bumps. In the simulation case, these bumps are created by two pairs of accelerating structures around two quadrupoles followed by a feedback system. This system consists of these quadrupoles that are about $\pi/2$ apart and serve to steer the beam onto the initial trajectory, and of an emittance measurement station. An illustration of the effect of one of these bumps is given in Fig. 2.14 (left), where the two quadrupoles no. 124 and no. 126 and the nearby cavities are numerically displaced in order to reduce the emittance growth downstream from 160% to 100%, in this particular case. In practice, two groups of accelerating cavities will be displaced. The structures are moved in order to minimize the emittance at the measurement station. With 10 bumps distributed along the linac, the emittance growth can be reduced to about 15% for $\Phi = 6°$, see Fig. 2.14 (right). Here, the results strongly depend on the RF phases because the emittance growth due to the dispersion is almost completely cancelled by the ballistic correction while the bumps prevent the emittance growth due to wakefields. The remaining blow-up corresponds to the cross talk of the dispersion and wakefield effects. Using five bumps results in about 30% emittance growth. The multibunch results are very close to those for single bunches, see Fig. 2.15 (left).

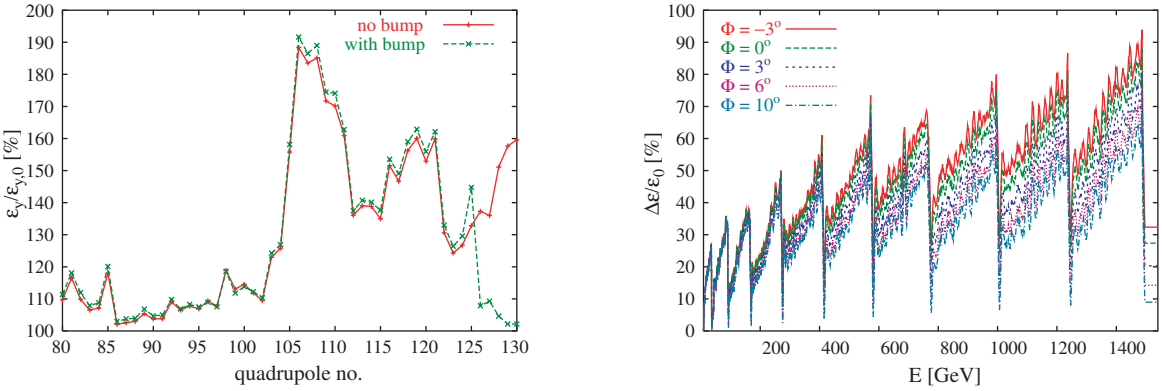

Fig. 2.14: *Left-hand side: Illustration of emittance-bump effect on a single bunch. Right-hand side: The emittance growth for different RF phases in the main linac.*

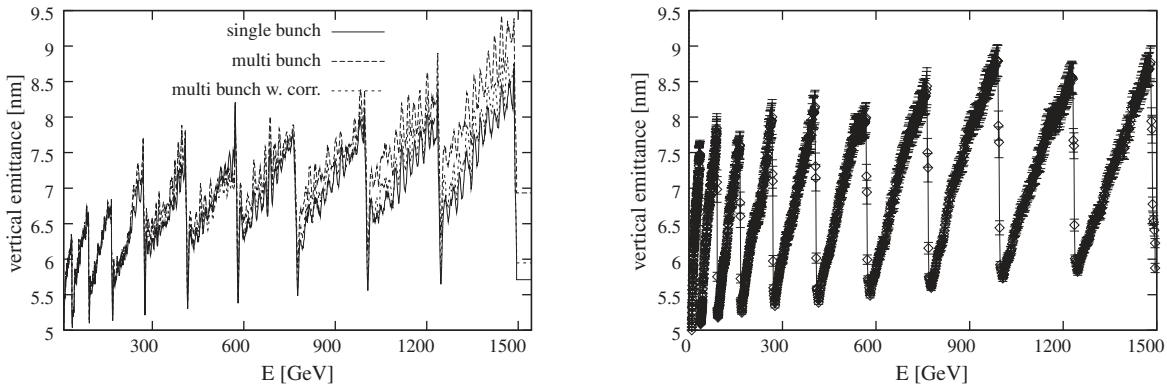

Fig. 2.15: *The emittance growth found after applying the ballistic correction and optimizing the emittance tuning bumps. On the left-hand side the single- and multibunch cases are shown. On the right-hand side the accelerating structures have been aligned to the beam after the ballistic alignment leading to a very smooth emittance growth.*

The emittance grows significantly after each tuning bump and this is due to the initial misalignment of the BPMs. This large beating can be prevented by realigning the accelerating structures onto the new beam trajectory. Figure 2.15 shows the emittance blow-up for this case, where the variations have been almost completely suppressed. The final position error of the structures is assumed to follow a normal distribution with a sigma of 10 μm.

2.3.3 Time-dependent effects

Three main dynamic effects that lead to emittance growth have been considered [2.10]. First, the quadrupoles may jitter independently, for example because the cooling water induces vibrations. Second, the ground will move coherently. Third, the beam itself may jitter. No data are available for the first and the last effects, therefore only tolerances can be given. The size of the second effect depends on the site and we have not yet achieved general consensus on the model to retain. Here, the so-called ATL model is used with $A = 5 \times 10^{-7}$ μm^2 m^{-1} s^{-1}.

An r.m.s. jitter of the quadrupoles of 1.3 nm leads to a single-bunch emittance growth with respect to the original beam axis of 6%. This cannot be reduced except with an intra-pulse feedback comparable to the one described in Ref. [2.21] or with a change of the lattice or beam parameters. The increase of single-bunch emittance expected from a beam-offset of $\Delta_y = 0.3\ \sigma_y$ is also 6%.

With the assumed ground motion model, one finds that the emittance increases in one minute by 50% if only one feedback after the linac is used to steer the beam to its original trajectory (such a trajectory feedback is made of one pair of fast kickers in each plane and BPM devices downstream). However, the ground motion effects can be reduced by the use of various feedbacks in the linac. Four different stages are envisaged. In the first, trajectory-feedbacks of the kind described above steer the beam locally back to its original trajectory, in the linac itself. If 10 such feedbacks are used which are placed at equal distances along the linac, the remaining emittance growth is 11% per minute (Fig. 2.16 left). If one used a larger energy spread in the linac, this growth could be reduced while the static growth would increase at the same time. In the second stage, a one-to-one correction is performed on a longer time-scale, over the whole linac length. This has most likely to be done in steps — moving the quadrupoles that give the largest effects first. A detailed investigation about the performance of this correction, including a smooth transition from the first step remains to be done, and the possibility to use as an alternative the multi-step lining-up, with small oscillations of the quadrupole strengths, forced at a given frequency (Section 2.3.2.2), has to be studied. If the one-to-one correction is performed in a single step, one finds a single-bunch emittance growth of about 20% per day (25% in the multi-bunch case), as illustrated in Fig. 2.16 (right). Here, a smaller energy spread in the main linac would give better results. The optimum has thus to be found by evaluating the transition from simple feedbacks to one-to-one correction. The third stage would be a re-tuning of the emittance bumps which leads to 5% growth per day. The fourth stage would perhaps be a complete realignment of the beam line.

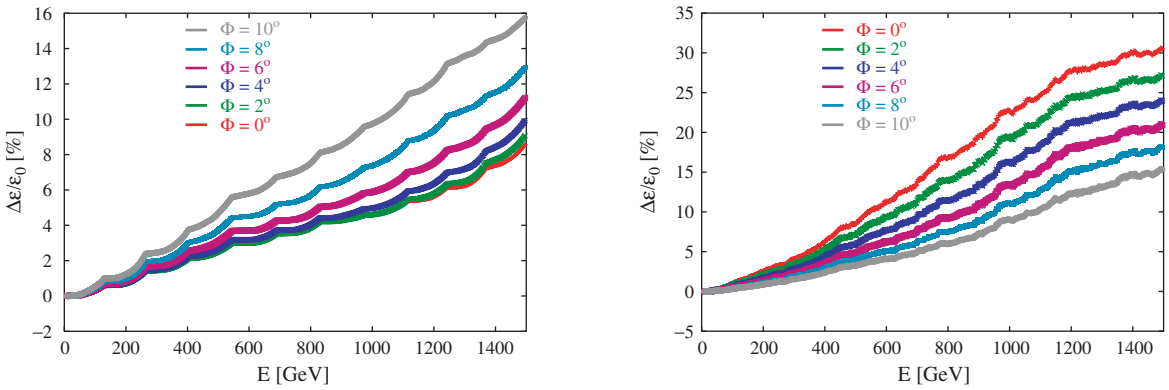

Fig. 2.16: *The emittance growth due to ground motion assuming the ATL model: on the left-hand side after one minute and using 10 feedbacks; on the right-hand side after one day using a one-to-one correction. With the feedbacks the larger energy spread ($\Phi = 0°$) is more stable, while for the one-to-one correction the smaller energy spread ($\Phi = 10°$) is advantageous.*

2.3.4 Emittance balance

This section summarizes the contributions to the emittance growth expected from the various sources of perturbations and corrections discussed in the preceding sections, for the lattice of Section 2.3.1. The beam energy varies in the linac from 9 GeV at injection to 1.5 TeV at the end. During the acceleration, the normalized transverse emittances grow for the reasons described above and this growth is controlled by the various corrections reviewed in the preceding sections. The most critical phase-plane is obviously vertical where the emittance is very small in order to allow the nominal luminosity retained. It is therefore interesting to summarize the expected values of the absolute increase of the vertical emittance [2.22]. At first, Table 2.7 gives the single-bunch growth after each static correction, according to Section 2.3.2 and assuming 10 μm r.m.s. misalignments. It shows that the one-to-one correction alone is by far insufficient, the ballistic correction and the multi-step lining-up are essentially equivalent, and that combining the ballistic correction with 10 emittance bumps allows a single-bunch vertical increase of the targeted amplitude (~1 nm·rad) to be achieved. Injecting a multibunch train after the latter combined correction gives a total effective emittance growth of ~2 nm·rad which can be reduced to ~1 nm·rad after re-optimization of the emittance bumps and one-to-one correction with the whole train (Table 2.8). Turning now to the time-dependent effects (Section 2.3.3), Table 2.9 gives the vertical emittance rise expected from simulations of uncorrelated quadrupole jitter and vertical injection beam-jitter (relative to the vertical beam size σ_y). The corresponding values indicate that a requirement to keep the contributions of these two jitters of the same order as in the static case implies tight tolerances. The last figure in Table 2.9 is the ground motion effect expected after one day, assuming that the ATL law applies. The total effective increase of the vertical emittance is obtained by adding the optimum static multibunch growth (~1 nm·rad, cf. Table 2.8), the jitter contributions and the ground motion effect per day (Table 2.9). On the basis of the simulations done, this effective increase would reach an amplitude of 5 nm·rad after 3 days and 8 nm·rad after 6 days; this implies repeating some corrections after such a period of time or using feedbacks which remain to be studied. Table 2.1 relies on these numbers for the estimates of emittance growths in the linac.

Table 2.7: Single-bunch vertical emittance increase after various static corrections

Effects of misalignments + static corrections	$\Delta(\gamma\varepsilon_y)$ **[nm·rad]**
After one-to-one correction only	135
After ballistic correction only	15
After multi-step lining-up	17
After ballistic correction and 10 emittance-bumps	0.75

Table 2.8: Multibunch vertical emittance after static correction and possible re-optimization

Effects of misalignments + static corrections	$\Delta(\gamma\varepsilon_y)$ **[nm·rad]**
Multibunch, injected after the best single-bunch correction	2
Multibunch, after re-optimization of the emittance-bumps and re-application of one-to-one correction to the train	1

Table 2.9: Vertical emittance dilution due to uncontrollable time-dependent effects, which adds to the multibunch emittance increase remaining after static corrections (Table 2.8)

Effects of dynamic, time-dependent position-fluctuations	$\Delta(\gamma\varepsilon_y)$ **[nm·rad]**
Uncorrelated quadrupole jitter of 2 nm	0.5
Vertical beam jitter at injection of amplitude 0.5 σ_y	0.5
Ground motion contribution (ATL law) after 10^5 s	~1 per day

2.3.5 The main linac accelerating structure

The CLIC main linac accelerating structure, the Tapered Damped Structure (TDS), has 150 cells, is 500 mm long, and operates in the $2\pi/3$ travelling-wave mode. The design of the structure is driven by extreme performance requirements: accelerating gradients well in excess of 150 MV/m, power flows in excess of 200 MW, a 10 μm structure straightness and alignment tolerance (to preserve single-bunch emittance), long-range transverse wakefield suppression of over two orders of magnitude (to preserve train emittance) and ultimately a low mass-production cost.

The issues of gradient, power and tolerances are each in part addressed by ultrahigh precision diamond turning of the copper disks that make up the sections. This technique gives a 1–2 μm dimensional tolerance and an optical-quality surface finish. The 10 μm tolerance of assembled sections is guaranteed by a specially developed hybrid brazing/diffusion bonding technique. Measured Q factors correspond to 98% of the theoretical value in (undamped) constant impedance structures. Constant impedance structures were tested in CTF1 to 125 MV/m (albeit with pulses that reached these peak levels for only a few nanoseconds) [2.23].

Long-range transverse wakefields are suppressed through a combination of strong damping and detuning [2.23]. The damping is accomplished by coupling to each cell of the structure four individually terminated waveguides. The damping waveguides have a rectangular cross-section of 4.5 mm by 1.9 mm, hence a cutoff frequency of 33.3 GHz, which is above the fundamental but below all higher-order modes. In this way higher-order mode energy propagates out of the cells via the damping waveguides but the fundamental mode energy does not. This results in a Q of approximately 16 for the lowest, and most dangerous, dipole passband. A taper in the iris diameter from 4.5 mm at the head of the structure to 3.5 mm at the tail provides a detuning frequency spread of 2 GHz (5.4%). The layout of the cell structure can be seen in Figs. 2.17 and 2.18.

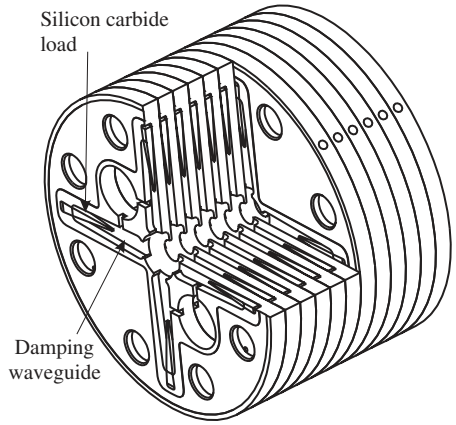

Fig. 2.17: *Cross-sectional view of the TDS geometry.*

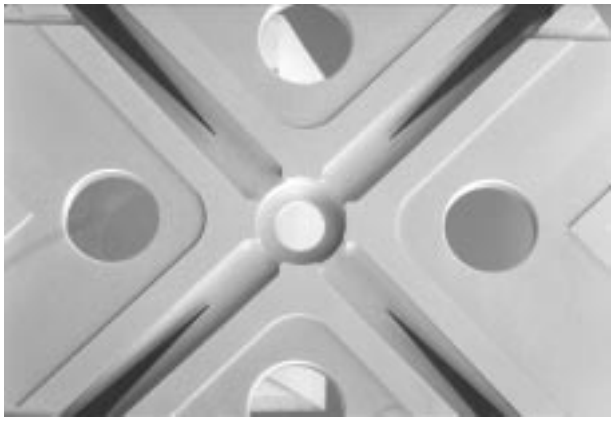

Fig. 2.18: *Photograph of a TDS cell with damping waveguides and SiC loads.*

Cell dimensions and some of the fundamental mode characteristics of the beginning, middle and end cells are given in Table 2.10.

Table 2.10: Fundamental mode parameters of the TDS as calculated using HFSS

Cell radius [mm]	**Iris radius [mm]**	Q	R'/Q **[kW/m]**	v_g/c
4.255	2.250	3628	20.2	10.4
4.111	2.000	3615	23.0	7.5
3.984	1.750	3621	27.1	5.2

By using these calculated fundamental mode characteristics, the power flow (Fig. 2.19), accelerating gradient etc. along the structure are calculated. The accelerating gradient profile is plotted in Fig. 2.20. The nominal average gradient of 150 MV/m is obtained with 250 MW input power.

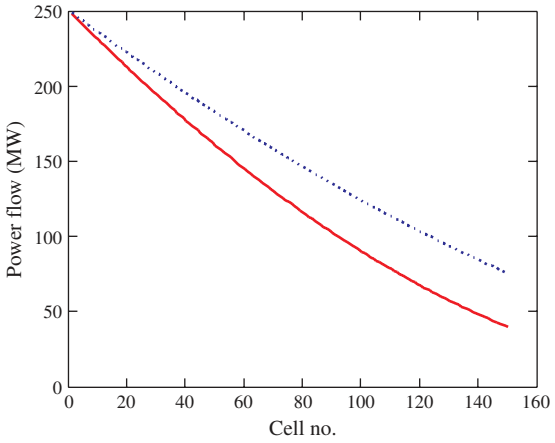

Fig. 2.19: *Power flow in MW along the structure as a function of cell number. The solid line is with beam and the dotted without.*

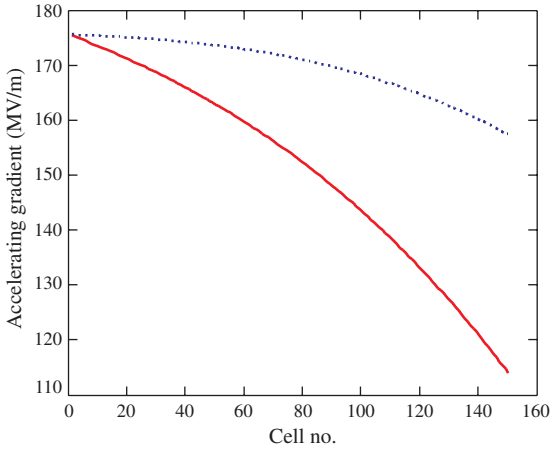

Fig. 2.20: *Accelerating gradient in MV/m as a function of cell number. The solid line is with beam and the dotted without.*

A number of methods have been developed to calculate the transverse wakefield of the TDS (Fig. 2.21). These include an uncoupled circuit model, a semi-coupled time domain model, a complex-wave number model and a double-band circuit model described in Refs. [2.24] and [2.25]. The validity of the analysis and of the TDS design has been directly demonstrated by the measurement of a 15 GHz structure at the ASSET facility at SLAC [2.26] (Fig. 2.22). However, the recent observation in CTF2 of unexpected surface damage at relatively low accelerating gradient (~ 60 MV/m) in these high group velocity structures (Table 2.10) is a cause for concern. It is not clear at the moment whether this can be attributed to the geometry of the structure or to contributing factors such as vacuum level or conditioning procedure.

The damping waveguide load must simultaneously be well-matched down to near the waveguide cut-off frequency, compact, vacuum-compatible, and compatible with assembly by brazing of the accelerating structure [2.27]. A low reflection coefficient (Fig. 2.23) is obtained by using a taper of silicon carbide (Fig. 2.24). The performance of the load near the cut-off is improved by tapering *inwards* the damping waveguide at the point at which the load begins. In this way the impedance change caused by the SiC is partially compensated by the impedance change of the narrowing waveguide. The current load design has been optimized using HFSS and has an overall length of 10 mm.

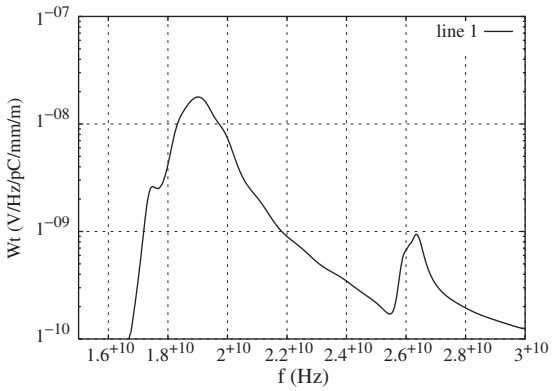

Fig. 2.21: Transverse wake spectrum.

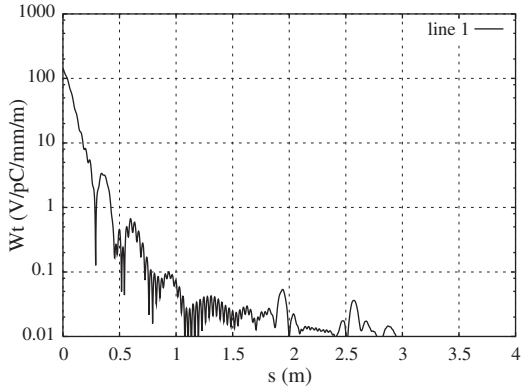

Fig. 2.22: Transverse wake of the TDS with the 10 mm load, as computed by the double-band circuit model (N.B. the computation has been made for a 15 GHz structure).

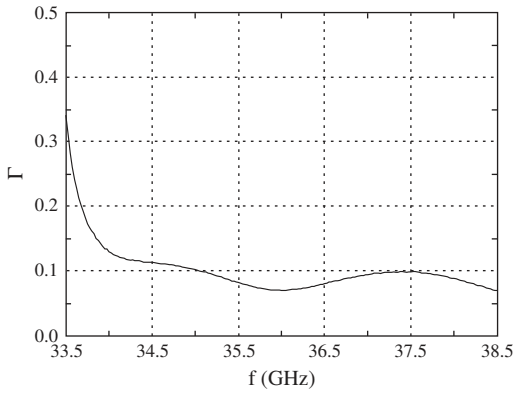

Fig. 2.23: Measured reflection coefficient of the load Γ as a function of frequency.

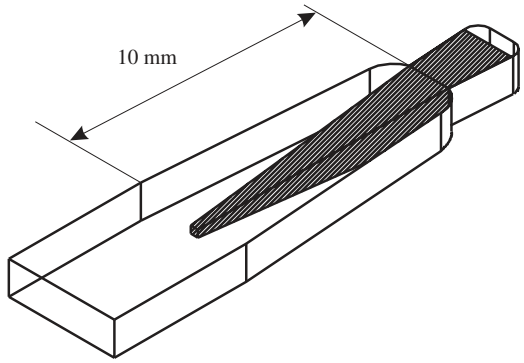

Fig. 2.24: Detail of the TDS load. The load is 2 mm wide at its base and 0.2 mm square at the tip.

2.4 Main-beam delivery

2.4.1 Function and length of the beam delivery

The main part of the beam-delivery line is the final-focus system which is characterized by a very large de-magnification. This means that the linear optics is dominated by the chromatic aberrations in the quadrupole doublets involved, aberrations which should be corrected by a minimal number of sextupoles separated from the quadrupoles by adequate betatron phases. In addition, in order to preserve the cleanness of the colliding beams and to limit backgrounds and losses, the beam halo has to be eliminated by collimation before the interaction region.

Consequently, a so-called *conventional* main-beam delivery complex is made of three major subsystems which follow one another in the delivery line and are as independent as possible. Following the beam after its extraction from the main linac, the first subsystem is the collimation section made of several collimators separated by adequate betatron-phases and located at positions where the β-amplitudes are large to keep low beam densities at the absorbers. Momentum collimation requires non-zero dispersion and dipole magnets in addition. All these needs lead to a section length which may be large and scales up with the collision energy. The second subsystem is the chromatic correction section which typically contains a minimum of two pairs of non-interleaved sextupoles and dipoles for generating some dispersion. Again this system requires high β-values at the sextupoles and may extend over a long distance which increases with the energy. The last subsystem is the telescope of the final focus, the length of which depends on the de-magnification, the required beam-size at the IP and the synchrotron radiation effect in the last doublet, which is linked to the beam energy and the length of the free space left between the two final doublets. In addition, and to be complete, a betatron-matching section in front of the chromaticity correction subsystem and an insertion for diagnostics might be necessary.

Such a basic beam-delivery line has been studied in detail for the Next Linear Collider (NLC) [2.28], and also for the Japan Linear Collider (JLC-I) [2.29] and TESLA [2.30]. In this context, laws for scaling the length of the different subsystems with the beam energy have been proposed [2.31]. Scaling from 1.5 to 3 TeV with the relative-energy variable $U_r = E$ (TeV)/1.5 and assuming a vertical β-function amplitude at the IP of the order of 0.1 mm, the law which has been obtained writes:

$$L_{BD}\ (\mathrm{km}) = [L_{FF}] + [L_{COLL}] = [0.8(1 + U_r) + 2.4U_r^{3/2}] + [6U_r] \quad ,$$

where L_{BD} represents the total length (both sides of the IP) of the beam-delivery line and where the parts due to the final focus (FF) and to the collimation system (COLL) are separated.

Starting from this basic design, modifications have been worked out in other studies [2.32]. As a major difference, an asymmetric dispersion has been proposed in order to concentrate the sextupole chromatic effects into the second sextupole of the pair, which tends to reduce chromogeometric aberrations. Another change consists of using non-linear magnetic field elements in the collimation subsystem in order to limit the betatron amplitude there and reduce the chromaticity and the section length. With these modifications, the law proposed [2.33] for the scaling of the length from 0.5 to 3 TeV and written for a different relative-energy variable $U_r = E$ (TeV)/0.5 looks as follows:

$$L_{BD}\ (\mathrm{km}) = [L_{FF}] + [L_{COLL}] = [U_r] + [1.6U_r^{1/2}] \quad ,$$

where the starting length comes from the 0.5 TeV design of the JLC beam delivery.

At 3 TeV, the first law gives a total length of the order of 21 km and the second of 10 km (value given in Fig. 1.1). More precise evaluation of the space needed can result only from design studies; the present status of the baseline design of the beam delivery is given below, more investigations remaining necessary.

The baseline proposed for the ensemble telescope and chromaticity-correction section, called final focus in Section 2.4.2.1, has a total length of 6.2 km (Fig. 2.25). Since the system studied includes the concept of asymmetric dispersion, this should be compared to the result of the second scaling law after ignoring the term linked to the collimation. The two values are remarkably consistent, for this law gives L_{FF} = 6 km.

A further significant reduction of the total final-focus length (both sides added) is only possible if the chromaticity correction is applied locally near the last doublets (the main source of chromaticity). There are essentially two ways which can be envisaged to achieve this. The first one, or *short* final-focus scheme [2.34], is based on the generation of some finite dispersion across the final doublet (but of zero amplitude at the IP) and on the addition of sextupoles close to the doublet quadrupoles in order to compensate their chromaticity. The second one, or *'ultra-short'* final-focus scheme [2.35], relies on the use of microwave quadrupoles placed near the magnetic quadrupoles of the doublet and playing a role similar to the one of the sextupoles, in the presence of a correlation between the momentum and the position along the bunch. The applicability of these schemes to CLIC at 3 TeV has still to be investigated before they can be adopted; in particular, questions related to the presence of finite dispersion, to flexibility and orthogonal tuning of the parameters in the first case, and to the tight tolerance about the energy variations required in the second.

2.4.2 Baseline design

2.4.2.1 Final focus

The task of the final-focus system is to focus the two main beams to the transverse design spot sizes of 43 nm and 1 nm at the interaction point (IP), where the opposing beams are collided. The momentum bandwidth of the final-focus system should be of the order of 1% in order to accommodate the expected beam energy spread from the linac. Tolerances on magnet position and field stability are another critical issue in the final-focus design. Both optics development and tolerance analysis for the CLIC final-focus made use of the design program FFADA [2.36].

A baseline optics of a 3-TeV final-focus system is shown in Fig. 2.25. It consists of horizontal and vertical chromatic correction sections (CCX and CCY) followed by a final transformer. The total length is 3100 m per side.

The final transformer, made from two quadrupole doublets, demagnifies the beam by a factor 15 horizontally, and 50 vertically. The gradient of the final quadrupole is taken to be 450 T/m. For comparison, the gradient achieved in an NLC permanent magnet prototype was 500 T/m [2.37]. For a large-aperture superconducting quadrupole the gradient would be a 30% increase from present design values of 320 T/m [2.38]. With the assumed quadrupole gradient, the chromaticity of the final doublet is 6900 in the horizontal and 27 000 in the vertical plane, where

chromaticity is defined as the relative spot-size increase (added in quadrature) divided by the r.m.s. energy spread. The beta functions at the entrance to the final quadrupole of 15 km horizontally and 88 km vertically correspond to r.m.s. beam sizes of 59 μm and 24 μm for the nominal CLIC parameters. This translates into a beam stay-clear of 50–140 σ for a permanent magnet with 3.3-mm bore radius and of 450–1100 σ for a superconducting quadrupole with 2.7 cm radial aperture.

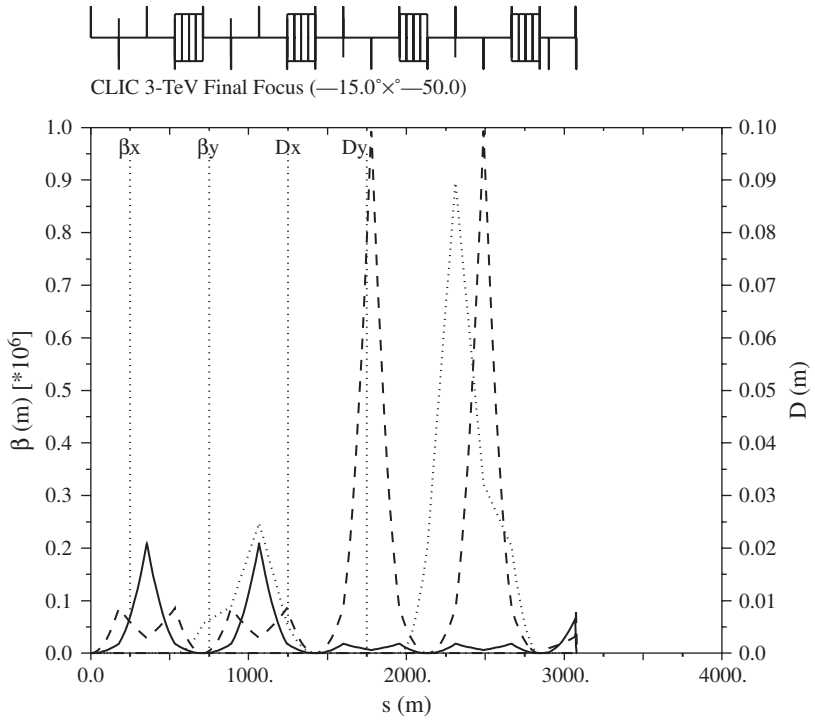

Fig. 2.25: *Beta function and dispersion for the 3-TeV baseline final-focus system, plotted as a function of the longitudinal position. The interaction point is on the right.*

The large chromaticity of the final doublet is compensated in the two chromatic correction sections. Each of these comprises a pair of sextupoles, separated by a *–I* transformation and placed an integer multiple of π in betatron phase apart from the final doublet. The dispersion function is nonzero only at the second sextupole of each pair. An odd-dispersion optics like this [2.39] has two advantages: (1) it reduces the number of bending magnets and the amount of synchrotron radiation by a factor of 2, and (2) it avoids many of the fifth-order chromogeometric aberrations arising from the chromatic breakdown of the *–I* between the sextupoles, which limit the momentum bandwidth. Thanks to the *–I* separation the individual sextupole pairs do not generate third-order geometric aberrations. The second-order dispersion from the CCX is adjusted to cancel the second-order dispersion produced in the CCY. The ratio of dispersion values, or, alternatively, the ratio of bending angles in CCX and CCY is thus constrained.

In the present design the net bending angles for the dipole regions in CCX and CCY are 63 μrad and 230 μrad, respectively. The peak beta functions at the CCY sextupoles are about 1000 km, and the maximum value of the dispersion is 0.1 m.

The achievable luminosity is calculated with the FFADA code, which tracks two random sets of particles through the entire system to the interaction point, using MAD, and then convolves them on a grid. The luminosity was maximized for a 1% flat energy spread by varying the total length, the ratio of CCX and CCY lengths, the bending angles, and the strengths of the last two quadrupoles. Figure 2.26 displays the luminosity of the optimized system as a function of the full-width momentum spread, assuming a flat energy distribution. For the expected energy spread, close to 1%, the luminosity (without pinch) is about 80% of the ideal luminosity that would be attained for a perfectly linear and achromatic optics. Figure 2.27 depicts the dependence of the transverse r.m.s. spot sizes on the energy spread. The vertical spot size is about 30% larger than the ideal linear value, the blow-up being due to synchrotron radiation (SR) in the second-to-last quadrupole magnet Q2. The horizontal spot size for small energy spread is close to the ideal value, but it increases rapidly with increasing energy spread. The strength of Q2 has been adjusted such that for 1% energy spread the horizontal blow-up is similar in magnitude to the vertical one. Hence, the final parameter choice is a trade-off [2.40] between Oide effect [2.41],[2.42] (vertical beam size increase due to

synchrotron radiation in the last quadrupoles, favouring a weak second-to-last magnet Q2) and the momentum bandwidth in the horizontal plane (demanding a small horizontal chromaticity and, thus, a strong quadrupole Q2).

The initial beta functions, at the entrance of the CCX, are about 1 m in both planes. Since the typical beta functions at the end of the linac are 18–65 m, an upstream beta-matching section will be required.

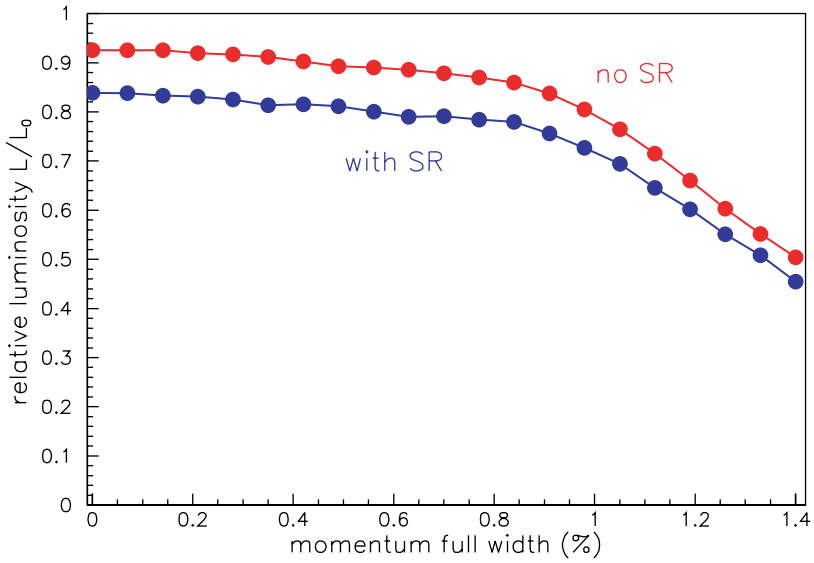

Fig. 2.26: *Relative luminosity loss as a function of the full-width energy spread for a flat distribution. The luminosity was calculated by tracking two random distributions of 5000 particles through the final focus to the interaction point (IP) and there convolving them on a grid, not including beam–beam focusing forces. The ideal reference luminosity is* $L_0 = 4.6 \times 10^{34}\ cm^{-2}\ s^{-1}$.

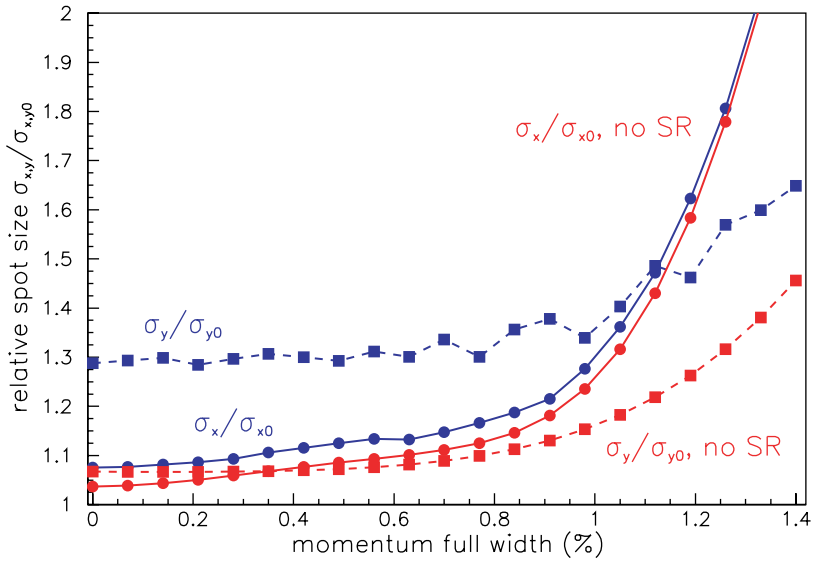

Fig. 2.27: *Relative r.m.s. spot sizes as a function of the full-width energy spread for a flat distribution. The ideal linear spot sizes are* $\sigma_x = 43$ *nm and* $\sigma_y = 1.0$ *nm.*

Figure 2.28 displays jitter and drift tolerances for the horizontal and vertical magnet positions. The jitter tolerances apply to pulse-to-pulse time scales. The tightest jitter tolerance is 0.2 nm for the last quadrupole. The drift tolerances refer to a time scale of several minutes and are of the order of 100 nm.

In Fig. 2.29, we present the tolerances on the magnet pitch angle and on the relative field stability. For the final quadrupole, the pitch jitter tolerance is 0.1 nrad. Typical field stability tolerances are 10^{-5}, a value close to specifications for the LHC power supplies [2.43].

Finally, it should be noted that a large crossing angle of 20 mrad (total) is required to suppress the multibunch kink instability by parasitic collisions around the IP and to provide sufficient space for the spent beam and collision debris, in particular for the opposite-charge pairs [2.44]. This means that crab-crossing cavities will have to be used to avoid a reduction of luminosity. However, the tolerance on the relative phase of the cavities is approximately 0.06° at 30 GHz (for a few per cent loss of L).

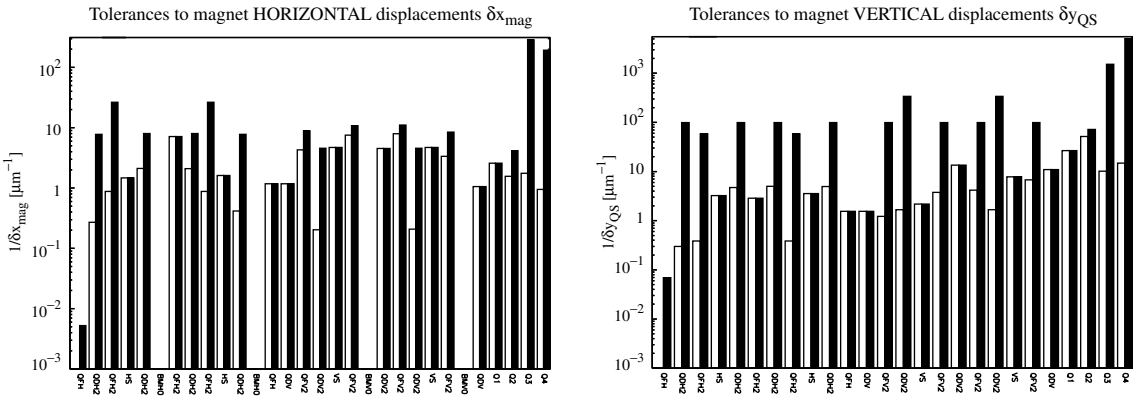

Fig. 2.28: *Displacement sensitivities for 2% luminosity loss, calculated with the FFADA code. The full bars represent pulse-to-pulse 'jitter' tolerances, due to both the induced orbit motion and the spot-size increase at the interaction point. This jitter can be corrected within a few pulses using a fast orbit feedback. The tightest jitter tolerances are about 3 nm (x) and 0.2 nm (y). The open bars are 'drift' tolerances referring to increases in the IP beam size only. Since the beam size tuning will be performed only every couple of minutes, the drift tolerances must be met over a longer time-scale. Drift tolerances are of the order of 100 nm.*

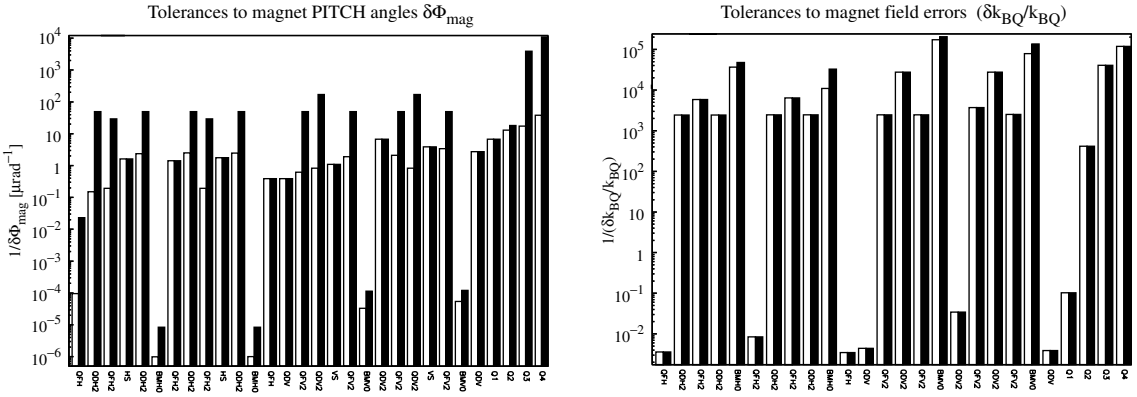

Fig. 2.29: *Sensitivities to pitch angle (left) and relative field changes (right), calculated with the FFADA code. Again, the full and open bars represent jitter and drift tolerances, respectively. The tightest pitch angle jitter tolerance is 0.1 nrad for the final quadrupole. Field stability tolerances are about 10^{-6}.*

2.4.2.2 Collimation system

The collimation system should serve two different purposes: (1) remove the beam halo which otherwise would cause unacceptable background in the particle-physics detector, and (2) protect the downstream systems against the impact of a missteered beam. Point (1) is achieved if the collimator shadows the final doublet apertures on the incoming side. To this end, the collimation aperture should be about 25 σ horizontally and 80 σ vertically [2.45], in case the final quadrupole is a permanent magnet, or 400 σ and 1000 σ for a superconducting final quadrupole with a large bore. The apertures on the outgoing side need not be shadowed by the collimation, since the incoming halo is tiny compared with the wide-angle debris coming from the collision point [2.46].

If a first beam-halo collimation is performed prior to injection into the main linac, the halo at the entrance to the final focus, due to all known scattering sources, is estimated to be of the order of only 10^3 or 10^4 particles per bunch [2.47] and [2.48]. Thus there may not be a need for a dedicated separate collimation section. Instead the collimators might be installed in the final focus itself, since for every few 10^4 scraped particles a single muon is generated, and the detector should be able to cope with several hundred muons passing it per bunch train. Collimation in the final focus will considerably shorten the overall system length, and, in addition, it will profit from the naturally large final-focus beta functions.

The collimators survive the impact of one entire bunch train if the following condition is fulfilled: $\sigma_{UTS} > \alpha E/C_p \, dE/dm$, where σ_{UTS} is the ultimate tensile strength, α the linear thermal expansion coefficient, C_p the heat

capacity, E the elastic modulus, and dE/dm the energy loss per gram of material. This condition can be rewritten as $\sigma_x\,\sigma_y > \alpha\,E/(\sigma_{UTS}\,C_p)\,\mathrm{d}E/\mathrm{d}x\,k_b\,N_b/(2\pi)$ where dE/dx is the loss of energy per unit of length. Assuming a copper collimator, with $E = 120$ GPa, $\alpha = 1.7 \times 10^{-5}$ K^{-1}, $C_p = 0.385$ Jg^{-1} K^{-1}, $\mathrm{d}E/(\rho\mathrm{d}x) = 1.44$ MeV cm^2 g^{-1} (ρ = material density), and $\sigma_{UTS} = 300$ MPa, we find $(\sigma_x\,\sigma_y)^{1/2} > 200$ μm, or $\beta_{x,y} > 1000$ km. Materials with a smaller product αE would be better suited for collimation. We are studying the possible use of carbon composites. For many conceivable failure modes, the emittance of a missteered beam will be significantly blown up in the linac, and a smaller β-function would suffice.

As a back-up option we may investigate a nonlinear collimation system *à la* KEK [2.49] or TESLA [2.48]. Also such a nonlinear collimation could be integrated into the final focus, e.g., utilizing the sextupoles in the two chromatic correction sections.

In addition, we are considering the installation of high-impedance structures for passive machine protection. In this scheme a missteered off-centre bunch will excite a wakefield in the high-impedance structure that spoils the bunch emittance and also deflects subsequent bunches. Both effects would increase the area of beam impact on a downstream collimator, thereby ensuring its survival.

2.4.2.3 Exit line

The task of the exit line is to remove the spent beam and debris from the interaction region, simultaneously ensuring acceptable background in the detector and not causing any vibrations of the final-doublet quadrupoles.

Design of the beam exit line is a major challenge, as the outgoing beam has an energy spread of 100%, and there are copious beamstrahlung photons, carrying a third of the initial beam power, and almost as many coherent pairs as incoming particles [2.50]. Low-energetic pairs of both charge signs might spiral around the solenoidal field and hit apertures between incoming and outgoing quadrupole magnets. The impact of only a small fraction of the incoming beam power near the final quadrupole can induce elastic waves with amplitudes well in excess of the 0.2 nm vertical jitter tolerance [2.51]. Neutron generation in the vicinity of the detector is a further concern. Large apertures should be chosen in order to guide as much of the collision debris as possible away from the IP. The ideal quadrupole magnet might be a double-quadrupole with an open centre, similar in its layout to the magnets built for the LHC cleaning insertions [2.52].

2.4.3 Machine–detector interface - beam–beam interaction

Because of the small spot size at the interaction point, the colliding bunches produce strong electromagnetic fields focusing each other. While this enhances luminosity, the beam particles travel on curved trajectories, emitting beamstrahlung, which is comparable to synchrotron radiation. In the machines with centre-of-mass energies of up to 1 TeV the critical energy of this radiation is below the beam energy, but this is not the case at $E_{CM} = 3$ TeV.

The beam–beam effects were simulated using GUINEA-PIG [2.53]. The beamstrahlung has a total power of about $P = 4.6$ MW, but it is emitted into small cones in the forward direction so it does not cause direct background. However, protection of the magnets in the spent beam line is an issue which has not yet been investigated. Also secondary particles — especially neutrons — are of concern.

The beam–beam interaction will also cause background via coherent and incoherent pair creation. In the coherent process, a hard beamstrahlung photon turns into an electron–positron pair in the strong field of the oncoming bunch. About 6.8×10^8 pairs are produced per bunch crossing [2.54]; a number comparable to the number of beam particles. Thus these particles influence the beam–beam interaction significantly. Initially they have small angles but they can be deflected by the beams. The detector can not be extended to very small angles in order to stay out of the flux of these particles. At larger angles it can be protected from most of their secondaries with the help of a mask. However, secondary neutrons produced inside of the mask potentially lead to significant background [2.55]. In order not to produce the neutrons in the first place it is therefore necessary to allow an exit hole with an opening angle of about 10 mrad [2.50]. In this case the energy deposited per bunch crossing in the final quadrupoles is comparable to the value expected for TESLA. The number of particles produced via the incoherent process is much smaller than the number of particles in the bunch (about 4.5×10^5), but they can have significant inherent angles. They can enter the detector causing background — especially in the vertex detector, which integrates over a full train. The longitudinal magnetic field of the main detector solenoid helps to reduce the number of hits. For $B_z = 4$ T a minimum radius of 30 mm for the inner layer of the detector seems possible, with a hit density of less than one charged hit per mm^2 and bunch train. The background processes can be used as a fast signal for tuning the luminosity [2.56].

The number of hadronic background events per bunch crossing is high, about four events with a centre-of-mass energy above 5 GeV [2.54]. Their effect on the physics needs to be investigated.

2.5 Micro-alignment system

Transverse alignment tolerances of about 10 µm (r.m.s.) are required for the main linac in order to limit the emittance blow-up due to transversely deflecting wakefields to reasonable values. The entire accelerator is mounted on a concrete base grounded to the floor. This base runs the full length of the tunnel (Fig. 1.2). An active alignment system using precision micro-movers is proposed to achieve these tight tolerances. The accelerating structures and beam-position monitors of each linac are supported by precisely pre-aligned V-blocks sitting on SiC girders. The ends of two adjacent girders are connected by swivel-joint link rods to a common platform that is driven by three remote-controlled 0.1 µm resolution stepping motors. The length of one girder is 2.23 m. The quadrupole supports are independent of the girder supports and are driven by five identical stepping motors. The quadrupole support platforms are located above the girders. Aligning the linac in this case means aligning the articulation points of the girders, and the magnetic components. The articulation points are equipped with, and aligned by, an overlapping optical off-set measurement system (RASNIK). This system ensures a relative precision between articulation points of the order of about 1 µm over distances of a few metres. At intervals of about 36 m (16 girders), the articulation points are attached via sensors to a stretched wire positioning system (WPS) which assures a relative precision of 10 µm over distances of about 200 m. The WPS consists of two stretched wires running parallel to the linacs and overlapping over half their own length. To be able to consider the wire as a reference in the vertical plane it is necessary to determine the catenary of the wire with great accuracy. The RASNIK system is preferred to the WPS for local positioning of the girders (within the 36 m intervals) because it is considerably cheaper. All magnetic elements are equipped with two-axes tilt monitors [making up the tilt monitoring system (TMS)] and with WPS sensors, and are positioned using the stretched wire. The WPS itself is attached to precision support plates which sit on the concrete block at 16-girder intervals (35.68 m). These precision plates also support a hydrostatic levelling system (HLS) which provides the reference for all height measurements and in particular for the measurement of the catenary of the wire. The corresponding geometrical reference networks are schematically shown in Fig. 2.30.

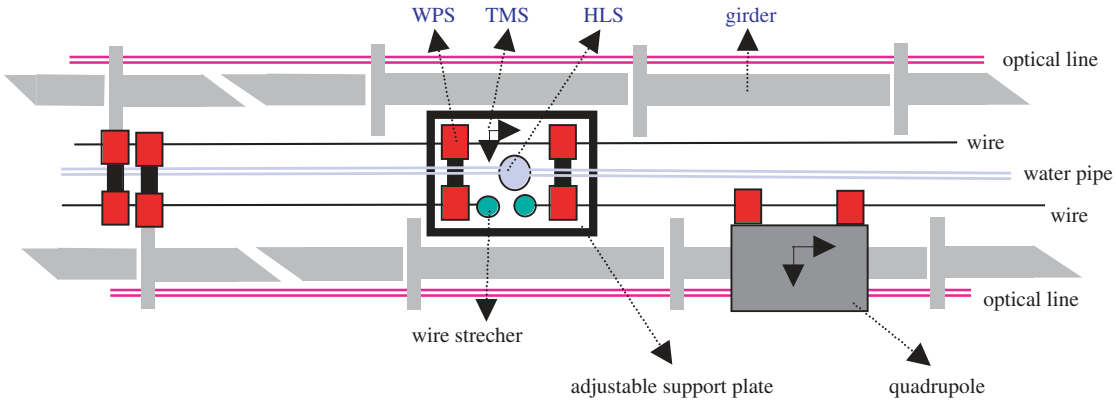

Fig. 2.30: *Schematic plan view of the two geometrical reference networks.*

The support plates have standard CERN reference bore holes which enable them to be positioned with classical surveying techniques to a relative precision of about 0.1 mm. This classical part is done during the civil engineering stage in the following way. First, a system of reference pillars is created outside the tunnel, on the surface along the projected line of the linacs, at intervals of about 3.6 km using global positioning surveying techniques (GPS) with an absolute precision of about 1cm and a relative precision of about 1mm. These surface pillars are then used to create a set of underground reference pillars with the same relative precision (~1 mm) using vertical drop techniques. The underground pillars are themselves then used to create a set of temporary civil engineering reference pillars using gyroscopic and distance techniques, which are built at intervals of about 36 m along the length of the linac as the tunnelling work progresses. This temporary reference system is used to position the above-mentioned reference support plates on the concrete base to a precision of about 1 cm. The last step is to use adjustment screws on the support plates to position the plates with respect to the underground reference pillars to a precision of about 1 mm and a relative precision of 0.1 mm. All the instruments measuring these networks during this pre-alignment stage continuously provide information to a computer system which, following a statistical analysis, calculates the actual positions of the components, and then deduces and controls the movements to be made. Once the linacs have been pre-aligned in this way, beam is injected into the machine, and the more accurate signals produced by the sub-micron-resolution beam-position monitors take over the alignment process. The measuring system used for pre-alignment, however, remains active in the background to provide a position memory of the components so that the pre-alignment condition can be reinstated for beam start-up after a shutdown.

References

Injection system (Section 2.2)

Overall injection complex (Section 2.2.2)

[2.1] L. Rinolfi, A CLIC injector complex for the main beams, CLIC Note 354 (1997).

[2.2] J. Condoning, Polarized RF guns, SLAC-PUB-7854 (1998).

[2.3] The NLC Design Group, Zeroth Order Design Report for the Next Linear Collider, SLAC Report 474 (1996), p. 89.

[2.4] R. Chehab, X. Artru, R. Kirsch, B. Johnson, P. Keppler, J. Major, L. Rinolfi and A. Jejcic, Radiation damage study of a monocrystalline tungsten positron converter, CLIC Note 369 (1998), LAL/RT 98–02, CERN/PS 98–17(LP), Proc. 6th Eur. Part. Accel. Conf. (EPAC98), Stockholm, 1998, Eds. S. Myers, L. Liljeby and C. Petit-Jean-Genaz (IOP, Bristol, 1999), p. 1394.

Damping rings (Section 2.2.4)

[2.5] J.-P. Potier and T. Risselada, Fundamental design principles of linear collider damping rings, with an application to CLIC, EPAC2000, Vienna, June 2000.

[2.6] J.-P. Potier and L. Rivkin, A low emittance lattice for the CLIC damping rings, Proc. 17th IEEE Part. Accel. Conf. (PAC97), Vancouver, 1997, Eds. M. Comyn, M.K. Craddock, M. Reiser et al. (IEEE, Piscataway, N. J., 1997), 3 vols., p. 476.

Bunch compressors and transfer lines (Section 2.2.5)

[2.7] E.T. D'Amico, G. Guignard and T.O. Raubenheimer, How to obtain a bunch length of 50 mm in the CLIC main linac, CLIC Note 355 (March 1998).

[2.8] E.T. D'Amico, G. Guignard and T.O. Raubenheimer, The CLIC main linac bunch compressor, Proc. 6th Eur. Part. Accel. Conf. (EPAC98), Stockholm, 1998, Eds. S. Myers, L. Liljeby and C. Petit-Jean-Genaz (IOP, Bristol, 1999).

[2.9] E.T. D'Amico and G. Guignard, First-order design of a new type of isochronous arc, CERN SL/95–120 (1997).

Main linac (Section 2.3)

The main linac lattice (Section 2.3.1)

[2.10] D. Schulte, Emittance preservation in the main linac of CLIC, Proc. 6th Eur. Part. Accel. Conf. (EPAC98), Stockholm, Eds. S. Myers, L. Liljeby and C. Petit-Jean-Genaz (IOP, Bristol, 1999) and CERN-PS 98–018-LP (1998).

[2.11] D. Schulte, I. Syratchev, Beam loading compensation in the main linac of CLIC, to be published in Proc. Lin. Accel. Conf. (LINAC2000), Monterey, 2000.

[2.12] A. Millich, Computations of wakefield for CLIC DLWG, CLIC Note 137 and CERN–SL/91–27 (CO) (1991).

Static trajectory correction (Section 2.3.2)

[2.13] T.O. Raubenheimer and D. Schulte, The ballistic alignment method, Proc. Part. Accel. Conf. (PAC99), New York, 1999, Eds. A. Luccio and W. MacKay (IEEE Computer Soc. Press, Piscataway, N. J., 1999) and CERN-PS 99–024-LP (1999).

[2.14] J.H. Sladen, I. Wilson and W. Wuensch, CLIC beam position monitor tests, CERN-PS/96–029 (LP) (1996).

[2.15] D. Schulte, The CLIC main linac lattice at 1 TeV, CLIC Note 356 (1998).

[2.16] D. Schulte, The tracking code PLACET, to be published, draft in http://home.cern.ch/dschulte/Placet.html.

[2.17] E.T. D'Amico and G. Guignard, Multi-step lining-up correction of the CLIC trajectory, Proc. Part. Accel. Conf. (PAC99), New York, 1999, Eds. A. Luccio and W. MacKay (IEEE Computer Soc. Press, Piscataway, N. J., 1999).

[2.18] T.O. Raubenheimer, The generation and acceleration of low emittance flat beams for future linear colliders, SLAC Report 387 (1991).

[2.19] E.T. D'Amico and G. Guignard, A trajectory correction based on multi-step lining-up for CLIC main linac, CLIC Note 400 (April 1999).

[2.20] G. Guignard and J. Hagel, MUSTAFA environment description and users's guide with applications to CLIC, CLIC Note 349 and CERN–SL 98–02 (1998).

Time-dependent effects (Section 2.3.3)
[2.21] D. Schulte, Simulations of an intra-pulse interaction point feedback for NLC, CLIC Note 415 (1999).

Emittance balance (Section 2.3.4)
[2.22] E.T. D'Amico, G. Guignard and D. Schulte, CLIC main linac beam simulations, Proc. of VIIIth Int. Workshop on Linear Colliders (LC99), Frascati, 1999, Eds. J.-P. Delahaye, G. Guignard, K. Hübner et al., URL: http://wwwsis.lnf.infn.it/talkshow/lc99/Guignard2b/talk.pdf

The main linac accelerating structure (Section 2.3.5)
[2.23] M. Dehler, I. Wilson and W. Wuensch, A tapered damped accelerating structure for CLIC, Proc. 19th Int. Lin. Accel. Conf. (LINAC'98), Chicago, 1998, URL: http://www.aps.anl.gov/conferences/LINAC98/papers/TH4083.pdf
[2.24] M. Dehler, Modeling a 30 GHz waveguide loaded detuned structure for the Compact LInear Collider (CLIC), CERN/PS RF 98–09 (1998).
[2.25] W. Wuensch, Calculation of the transverse wake function of a highly damped periodic structure, Proc. Part. Accel. Conf. (PAC99), New York, 1999, Eds. A. Luccio and W. MacKay (IEEE Computer Soc. Press, Piscataway, N. J., 1999).
[2.26] I. Wilson et al., A Test of the CLIC multibunch accelerating structure in ASSET, Proc. Eur. Part. Accel. Conf. (EPAC2000), Vienna, June 2000.
[2.27] M. Luong, I. Wilson and W. Wuensch, RF loads for the CLIC multibunch structure, Proc. Part. Accel. Conf. (PAC99), New York, 1999, Eds. A. Luccio and W. MacKay (IEEE Computer Soc. Press, Piscataway, N. J., 1999).

Main-beam delivery (Section 2.4)

Function and length of the beam delivery (Section 2.4.1)
[2.28] The NLC Design Group, Zeroth order Design Report for the Next Linear Collider, SLAC Report 474 (1996).
[2.29] JLC Group, JLC-I design, KEK Report 92–16 (1992).
[2.30] Conceptual Design of a 500 GeV e^+e^- Linear Collider with Integrated X-ray Laser Facility, Eds. R. Brinkmann, G. Materlik, J. Rossbach and A. Wagner, DESY 1997–048 (1997).
[2.31] T.O. Raubenheimer, private communication.
[2.32] N. Akasaka et al., JLC Design Study, High Energy Accel. Research Org., Tsukuba, Japan (1997), ftp://lcdev.kek.jp/pub/DesignStudy/
[2.33] K. Oide, private communication.
[2.34] P. Raimondi, A novel final focus design for future linear colliders, SLAC-PUB-8460 (2000).
[2.35] S. Fartoukh and J.-B. Jeanneret, A proposal to use microwave quadrupoles to shorten the beam delivery section of CLIC, CLIC Note 423 (1999).

Baseline design (Section 2.4.2)
[2.36] O. Napoly and F. Dunham, FFADA: computer design of final focus systems for linear colliders, Proc. Eur. Part. Accel. Conf. (EPAC94), London, 1994 (World Scientific, Singapore, 1994), vol. 1, p. 698.
[2.37] J. Spencer *in* Zeroth Order Design Report for the Next Linear Collider, C. Adolphsen et al., report submitted to Snowmass 1996, SLAC Report 474 (1996), Section 11.8.
[2.38] S. Caspi et al., Design of a Nb_3Sn high gradient low-beta quadrupole magnet,15th Int. Conf. on Magnet Technology, Beijing, China, 1997.
[2.39] K. Oide, Final focus system with odd dispersion scheme, Proc. 15th Int. Conf. on High Energy Accel., Hamburg, 1992, Ed. J. Rossbach (World Scientific, Singapore, 1993).
[2.40] O. Napoly, CLIC 3 TeV interaction region and final focus studies, CERN-SL 99–054 and CLIC Note 414 (1999).
[2.41] K. Oide, Phys. Rev. Lett. **61** (1988) 1713.
[2.42] K. Hirata, K. Oide and B. Zotter, Phys. Lett. **B224** (1989) 437.
[2.43] L. Barnett, D. Hundzinger, Q. King, Developments in the high precision control of magnet currents for LHC, Proc. Part. Accel. Conf. (PAC99), New York, 1999, Eds. A. Luccio and W. MacKay (IEEE Computer Soc. Press, Piscataway, N. J., 1999).
[2.44] R. Assmann et al., Design status of the CLIC 3-TeV beam delivery system and damping rings, Proc. 7th Eur. Part. Accel. Conf. (EPAC2000), Vienna, June 2000.
[2.45] O. Napoly, private communication (2000).

[2.46] R. Brinkmann, private communication (1999).
[2.47] H. Burkhardt, Background in future e^+e^- linear colliders, CERN-SL 057-AP and CLIC Note 416 (1999).
[2.48] R. Brinkmann, Estimate of beam halo for TESLA, Proc. of VIIIth Int. Workshop on Linear Colliders (LC99), Frascati, 1999, Eds. J.-P. Delahaye, G. Guignard, K. Hübner et al., URL: http://wwwsis.lnf.infn.it/talkshow/lc99/Brinkmann4a/talk.pdf
[2.49] N. Akasaka et al., JLC Design Study, KEK, Tsukuba (1997).
[2.50] D. Schulte, High energy beam–beam effects in CLIC, Proc. Part. Accel. Conf. (PAC99), New York, 1999, Eds. A. Luccio and W. MacKay (IEEE Computer Soc. Press, Piscataway, N. J., 1999) and CERN–PS 99–017 (1999).
[2.51] J.-B. Jeanneret and E. Wildner, Thermal and acoustic effects in CLIC beam absorbers, CERN–SL– 99–072 and CLIC Note 421 (1999).
[2.52] M. Giesch, Twin aperture quadrupoles for the LHC cleaning insertions, 14th Int. Conf. Magnet Technology, MT-14, Tampere, Finland, 1995, Eds. L. Kettunen, K. Forsman, A. Koski, R. Mikkonen [IEEE Trans. Magn. **32** (1996)].

Machine–detector interface - beam–beam interaction (Section 2.4.3)

[2.53] D. Schulte, Beam–beam simulations with GUINEA-PIG, International Computational Accelerator Physics Conference (ICAP98), Monterey, 1998 and CERN-PS 99–014-LP (1999).
[2.54] D. Schulte, Background at linear colliders, Workshop on the Development of Future Electron–Positron Colliders for Particle Physics Studies and for Research Using Free Electron Lasers, Lund, 1999, Eds. G. Jarlskog, U. Mjörnmark and T. Sjöstrand (Fysiska Inst. Lund, 1999), p. 59 and CERN–PS 99–069 (LP) (1999).
[2.55] D. Schulte, Study of the Electromagnetic and Hadronic Background in the Interaction Region of the TESLA Collider, Ph.D. thesis, TESLA 97–014, Univ. of Hamburg, Hamburg (1997).
[2.56] O. Napoly and D. Schulte, Luminosity monitor studies for TESLA, Proc. 19th Int. Lin. Accel. Conf. (LINAC98), Chicago, 1998 and TESLA 97–17 (1997).

3 Drive Beam and RF Power Source

3.1 Introduction

The CLIC study focuses on high-gradient, high-frequency (30 GHz) acceleration for multi-TeV linear colliders. Short RF pulses of high peak power are typically required in high-frequency linear colliders. In the case of CLIC, 130 ns long pulses at about 230 MW per accelerating structure are needed, but no conventional RF source at 30 GHz can provide such pulses. This leads naturally to the exploration of the two-beam acceleration technique [3.1], in which an electron beam (the drive beam) is accelerated using standard, low-frequency RF sources and then used to produce RF power at high frequency.

In linear collider projects based on conventional RF sources (klystrons), pulse compression or delayed distribution techniques are used in order to obtain the needed high peak power and short pulse length. Similar techniques can be used in two-beam accelerators. In the CLIC case, however, the compression and distribution are done with electron beams [3.2]. The main advantage of electron beam manipulation, with respect to manipulation of RF pulses, consists in the very low losses that can be obtained while transporting the beam pulses over long distances and compressing them to very high ratios. A further advantage is the possibility of frequency multiplication, achieved by interleaving bunched beams by means of transverse RF deflectors [3.3]. In the following we will describe the CLIC RF power source complex used to generate all the RF power needed for one of the two main linacs (electron or positron). Possibilities to combine some elements of both the e^+ and e^- complexes are under study. A schematic layout of one complex is shown in Fig. 3.1.

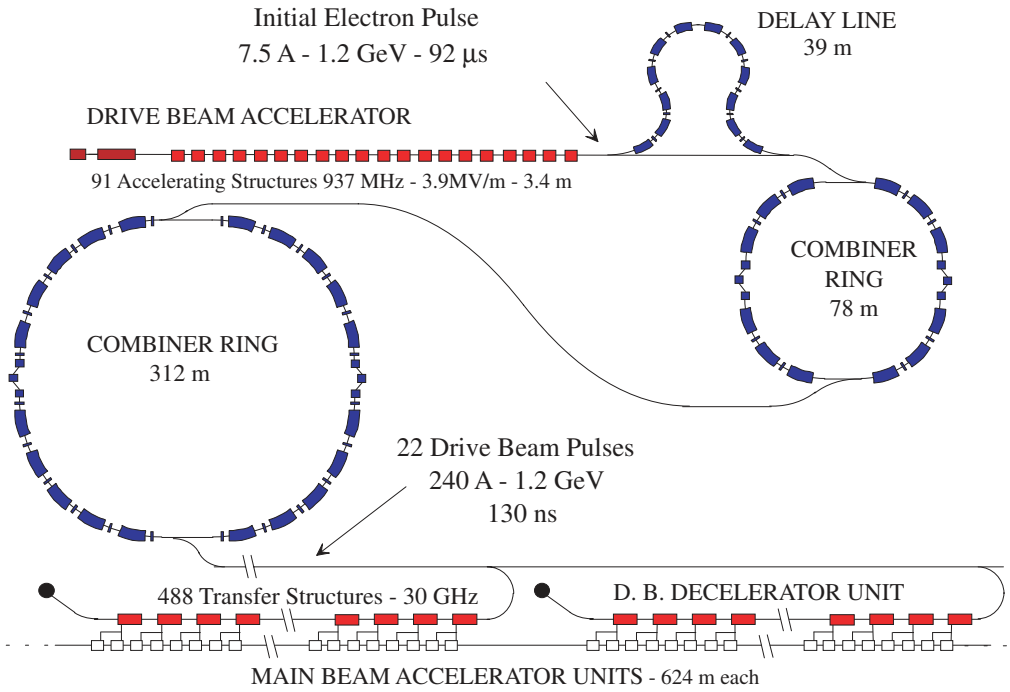

Fig. 3.1: *Schematic layout of the CLIC RF power source. Two such complexes (one for each of the main linacs) will be needed to provide the power for 3 TeV c.m. CLIC operation. Only two of the 22 decelerator/accelerator units composing a linac are shown.*

The CLIC RF power source can be thought of as a 'black box' that combines and transforms several long, low-frequency RF pulses into many short, high-power pulses at high frequency. During the process, the energy is stored in a relativistic electron beam, which is manipulated in order to obtain the desired time structure and then transported to the place where the energy is needed. The energy is finally extracted from the electron beam in resonant decelerating structures, which run parallel to the main accelerator and are called Power Extraction and Transfer Structures (PETS). The key points of the system are an efficient acceleration of the drive beam in conventional structures, the introduction of transverse RF deflectors to manipulate the drive beam, and the use of several drive-beam pulses in a counter-flow distribution system, each one powering a different section of the main linac. The primary characteristic of this scheme consists of using the energy stored in different time bins of a long electron-beam pulse to create the RF necessary for different sections of a long linac. Thus, the same accelerator and beam manipulation system is used to

create all the beam pulses needed for powering one of the two main linacs. The method discussed here seems relatively inexpensive, very flexible and can be applied to the beam-acceleration in various linear colliders over the entire frequency and energy range applicable.

The drive-beam generation complex is located at the centre of the linear collider complex, near the final-focus system. The energy for the RF production is initially stored in a 92 μs long electron beam pulse (corresponding to twice the length of the high-gradient, main linac) which is accelerated to about 1.2 GeV by a normal-conducting, low-frequency (937 MHz) travelling wave linac. The linac is powered by conventional long-pulse klystrons. A high-energy transfer efficiency is paramount in this stage. The drive beam is accelerated in relatively short structures (3.4 m long), such that the RF losses in the copper are minimized. Furthermore, the structures are fully beam-loaded, i.e., the accelerating gradient is zero at the downstream end of each structure and no RF power flows out to a load. In this way, about 98% of the RF energy can be transferred to the beam.

The beam pulse is composed of 32×22 subpulses, each one 130 ns long. In each subpulse the electron bunches occupy alternately even and odd buckets of the drive-beam accelerator fundamental frequency (937 MHz). Such a time structure is produced after the thermionic gun in a subharmonic buncher, whose phase is rapidly switched by 180° every 130 ns. This provides us with a means to separate the subpulses after acceleration, while keeping a constant current in the accelerator and avoiding transient beam-loading.

With nominal phase-switching times, the resulting pulse of the acceleration voltage is rectangular. By delaying the phase-switching time, it is also possible to obtain subpulses of different lengths. When the different subpulses are superimposed at the end of the combination process, one can thus obtain a current ramp of about 22 ns at the leading edge of the pulse. This in turn produces a ramp in the PETS power output, which is used for beam-loading compensation in the main linac. An illustration of this technique [2.11] is given in Fig. 3.2 under the assumption that only one combiner ring is used, folding the beam by a factor two only. If the phase-switching is delayed after the first two trains, the shape of the voltage pulse is not flat anymore. The trailing bunches which are located after the nominal switching time add to the train considered and consequently append to the tail of the final pulse. In the train which follows the delayed switching, the first few bunches are missing and this generates gaps at the head of the final pulse. This results in a variation of the density of bunches and therefore in a ramp of the current. The unwanted tail is of no concern since it goes through the drive-beam decelerator after the passage of the main beam.

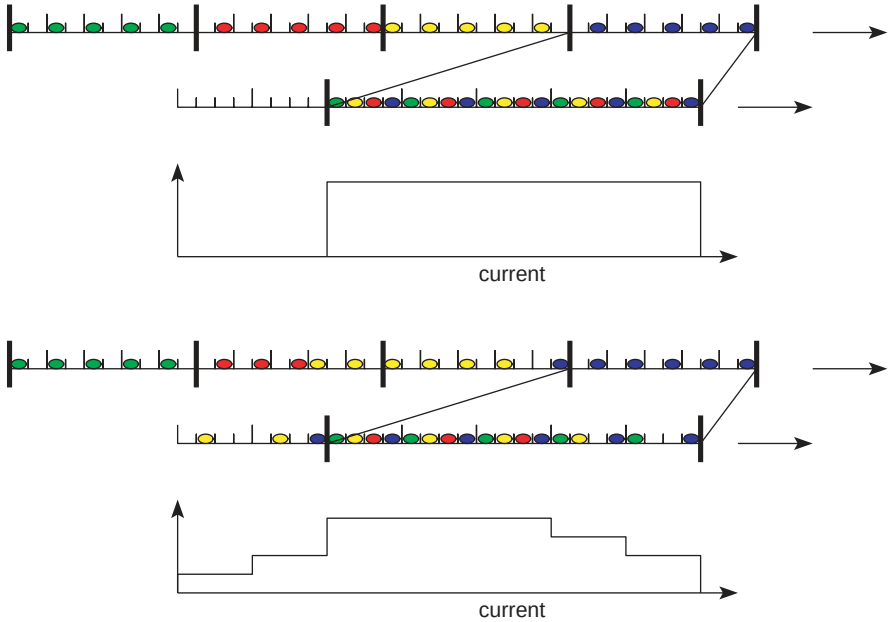

Fig. 3.2: *Illustration of the delayed switching scheme. In the upper case, the phase is switched at nominal times, creating a rectangular pulse. In the lower case, the phase shift is delayed in order to create a ramp of beam current.*

As the long pulse leaves the drive-beam accelerator, it passes through a delay-line combiner [3.2] where 'odd' and 'even' subpulses are separated by a transverse RF deflector at the frequency of 468.5 MHz. Each 'even' bunch train is delayed with respect to the following 'odd' one by 130 ns. The subpulses are recombined two-by-two by interleaving the electron bunches in a second RF deflector at the same frequency. The net effect is to convert the long pulse to a periodic sequence of drive-beam pulses with gaps in between. After recombination, the pulse is composed

of 16×22 subpulses (or trains) whose spacing is equal to the train length. The peak power and the bunch frequency are doubled.

The same principle of electron-bunch pulse combination is then used to combine the trains four-by-four in a first combiner ring, 78 m long. Two 937 MHz RF deflectors create a time-dependent local deformation of the equilibrium orbit in the ring. This bump is used for injection of a first train in the ring (all its bunches being deflected by the second RF deflector onto the equilibrium orbit). The ring length is equal to the spacing between trains plus $\lambda/4$, where λ is the spacing between bunches, equal to the wavelength of the RF deflectors. Thus, for each revolution period, the RF phase seen by the bunches circulating in the ring increases by 90°, and when the second train is injected, the first one does not see any deflection and its bunches are interleaved with the ones which are injected (at a $\lambda/4$ distance). This is repeated twice, then the four interleaved trains are extracted from the ring by an ejection kicker half a turn later, and the same cycle starts again. After the first combiner ring the whole pulse is composed of 4×22 trains.

The trains are combined again, using the same mechanism, in a second combiner ring, 312 m long, yielding another factor four in frequency multiplication, and obtaining the final 22 trains required for the main linac. At this point, each final train is 39 m long and consists of 1952 bunches with a charge of 16 nC/bunch and an energy of 1.18 GeV.

Such drive-beam pulses are distributed down the main linac via a common transport line, in a direction opposite to the direction of the main beam. The distance between trains is now 1248 m, corresponding to twice the length of the linac section which they will power, so that they will arrive at the appropriate time to accelerate a high-energy beam travelling in the opposite direction.

Pulsed magnets deflect each beam at the appropriate time into a turn-around. After the turn-around each pulse is decelerated in a 624 m long sequence of low-impedance Power Extraction and Transfer Structures (PETS) down to a minimum energy close to 0.12 GeV (Fig. 3.22), and the resulting output power is transferred to accelerate the high-energy beam in the main linac. As the main beam travels along, a new drive-beam train periodically joins it and runs in parallel but ahead of it to produce the necessary power for a 624 m long linac unit. At the end of a unit the remaining energy in the drive beam is dumped while a new one takes over the job of accelerating the main beam. The main characteristics of one drive-beam unit are given in Table 3.1.

Table 3.1: Main parameters of a drive-beam unit

Parameter	**Symbol**	**Value**
Drive-beam pulse		
Energy (initial)	$E_{\text{in,dec}}$	1.18 GeV
Energy (final, minimum)	$E_{\text{fin,dec}}$	118 MeV
Current	I_{dec}	240 A
Pulse duration (FWHH)	τ_{train}	130 ns
Charge/train	Q_{train}	31.25 μC
Total energy/train	W_{train}	36.9 kJ
Number bunches/train	$N_{\text{b,dec}}$	1952
Bunch charge	$Q_{\text{b,dec}}$	16 nC
Bunch separation	$\Delta_{\text{b,dec}}$	0.067 ns
Bunch length, r.m.s.	$\sigma_{\text{z,dec}}$	0.4 mm
Normalized emittance, r.m.s. (injection)	$\varepsilon_{\text{n,dec}}$	150 μm·rad
Decelerator unit		
Repetition rate	f_{rep}	100 Hz
Unit length (total)	$L_{\text{unit,tot}}$	624 m
Unit length (active)	$L_{\text{unit,act}}$	390 m
Number of PETS/unit	$N_{\text{PETS,unit}}$	488
Number of quadrupoles/unit	$N_{\text{quad,unit}}$	488
Decelerating gradient	G_{dec}	2.8 MV/m
Power extracted/metre	P_{out}	458 MW
Main beam energy gain/unit	ΔE_{main}	68 GeV

3.2 Drive-beam injector

3.2.1 Overview of the system

The basic scheme for the drive-beam injector has been further developed and adapted to the new parameter set. The total pulse, at the injector exit, is 92 µs (Fig. 3.3) and is composed of 32×22 subpulses as mentioned in Section 3.1. The time structure of this pulse is produced after the thermionic gun in a subharmonic buncher, in such a way that the electron bunches of each subpulse occupy alternately even and odd buckets (Fig. 3.3). This is indeed the requisite for subsequent separation of the subpulses, and their recombination in the combiner rings.

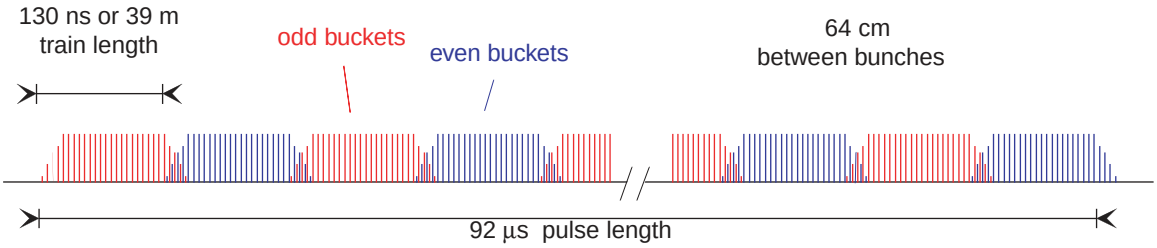

Fig. 3.3: *Combined pulses at the injector exit or linac entrance.*

Figure 3.4 shows a layout of the CLIC drive-beam injector. The latter is composed of five subsystems:
1) A thermionic gun; 2) A bunching system providing a bunched beam at 10 MeV; 3) An injector linac accelerating the beam up to 50 MeV; 4) A spectrometer line with beam diagnostic and collimation; 5) A matching section to the drive-beam accelerator.

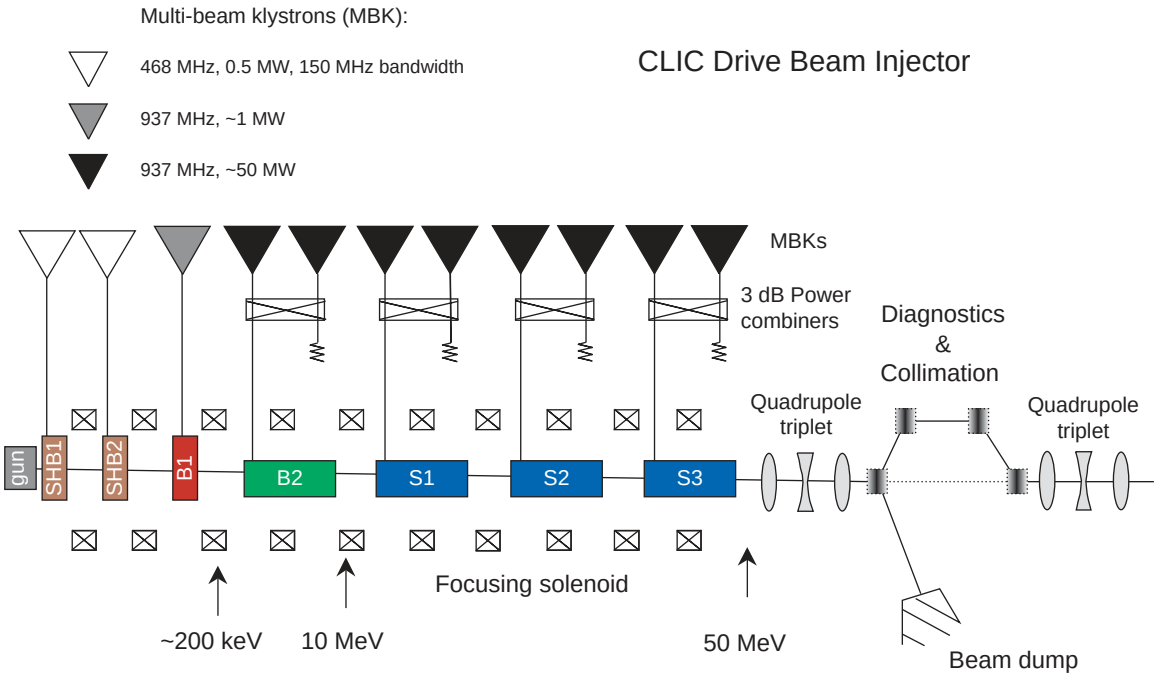

Fig. 3.4: *Layout of the CLIC drive-beam injector.*

The thermionic gun

The gun provides a beam at 200 keV. The rise and the fall time of the electron pulse from the gun are assumed to be linear. Their duration ranges between 10 and 50 ns. The power calculated for the gun and for the grid is based on the total charge of about 1300 µC. It takes into account the bunching efficiency and the collimation in order to get 750 µC at the injector exit. At 200 kV, the gun provides an energy of 253 J. With a repetition rate of 100 Hz, the beam power out of the gun is 25 kW. The average current delivered by the gun is 0.127 A. The duty cycle is 0.0092. It implies an average current of 13.8 A during the pulse. The gun is of the triode type. With the cathode at –200 kV, a pulsed grid allows this peak current. The grid limits the electron current (I_b) by space charge effects [3.2]. The grid voltage is plotted versus the beam current on Fig. 3.5 based on the LEP Injector Linac (LIL) gun characteristics. The CLIC grid voltage is estimated to be around 600 V.

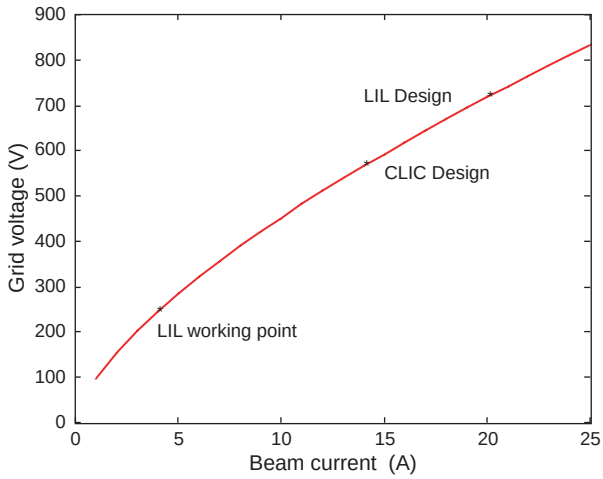

Fig. 3.5: *Grid voltage versus beam current.*

A pass tube is fed from a power supply and provides the –200 kV. A function generator drives the grid through optical fibres and the linear power amplifier must have the necessary bandwidth to reach the required grid modulation. A ripple of one per mil, during the 92 μs flat-top, could be obtained with the voltage. The beam emittance was measured out of the LIL gun [3.4]. The measured geometrical emittance containing 85% of the beam is 120 μm·rad (not normalized) for a beam current of 1 A.

The bunching system

The bunching system is composed of two subharmonic bunchers (SHB1 and SHB2) working at 937/2 MHz, followed by one standing-wave pre-buncher (B1) and one travelling-wave buncher (B2), both working at 937 MHz. The bunching efficiency is estimated at 66% (based on LIL) while the collimation efficiency (at 50 MeV) is estimated at 90%. After a drift of 50 cm from the gun exit, the first subharmonic buncher (SHB1) receives a modulation of ±10 kV. The second subharmonic buncher (SHB2) is 2 m downstream and works with a modulation of ±50 kV. The phase of the SHBs is rapidly switched by 180° every 130 ns, in order to produce the 'phase-coded' subpulses. Then the pre-buncher (B1) is 1.25 m downstream and works with a voltage of ±100 kV. Finally the buncher B2 continues the bunching process while accelerating the beam up to 10 MeV. It has 12 cells (4×3 cells) with a phase advance of $2\,\pi/3$. The magnetic field along the front end keeps the beam sizes to a reasonable value of 10 mm (90% of particles). The front end is roughly 5 m long.

The injector linac

The linac is composed of three damped and detuned accelerating structures (S1 to S3) and works in the fully loaded steady-state mode. It accelerates the beam up to 50 MeV with travelling wave sections at 937 MHz. A long sequence of solenoids along the entire section is installed for focusing. The accelerating structures are 3.4 m long with a loaded accelerating field of 3.9 MV/m. They are similar to those of the drive-beam accelerator. The injector linac provides an energy gain of 40 MeV. Adding the beam energy from the front end, the total energy at the injector linac exit is around 50 MeV. A beam collimation is implemented with losses up to 10% before injection of the beam into the accelerating linac.

The matching section and the spectrometer line

A matching section composed of two quadrupole triplets is implemented at the injector exit (50 MeV). A chicane will allow the beam collimation ($\pm\ 3\ \sigma_E$) in order to achieve the required beam characteristics. Losses up to 10% before injection of the beam into the drive-beam accelerator could be accepted. A spectrometer line will be used for beam diagnostics and beam performance optimization.

3.2.2 Beam characteristics required at injector exit

The main condition to be fulfilled is that the total number of bunches should be a multiple of 32 since there are two combiner rings giving a multiplication factor of 4 and a delay loop providing a multiplication factor of 2.

The energy spread at the exit of the injector linac is partly correlated due to the short-range wakefields. The uncorrelated energy spread is assumed to be 0.75% and the total energy spread is assumed to be less than 1%. Such a value is expected after beam collimation around $\pm 3\ \sigma_E$ before the injection in the accelerating linac. An r.m.s. value of 4 mm for the single bunch length could be achieved at the injector exit. A large beam size could cause losses in the decelerating structures. Therefore, it is crucial to obtain at 1.2 GeV a beam with an emittance as small as possible. Assuming an emittance blow-up of 50% between the injector and the decelerator, an upper limit of 100 μm·rad is required at 50 MeV. Table 3.2 summarizes the beam characteristics required at the injector exit.

Table 3.2: Beam characteristics required at the injector exit

Parameters	**Injector exit**
Beam energy	50 MeV
Pulse length (total train)	92 μs
Beam current per pulse	8.2 A
Charge per pulse	750 μC
Number of bunches per pulse	~43 000
Bunch length (FWHH)	32 ps
Bunch length (r.m.s.)	4 mm
Normalized emittance (r.m.s.)	≤ 100 μm·rad
Energy spread	< 1%
Repetition frequency	100 Hz

3.2.3 Beam dynamics simulations

Beam dynamics simulations are done with the PARMELA code [3.5]. Preliminary simulations have been performed for the bunching system (up to B2) and with an energy gain of 3 MeV. As initial beam conditions, a given number of particles (between 100 and 500) are generated randomly in a four-dimensional transverse hyperspace with uniform phase and random energy-spread at the gun exit. The normalized r.m.s. emittance is 10 μm·rad at this point and 100% of particles are assumed to be confined within six times this emittance. At 200 keV a total emittance of 62 μm·rad is used for the simulations. With a radius of 10 mm for the hole in the anode, the horizontal (and vertical) β-value of the ellipse is 1.61 m/rad. The r.m.s. beam radius is $\sigma = 7$ mm. A straight ellipse ($\alpha = 0$) is assumed in both transverse planes at the gun exit. The longitudinal coordinate $z = 0$ is taken at the anode exit where the magnetic field is still zero. The total charge of 29.2 nC (1.8×10^{11} e^-) is distributed over two RF periods of 937 MHz. The transverse focusing is provided by a longitudinal magnetic field satisfying the Brillouin-flow condition. Both axial bunch velocity and bunch current are functions of z. For preliminary simulations, the magnetic field is represented by a fast rise at the beginning, starting from zero and followed by a constant amplitude along the front end (≈5 m). Figure 3.6 shows the energy gain from the gun exit.

Figure 3.7 shows the horizontal beam envelopes along the front end. The continuous curve is the r.m.s. envelope and the dotted curves are the 90% and 100% beam envelopes. The entire beam remains inside the 40 mm aperture (radius) of the travelling-wave structures. The buncher's aperture (radius) is 53 mm. The core of the bunch has an extension of 22 degrees while the total bunch (a few particles in the tails) extends over twice this value. The full energy spread is roughly ±10% which corresponds to a r.m.s. value of a few per cent. Figure 3.8 shows the bunch length obtained at 3.7 MeV.

Figure 3.9 shows the initial phase versus the current phase. It provides a figure of merit of the bunching efficiency. For this run with 500 particles and an initial phase of ±500°, one obtains ±300° in the correct bucket. The bunching efficiency in this case is 60%.

The normalized emittance is 245 μm·rad. The results presented here are preliminary. The target values for the injector are not yet completely reached and further optimization is necessary. The input and resulting parameters are given in Table 3.3.

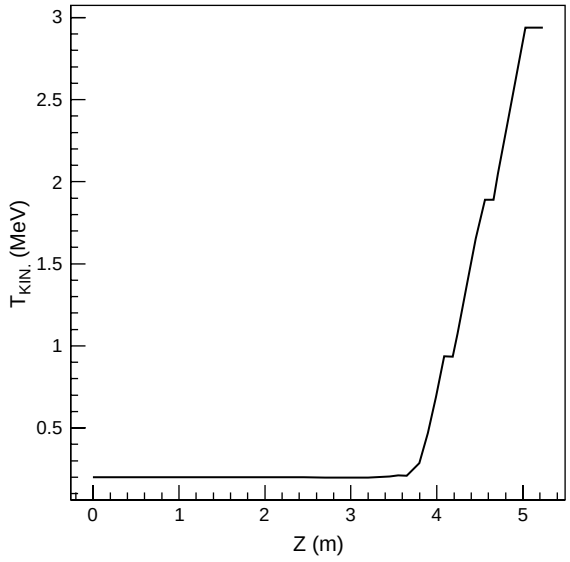

Fig. 3.6: *Energy gain along the front end.*

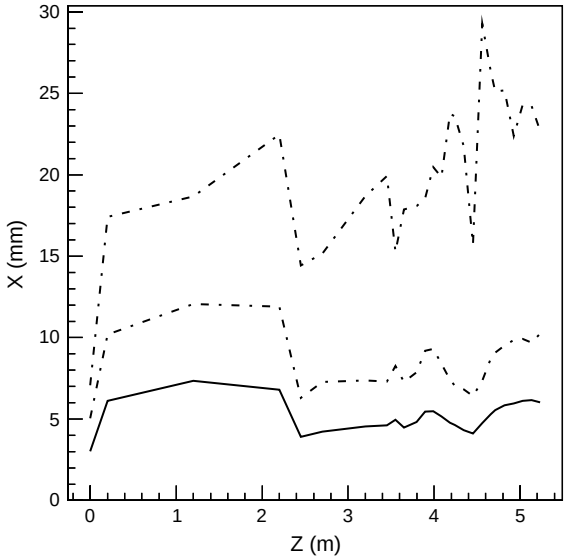

Fig. 3.7: *Horizontal beam envelopes (r.m.s., 90% and 100% of particles).*

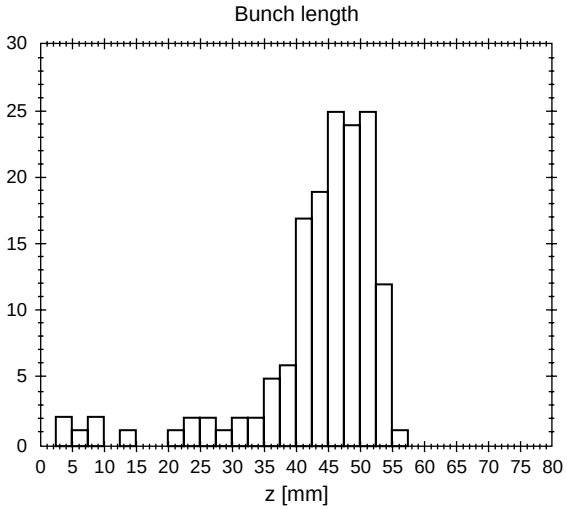

Fig. 3.8: *Bunch length at the front-end exit.*

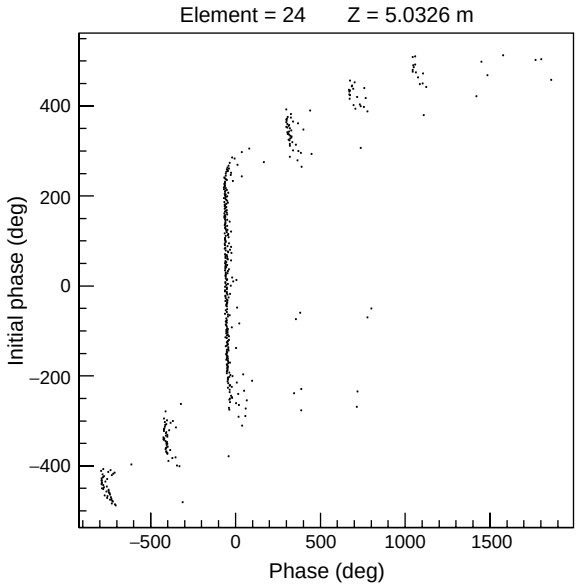

Fig. 3.9: *Bunching efficiency of the injector.*

Table 3.3: Preliminary simulation results at the front-end exit

PARMELA results	
Beam energy	3.2 MeV
Bunch charge/2 RF periods	30 nC
Bunch population/2 RF periods	18×10^{10}
Bunching efficiency	67%
Bunch length	19.5 mm (FWFM)
Phase extension (937 MHz)	22 degrees
Energy spread (single bunch)	20% (FWFM)
Normalized emittances	245 μm·rad

3.2.4 A photo-injector option

The possibility to use a RF photo-injector as the drive-beam source is under investigation. Figure 3.10 gives a sketch of a possible layout. A CW laser working at 468.5 MHz provides a continuous train. During 92 μs the necessary power at 262 nm is generated in order to create the charge of 750 μC by the photocathode. The 'even' and 'odd' photon pulses are directly produced by electro-optics components. The resulting laser beam illuminates the photocathode of an RF gun powered by a klystron at 937 MHz. It generates an electron beam with a momentum of several MeV at the exit of the photo-injector and with the required sequence of bunches which can then be directly injected into the drive-beam accelerating linac. Such an option would represent several advantages: it would replace the thermionic gun and the bunching system by a single RF gun; the pulse shaping would be much easier and could be adjusted in order to optimize the RF power generation; small emittances would be achievable. However, several issues remain to be addressed: the UV power and stability for the laser and the necessary charge for the photocathodes. An R&D programme has been set up to try to overcome these problems.

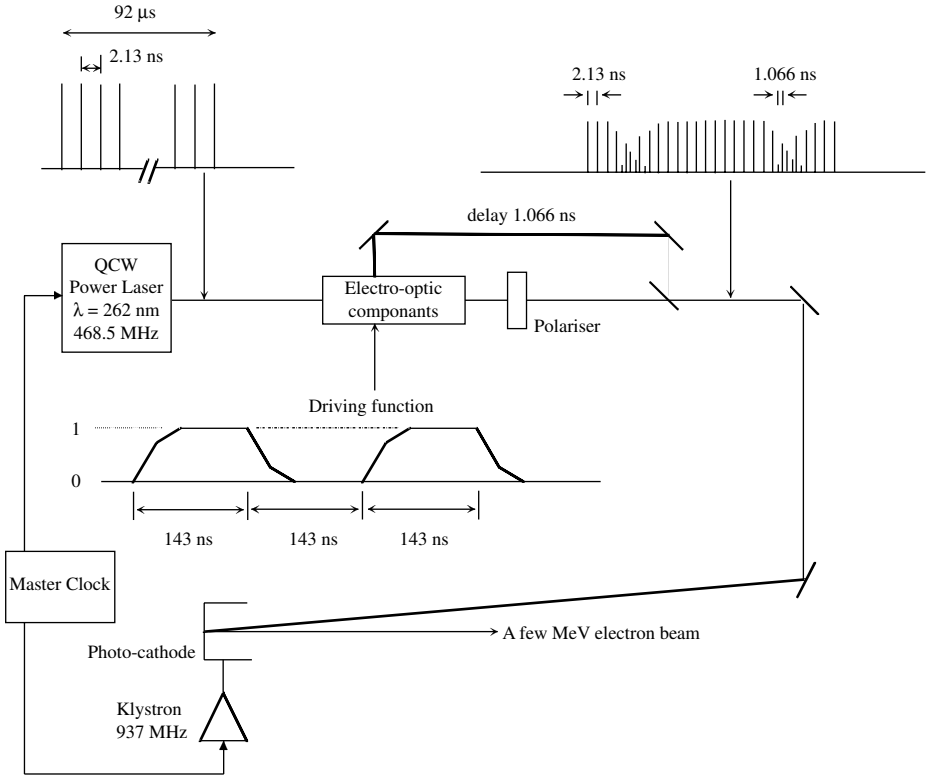

Fig. 3.10: *Possible layout for a photo-injector option.*

3.3 Drive-beam accelerating linac

3.3.1 The accelerator beam dynamics

The drive-beam accelerator consists of 50 FODO cells with a constant phase advance of 117 degrees. The spacing between quadrupoles is 3.8 m and one accelerating structure with a length of 3.1 m is placed between each pair. The beam is accelerated from 50 MeV to about 1.2 GeV. Every second bucket of the beam is filled with a charge of about 16 nC, switching from odd to even buckets or vice versa every 60 bunches.

For the simulation the single-bunch wakefields were derived from the ones calculated for SBLC [3.6] by scaling with the frequency and iris radius. The longitudinal multibunch wakefields were ignored, their effect should be small due to the beam loading compensation scheme. The transverse wakefields were calculated for a constant impedance structure for four different iris radii [3.7]. For each cell the loss factor and the frequency of the two most important dipole modes were derived by interpolation. An analysis that includes the coupling between cells and the damping remains to be done. Conservatively, a damping with $Q = 100$ was assumed for the first dipole mode and with $Q = 400$ for the second.

The initial bunch length in the accelerator is $\sigma_z = 4$ mm while in the decelerator it should be smaller than 0.4 mm. Therefore, bunch compression is needed. On the other hand, the bunch length has to be larger than 2 mm in the combiner rings and the following bends in order to suppress coherent synchrotron radiation. Thus a final

compression is needed at the point where the beam is bent into the decelerator. To evaluate the final bunch length a simple calculation was performed [3.8]. The compression stages are assumed to be linear. The longitudinal single-bunch wakefield was scaled from the one from SBLC assuming $W \propto 1/a^2$. Two different strategies of compression exist. One can compress the beam to $\sigma_z = 2$ mm at about $E = 100$ MeV and then just accelerate it. The final compression after the final bends then yields a bunch length of $\sigma_z = 290$ µm. It is also possible to compress the beam as much as possible at three stages in the linac. Before the rings the beam is uncompressed to $\sigma_z = 2$ mm. After the final bend it is compressed as much as possible yielding $\sigma_z = 170$ µm. The phase space for this case is shown in Fig. 3.11.

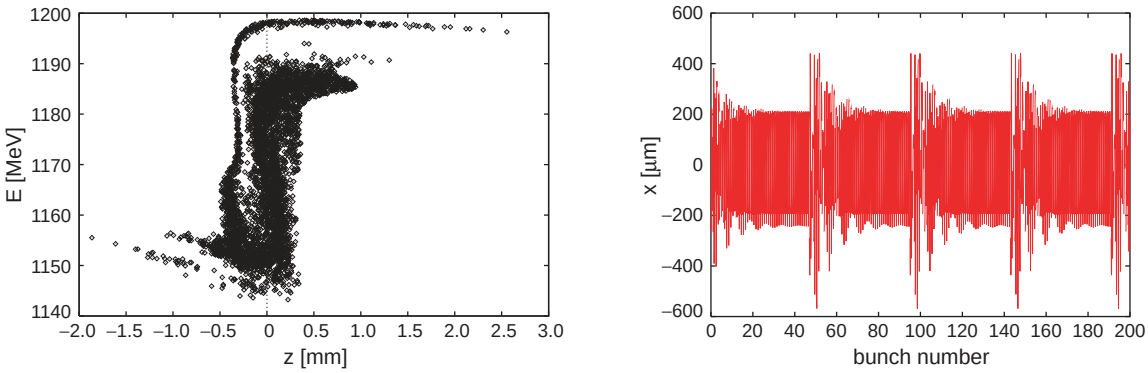

Fig. 3.11: *The longitudinal phase space in the case of four compression steps (left). The final position of the slices in a bunch train with an initial offset of one sigma (right). The periodic large deviations are the result of the phase switch.*

Coherent jitter of the beam is one of the possible sources of instability. Figure 3.11 shows the final offset of the different bunch slices at the exit of the accelerator for an initial offset of $\Delta = \sigma$. Large amplitudes occur periodically. At these positions one switches from one train to the next. The offsets reach a steady state before the next train. It is therefore not important to simulate the exact pattern of the switching with the precise length of the trains. However, the time necessary for switching is important, as can be seen in Fig. 3.12. Here, the amplification of an initial offset is shown for a fast switch without any ramp and one with a ramp of 20 bunches. The points represent different slices of the beam. Initial and final offset are normalized to the beam size. Without a ramp the maximum amplification is significantly larger than with a ramp. Even a short ramp results in a significant reduction of the amplification.

The initial misalignment of the accelerator components needs to be corrected with beam-based alignment. Only a simple one-to-one correction is used in the simulation, since this machine needs to be very simple to operate in order to minimize down-time. All components are assumed to be scattered around a straight line with a normal distribution with a sigma of 100 µm. For the quadrupoles larger errors are assumed, but they have no influence on the results.

Figure 3.12 shows the result of the correction in one case. The simple correction technique seems to be sufficient. This was verified by simulating 20 other cases [3.9] in which similar results were found.

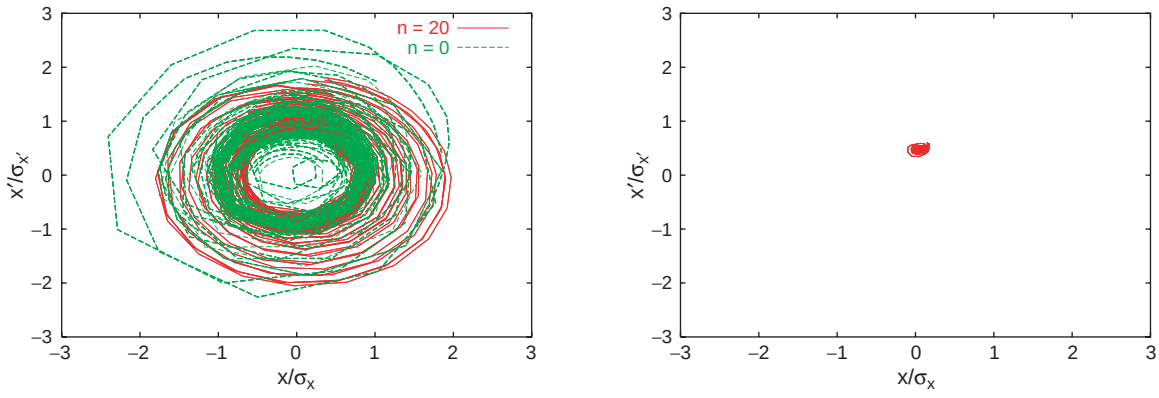

Fig. 3.12: *Left: The amplification of an initial jitter. Initial and final position are normalized to the beam size at the corresponding energy. Right: The final bunch positions for a corrected machine.*

3.3.2 Description of the accelerator cavities

3.3.2.1 Structure description and scaling

The group velocities and the R'/Q values must be such as to enable the beam to use up properly the electromagnetic energy before it reaches the structure end. Two possible designs of the accelerator cavities are being investigated. A new concept based on a slotted iris and constant aperture is proposed (E. Jensen et al., LINAC 2000). The model based on a classical geometry in order to avoid excessive surface gradients is described below.

First beam transport simulations with 937 MHz structures of 29 cells having an average iris radius a equal to 48.5 mm, an average outer radius b = 144 mm and a disc thickness d = 19 mm demonstrated that both detuning and damping were necessary to preserve a sufficiently low transverse beam emittance. The design is based on the same principles proposed for the CLIC main accelerating structures [2.23]. Good beam transmission was obtained with a dipole frequency spread of about 10% and a Q-value of 100 for the first mode and 400 for the second one (see Section 3.3.1 on beam dynamics). Since some scaled model work was planned at 3 GHz, the investigations with the code ABCI were all done for structures with this fundamental frequency (the average iris radius a scales to 15 mm at 3 GHz). A 29-cell structure having for the first cell a = 17 mm and for the last one a = 13.3 mm was used.

Table 3.4 lists the relevant parameters of the two extreme cells for zero bunch length and the 937 MHz operating frequency of the CLIC drive beam.

Table 3.4: Parameters of the first and last cell of the 937 MHz structure

Quantity	First cell	Last cell	Units
Iris radius a	54.4	42.6	mm
Relative group velocity v_g	0.053	0.025	–
Outer radius b	147.2	140	mm
R/Q for fundamental mode	1088	1340	Ω/m (linac)
Frequency of first transverse mode	1.22	1.34	GHz
Transverse loss factor k of first mode	32.34	63.5	V/pC/m^2
Frequency of second transverse mode	2.14	2.18	GHz
Transverse loss factor k of second mode	3.1	13.7	V/pC/m^2

A 32-cell damped, detuned scale-model has been realized for 3 GHz (Fig. 3.13). Damping was confirmed by computations on a single cell using the HFSS code yielding Q-values of 11 and 100 for the first and second transverse modes, respectively [3.10]. The model work and the HFSS calculations have demonstrated that sufficient damping for beam survival is obtainable.

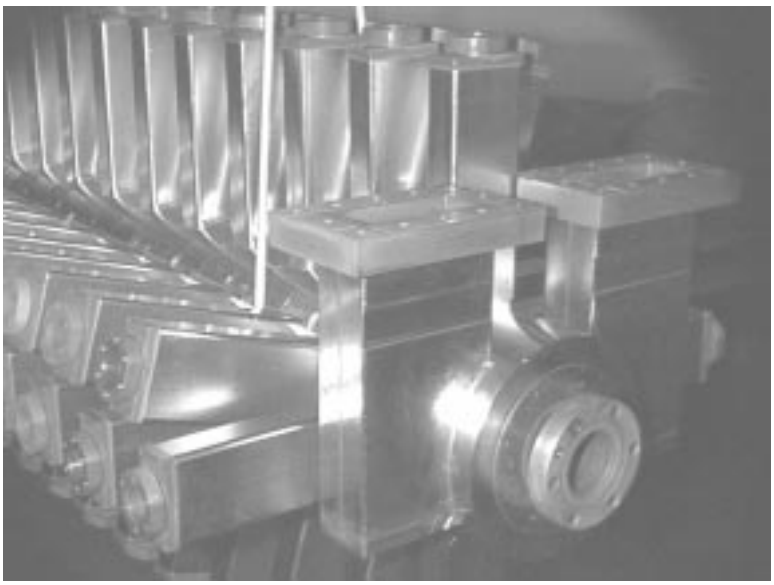

Fig. 3.13: *Front end of a 3 GHz scaled CLIC drive-beam acceleration structure with transverse damping waveguides against bipolar and quadrupolar high-order modes. Each such waveguide contains a SiC absorber.*

3.3.2.2 Wake-fields and the structure model

The short-range wakefields of the structures are derived by scaling from those for the S-Band Linear Collider (SBLC). For the SBLC frequency of 2.998 GHz the longitudinal delta-wakefield can be expressed as follows [3.6]:

$$W_{\mathrm{L}} = 250\ \mathrm{V/(pC\,m)} \exp\left(-0.85\sqrt{z/\mathrm{mm}}\right)$$

For fixed ratio a/λ, the scaling of the wakefield amplitudes with frequency goes with the frequency ratio to the square, i.e. $(f_1/f_0)^2$. For a change of a/λ, the scaling law is not straightforward, but goes with the square of the inverse of the radius-ratio, i.e. $(a_0/a_1)^2$. The long-range longitudinal wakefields are neglected in the simulations reported in Section 3.3.1. Their effect on the mean bunch energy should be taken out by the beam loading compensation, so that only the distribution might slightly change.

The transverse delta-wakefield for 2.998 GHz can be approximated by the following relation [3.6]:

$$W_{\perp} = 5.45\ \mathrm{kV}/(\mathrm{pC\,m^2})\left[1-\exp\left(-1.13\sqrt{z/\mathrm{mm}}\right)\left(1+1.13\sqrt{z/\mathrm{mm}}\right)\right] \quad .$$

Provided that a/λ remains constant, the scaling with the frequency is proportional to the cube of the frequency-ratio, i.e. $(f_1/f_0)^3$ as shown in Ref. [3.11]. For a variation of a/λ, the scaling of the amplitudes is approximately given by the following law $(a_0/a_1)^{2.2}$.

The ratio a/λ selected for the accelerator is larger than that for SBLC by a factor 1.25. The long-range transverse wakefield is calculated by assigning specific modes to the individual cells. It is assumed that the modes are trapped and do not propagate longitudinally. For each cell the two modes with the highest loss factors are used and the transverse field of the cell is given by the summation of these sinusoidal modes, exponentially decreasing with the distance z behind the particles driving the wakefield.

In order to obtain a realistic model at 937 MHz, the loss factors and frequencies for all the 29 cells are estimated by interpolating between the four cells simulated with the code ABCI at 3 GHz [3.12],[3.10]. The radii are equally spaced in the range 42.6–54.4 mm, corresponding to 13–17 mm at 3 GHz. Once the frequencies and amplitudes of the two most important modes in the four simulated cells have been calculated, the results are fitted by interpolation with a continuous function. These fits give closed expressions for the amplitudes and frequencies of the first two modes of the transverse wakefield which can then be used in beam tracking simulations (Section 3.3.1).

The damping was measured on a model indicating an upper limit for the damping of the first transverse mode of $Q < 100$ and a value of $Q \approx 400$ for the second mode. In what follows, a quality factor for the main mode $Q = 100$ is used but more precise measurements are expected to show significantly smaller values. Calculations predict $Q \approx 11$ for perfect loads [3.10].

3.3.3 Drive-beam power systems

3.3.3.1 Klystrons

The CLIC drive-beam RF power system provides 100 MW, 100 μs long pulses for each single accelerating structure of the 1.2 GeV, fully loaded and conventional 937 MHz, L-band linac [3.2]. A modular drive power system approach has been chosen, where the RF outputs from two 50 MW klystrons are connected to this single 3.4 m long, travelling wave structure, via 3 dB power combiners. Each of the 50 MW klystrons is driven by high-power modulators as shown below in Fig. 3.14. The CLIC scheme will contain in total about 90 of these RF power modules in each of the drive-beam linacs.

CLIC requires a high conversion efficiency of AC power into klystron RF output power in order to reduce overall power consumption. Multibeam klystrons (MBKs) are being designed for this task in the above drive scheme (Table 3.5). These can be likened to a number of separate klystrons that share common cavities, a common collector structure, and the axial magnetic focusing field. For a given peak output power (P_{o}) and efficiency (η_{MBK}) the MBK beam voltage reduces with an increasing number of beams (n_{b}) within the structure. This lower voltage reduces the probability of gun breakdowns with long pulse lengths and reduces any X-ray emission. It also permits the overall tube length to be reduced by up to 25%, leading to a smaller total volume for the installation. The MBK efficiency is expressed empirically as a function of the single-beam microperveance (μP) by:

$$\eta_{\mathrm{MBK}} = [0.78 - 0.16\ (\mu P)] \quad .$$

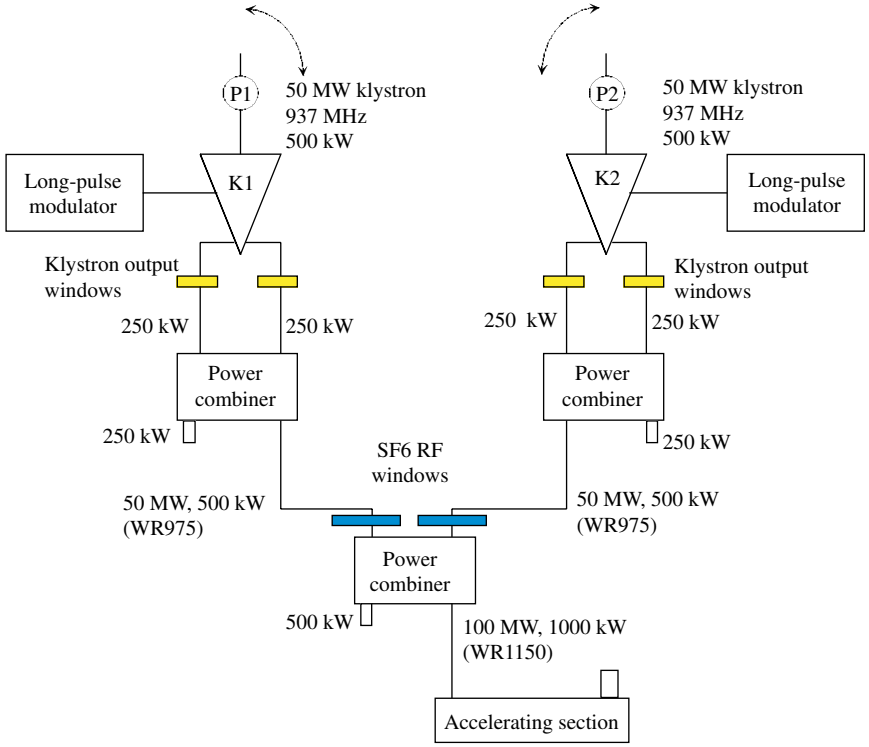

Fig. 3.14: *The 50 MW MBK RF network module.*

This low, single-beam microperveance, with low space-charge forces, enables stronger beam-bunching and so a higher electron efficiency compared to the standard monobeam, higher microperveance tube. An efficiency of 65–70% is calculated for the CLIC MBK. For high efficiency, as much of the kinetic energy as possible in the bunched beams must be converted into electrical energy at the RF output. This is achieved by decelerating the electron beam in the output gap. On account of the potential drop at the collector entrance, some electrons are accelerated in the reverse direction, particularly from the central, seventh beam, giving rise to oscillations and unwanted sidebands. An alternative six-beam MBK is also being investigated in case this difficulty has an impact on the use of the central beam and restricts the present design (Table 3.5). Each of the parallel beams is the MBK transport part of the total output power $\left(P_{\mathrm{o}}/n_{\mathrm{b}}\right)$ so that the effective tube microperveance is $n_{\mathrm{b}}(\mu P)$. The peak output power is then given by:

$$P_{\mathrm{o}} = \eta_{\mathrm{MBK}}(\mu P)\, n_{\mathrm{b}} \left(V_{\mathrm{k}}\right)^{5/2} \quad .$$

The simulated power transfer curves [3.13] for a seven-beam MBK are shown in Fig. 3.15.

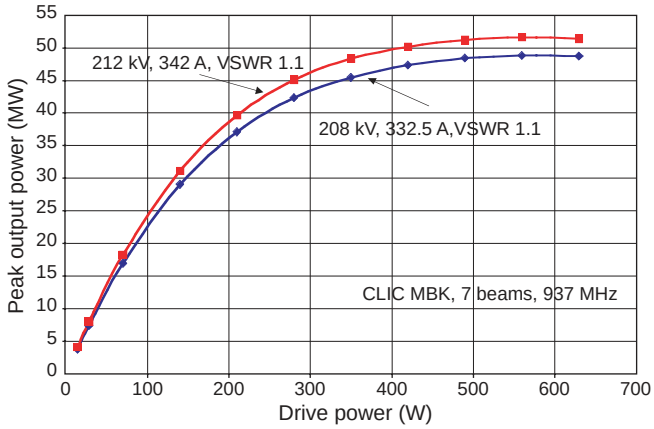

Fig. 3.15: *Simulated MBK power transfer curves.*

The present MBK design parameters are given in Table 3.5.

Table 3.5: Six- and seven-beam MBK design parameters

Parameter	
Frequency	937.5 MHz
RF pulse width	100 μs
Microperveance	0.5 A/V$^{3/2}$
Number of beams (n_b)	7 (6)
Beam area convergence	5.4:1
Beam interaction length	~2800 mm
J_{max}	6 A/cm^2
Efficiency	65–70%
Bandwidth (−1 dB)	4 MHz (min)
Saturated gain	≥47 dB
Focusing field	975 G
Beam voltage (V_k)	212 kV (211 kV)
Collector dissipation	Full beam
Beam current	342 A (293 A)
Peak RF output power (P_o)	47 MW (40 MW)

The choice of six beams is a minimum to meet initial design parameters and stay within current experience limits. An MBK with a seventh beam should enable a device to be developed that is close to the required RF power output specification. A further increase in the number of beams in the tube envelope will again reduce the beam voltage requirements and enable a higher peak output power to be obtained, but will not increase the efficiency, and increases the complexity of the gun and beam focusing systems.

For a greater number of beams ($n_b > 7$) a larger-diameter cavity would probably be needed, and could be operated as a higher-order mode multibeam klystron (HOM-MBK). However, larger cavities have multiple resonances that may bring difficulties in selecting the right operating mode for the klystron and cause a reduction in gain or efficiency. A larger-diameter cavity could make the internal geometry simpler with a beam convergence ratio closer to unity reducing the focusing power needed for the electromagnet and improving overall klystron-modulator system efficiency. All of the multibeam klystron scenarios discussed above require development to ensure that the operational parameters can be obtained.

3.3.3.2 Modulators

The conventional line-type modulator baseline design, shown in Fig. 3.16, has been studied [3.14] for powering a single 50 MW multibeam klystron and can also be used with two parallel, lower-power (25 MW) klystrons in an initial development phase. A key consideration is the conversion efficiency of AC wallplug power to pulsed RF power from the klystron. This requires that each major functional part be optimized for efficiency as well as for high-voltage performance and reliability. In this baseline design a high-efficiency switched-mode power unit is proposed for the high-voltage charging system. This is connected to a Rayleigh multicell (~33 cells) pulse-forming network (PFN), and discharged by two thyratron switches into the MBK load via a step-up pulse transformer. Auxiliary power systems provide the thyratron and klystron tube heating and focal power to an electromagnet for a magnetic field of around 2.5 times the Brillouin level. An overall AC-to-RF power efficiency of about 52% for a klystron modulator should be obtainable. The parameters for a 50 MW baseline modulator are shown below (Table 3.6).

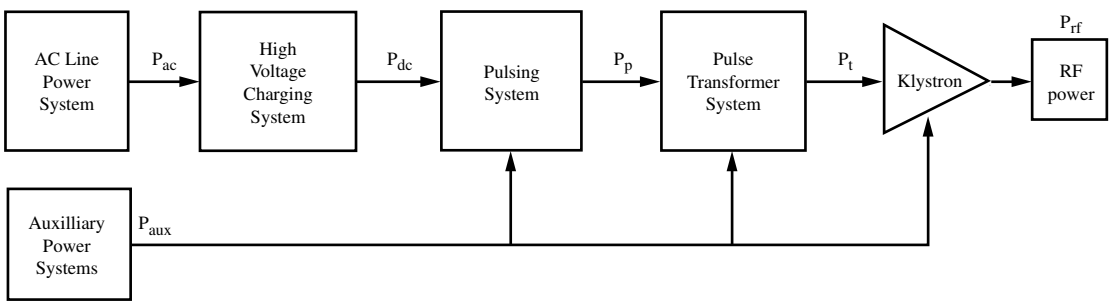

Fig. 3.16: *Block diagram of a basic modulator.*

Table 3.6: Baseline modulator parameters

Parameter	
Modulator pulse width (FWHM)	108 μs
Voltage pulse rise time (10–90%)	12 μs
PFN voltage (max.)	43 kV
Single PFN impedance	11.5 Ω
PFN cell capacitance	155 nF
Stored energy in PFN	8.5 kJ
Klystron-to-PFN mismatch (max.)	6%
Single thyratron peak current	1800 A
Single thyratron average current	19.5 A
Pulse transformer ratio	1:10
Pulse transformer volt-seconds	22.5 Vs

Different modulator designs using Insulated Gate Bipolar Transistors (IGBTs) for high-voltage switching are also being investigated as a possible future replacement for the thyratron in the baseline design. Large IGBT arrays can be used to handle the switched voltage and current requirements, and these need adequate protection to ensure correct load sharing. Alternatively, a high-frequency 3-phase switching supply, with low leakage inductance mains transformers, that is gated on and off by its primary circuit IGBTs will produce a high-voltage pulse directly for the klystron, or via a step-up pulse transformer. In the CLIC klystron-modulator application the requirements of high conversion efficiency, with high reliability and the handling of high-average switched power are important issues that need to be resolved.

3.4 Frequency multiplication and pulse compression

3.4.1 Design of the delay line and combiner rings

The main issue in the compression system (delay line plus combiner rings) is the preservation of the bunch quality during the combination process. In particular, the bunch length and longitudinal phase-space distribution must be preserved and the fluctuations in phase and transverse position between trains and between bunches minimized. The rings, the delay line and the transfer lines must therefore be isochronous. The final bunch length must be short in order to maximize the 30 GHz RF power production efficiency in the drive-beam decelerator. The aim is an r.m.s. bunch length of $\sigma_z = 0.4$ mm, for a 16 nC bunch-charge. High-charge, short bunches can radiate a considerable amount of Coherent Synchrotron Radiation (CSR), leading to both a significant average energy-loss and energy-spread within the bunch [3.15]. The emission is concentrated at low frequencies [$\nu \leq 1/(2\,\sigma)$], and can be partly suppressed if at least a fraction of the emitted spectrum is below the cut-off of the beam pipe (shielding effect), though a lower limit in the beam pipe dimensions is imposed by the necessary beam clearance. Both the energy loss and spread must be kept small, in particular because the bunches belonging to different trains make a different number of turns in the rings (from 1/2 to 7/2) and will develop different energy distributions. This will cause relative phase errors between bunches and some bunch lengthening. These intense and short bunches will also interact with any small discontinuity of the beam chamber (e.g., bellows and septa), possibly being subject to longitudinal and transverse wakefields. It is therefore highly desirable to have relatively long bunches to manipulate in the compression system, and to compress them just before the injection into the drive-beam decelerator sections. An upper limit to the bunch length is given by the non-uniform kick experienced by the bunches at injection in the RF deflectors, due to their phase extension, causing growth of the single-bunch emittance. The bunch length has been fixed at the exit of the accelerator to be 2 mm r.m.s. approximately. The emittance growth in this case is approximately 2% (for an initial r.m.s. normalized emittance of 200 μm·rad), arising mainly in the deflectors (3.75 GHz) of the second combiner ring, where their effect is large. A correlated energy spread (~1% r.m.s.), suitable for the final bunch compression, is obtained in the accelerator by the combined effect of the RF curvature and longitudinal wakefields. The need to preserve the correlation all along the compression system means that all the distortions of the longitudinal phase space must be kept small. In particular, attention must be given to the higher orders of the momentum compaction. A numerical analysis has shown that second-order effects would be unacceptable and must be corrected by using sextupoles [3.2].

Another concern is the beam loading in the RF deflectors, particularly just before the extraction from the second combiner ring, where the average current in the train and the deflector's frequency (3.75 GHz) are the highest. In order to overcome this problem, a travelling-wave iris-loaded structure with a short filling time with respect to the train duration has been chosen. A steady-state condition is then reached with minimum transient effects, although at the expense of a loss in the deflection efficiency. The extraction system for both rings is also a critical item, the two main issues being the high repetition rate (particularly in the first ring –250 kHz) and the interaction with the high-current beam (particularly in the second ring –262 A). A possible solution is based on the use of pairs of travelling TEM wave transmission-lines [3.16].

A preliminary design of the lattices for the delay line and the combiner rings was made in 1999 [3.2]. Since then, the CLIC RF pulse length has been reduced from 143 ns to 130 ns. Such a parameter change implies a reduction of the delay introduced in the delay-line and of the circumference of the combiner rings. The existing lattice design could in principle be modified to fit the new parameters. Another possibility would be to use an alternative design for the isochronous cells [3.17], presently under investigation for CTF3. Such a design is based on the use of three bending magnets per module or cell instead of four. Being more compact, it would be better adapted to shorter rings and transfer lines. In the following, only the first-order design with the old parameters will be described in some detail. Tables 3.7 and 3.8 present the main parameters of the subsystems with the delay length and ring circumferences selected at the time of the study. The delay-line geometry has been chosen to minimize both CSR emission and overall dimensions. One 3-bend magnetic chicane is located in the delay line and two in each ring. They are used for fine path-length tuning (±0.5 mm tuning range), in order to adjust the relative phase of the bunches and compensate for orbit variations. Each chicane is 3.5 m long and works around an average bending angle of $\theta_0 \sim 150$ mrad. The tuning range is obtained with a bending angle variation of $\Delta\theta = 1.5$ mrad; such a small value of $\Delta\theta/\theta_0$ does not perturb the optics. Each chicane has a linear transfer matrix element $R_{56} = 0.065$. Both the delay line and the ring arcs are based on the same type of isochronous lattice cell (see Fig. 3.17), a modified four-cell FODO structure with 'missing magnets' [3.18]. The small finite R_{56} generated by the chicane is compensated in the two adjacent cells with $R_{56} = 0.065/2$, slightly detuned away from their isochronous point. In order to avoid distortions in the longitudinal phase space, all the arcs are made isochronous up to second order by the use of sextupoles placed in the high-dispersion regions where there are no dipoles. The use of different families of sextupoles makes it possible to correct the third order as well. These designs will have to be re-adjusted to the new nominal delay length of 39 m and ring circumferences of 78 m and 312 m (Fig. A.1).

Table 3.7: Delay line parameters

Delay length	43 m
Bending radius	3 m
No. dipoles	16
Dipole length	2 m
Dipole field	1.25 T

Table 3.8: Ring parameters

		Ring 1	**Ring 2**
Circumference	(m)	86	344
Bending radius	(m)	3.6	17.8
No. cells		4	20
Cell length	(m)	13.6	13.6
No. dipoles		16	80
Dipole length	(m)	1.4	1.4
Dipole field	(T)	1.1	0.22
No. quadrupoles		52	184
Quadrupole length	(m)	0.3	0.3
Max. quadrupole gradient	(T/m)	14	14
No. sextupoles		20	84
Sextupole length	(m)	0.3	0.3
Max. sextupole gradient	(T/m^2)	26	120
Max. β-function (h,v)	(m)	10.3, 10.9	32.6, 16.8

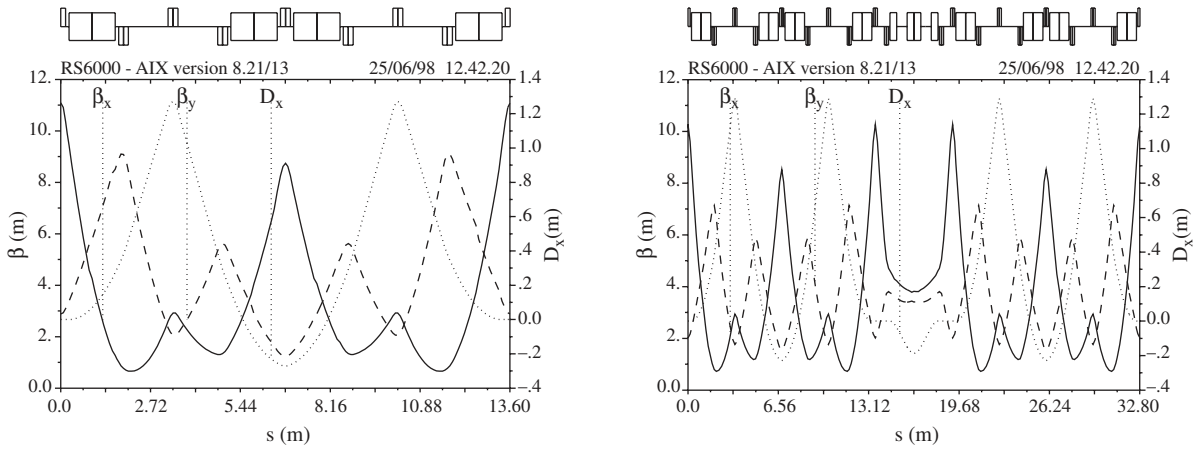

Fig. 3.17: *Lattices of the basic isochronous cell (left), and of the first ring arc (2 cells + 1 chicane), globally isochronous to 1st order (right). The β-functions and the dispersion curve are shown.*

The ring injection is similar to a conventional fast injection scheme based on a septum and a fast kicker, where the kicker is, however, replaced by an RF deflector. Another deflector is placed upstream of the septum (at $-\pi$ phase advance), and provides the pre-compensation of the kick given by the injection deflector to the circulating bunches. A $\pi/2$ phase advance FODO lattice is used in the injection straight section, with the septum and deflectors close to the focusing quadrupoles, such that the angular kick from the deflector corresponds to a maximum displacement in the septum (see Fig. 3.18).

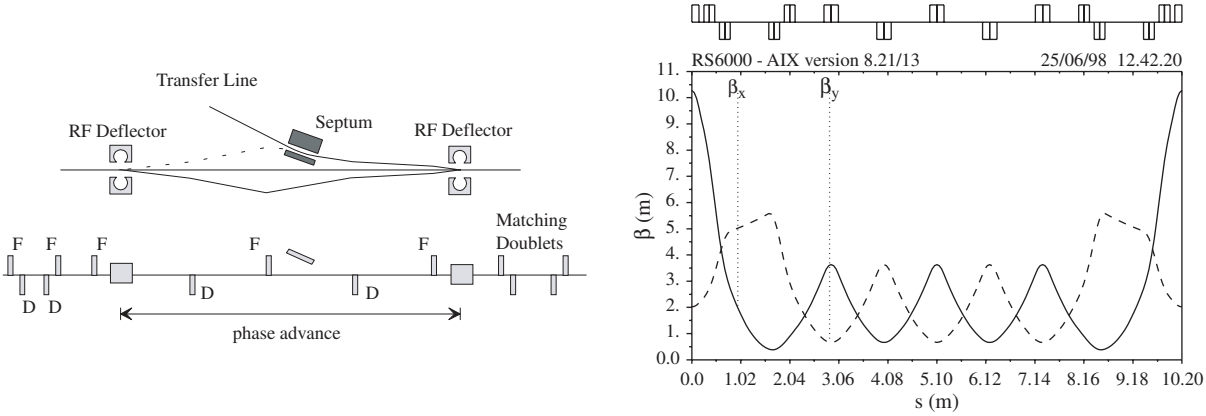

Fig. 3.18: *Injection-insertion layout with the RF deflector (left) and first-ring lattice (right). Circulating bunches will travel on the central or inner orbit, while the injected bunches are kicked by the 2nd deflector onto the equilibrium orbit. The train of combined bunches is ejected before the next pulse reaches the deflecting phase represented by the dotted line trajectory (intercepting the septum).*

All the RF deflectors are short travelling-wave iris-loaded structures, in which the resonant mode is a deflecting hybrid mode with a $2\pi/3$ phase advance per cell and a negative group velocity [3.19]. The design is basically the same for all the deflectors, with the cell dimensions linearly scaled with frequency. They are made of 4 cells at 937 MHz and 10 cells at 3.75 GHz, and provide the 2 mrad deflection needed in both rings, with a 50 MW and 15 MW power consumption, respectively.

The extraction kickers consist of pairs of TEM travelling-wave transmission-lines (Fig. 3.19) [3.16], powered in anti-phase, with the wave moving against the beam; the kicker length is chosen to be 2 m, with a half-aperture of 1.5 cm. A deflection of 3 mrad requires a voltage of 11.3 kV, corresponding to 2.6 MW into each 50 Ω line. The kicker filling time of 6 ns remains small compared with the 130 ns available rise time. Because of the length of the extraction kicker, a different design is used for the extraction region lattice, based on a triplet placed between the kicker and the extraction septum. The phase advance between the kicker and the septum remains ~$\pi/2$. The use of a triplet allows a rather constant β-amplitude along the kicker.

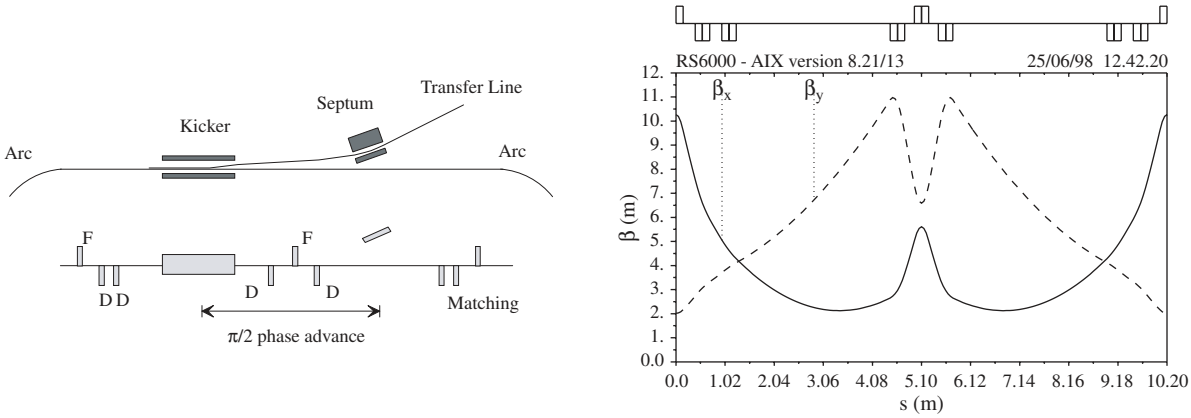

Fig. 3.19: *Extraction-insertion layout (left) and lattice (first-ring case, right).*

As mentioned earlier, the preservation of the longitudinal phase-space of the bunches is important in order to be able to compress them before injection in the drive-beam decelerator. The main sources of phase-space distortion in the pulse compression chain are the coherent synchrotron radiation (CSR) emission and the higher-order momentum compaction. The evaluation of the longitudinal bunch-dynamics in both rings takes into account the CSR effect with shielding and the isochronicity curves in the arcs after sextupole correction up to second order [3.2]. The results are promising; the final bunch-length after compression is smaller than the target value, with small bunch-to-bunch variation (from 340 to 360 μm r.m.s., depending on the number of turns in the rings). The contribution of the delay-line arcs, as well as the non-linear contributions from the return loops and the final bunch-compressor, have been neglected for the moment. Nevertheless, these contributions are smaller, and further improvement can be obtained, e.g., either by using different sextupole families, or by adding pulse stretchers and compressors in front of each ring and optimizing the bunch length in each component.

3.4.2 Transfer lines, compressors, path-length chicanes and loops

The drive-beam accelerator and the combiner rings are planned to be in a central position with respect to the two main linacs of the collider. This means that all the drive beams have to be first transported in a direction opposite to that of the main beams, before being turned around over 360° and injected in the different decelerating units where they travel parallel to the main beams.

The transport line for the beam going upstream is of course located in the same tunnel as the decelerators, near the tunnel roof in order to minimize the loss of space (cf. Fig. 1.2). This position offers the advantage of preventing interference with the main linac and the decelerator by keeping the turn-around loops at a different level both in the tunnel and in the individual alcoves which will house these loops.

The different beam-transport elements of the turn-around area [3.2] are schematically shown in the plan view of Fig. 3.20 (bottom part). The up-going drive beam arrives from the left through a simple FODO transfer line. After a small vertical deflection [see the solid line branching above the dashed line at the top of the drawing (Fig. 3.20), (side view)], the selected drive-beam pulse enters the 360° loop, consisting of a 90° right-turn followed by three 90° left-turns. Drifts between these 90° turns are added to adjust the geometry and separate the axis of the down-going beam from the up-going one. These modules are designed to be isochronous ($R_{56} = 0$) in order to preserve the bunch length and are based on the design concept elaborated for such applications with compact lattice and acceptable synchrotron radiation effects [2.9]. Table 3.9 summarizes the main parameters.

Table 3.9: Isochronous module parameters

Bending magnet length	1.6 m
Bending magnet fields	1.0/1.8 T
Bending angle per dipole	23.5/43 degrees
Bending radius	3.9/2.15 m
Quadrupole length	0.3 m
Quadrupole gradient	26.0 T/m
Module length	11.0 m
Transfer matrix coefficient R_{56}	0.00 m

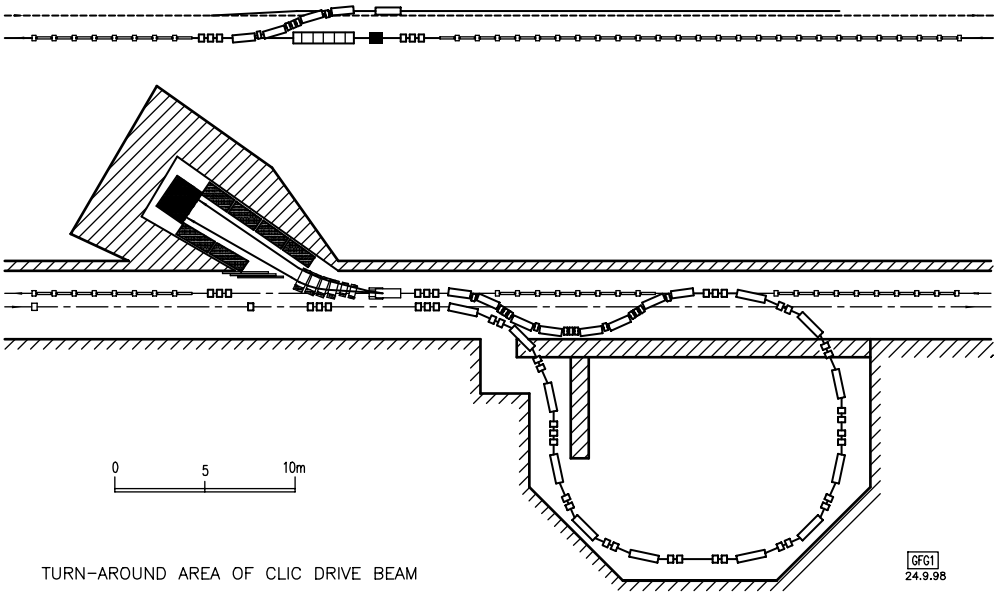

Fig. 3.20: *Layout of the turn-around area.*

After the loop, the beam traverses a sort of bending chicane that serves to adjust the path length and at the same time to compress the bunch length. The present proposal is a generalized chicane consisting of a series of four double-bends with two dipoles deflecting the beam in the same direction, i.e., with a bending radius ρ and a bending angle θ of the same sign. In this case, the integral of D/ρ over the two dipoles is positive by definition. The dispersion D, assumed to be zero, together with D', at both the entrance and the exit of the double-bend, is simply controlled by putting a focusing quadrupole at the mid-point between the two dipoles. The quadrupole inverts the sign of D' and the function D is mirror-symmetric with respect to this point. The correlation between the energy spread and the position z within the bunch requires a positive R_{56} for bunch compression. The total compression corresponds to a reduction of the bunch length from 2 mm to 290–170 μm with a correlated r.m.s. momentum-spread of approximately 1.5–1.2%. This gives a total R_{56} of ~0.15 m. On the other hand, the R_{56} coefficient must be sufficiently large for an adjustment Δl between ±2 mm and ±5 mm at most (i.e., half the RF period at 30 GHz). The proposed path-length module has an R_{56} equal to 0.13 m, the remaining compression being provided by the following vertical-bend (see side view of Fig. 3.20). In order to reach such a high value of R_{56} without increasing too much the angle or the dipole length, it is necessary to have a succession of four double-bends arranged in a geometry that looks like a chicane (Fig. 3.21). The total contribution to R_{56} is simply equal to the sum of the individual contributions. These do not depend on the sign of the deflection, since the double bends are separated by dispersion-free drifts. It is important to note that a triplet of quadrupoles must be inserted in the middle of these drifts. This matching triplet has no influence on R_{56} but is necessary to focus the beam and match the optics of the two adjacent double-bends. The following parameters of the generalized chicane were selected to give $R_{56} = 0.13$ m and $\Delta l = 0.5$ mm/mrad:

$$\theta_B = 16^\circ \quad l_B = 1.23 \text{ m} \quad B = 0.88 \text{ T} \quad l_{drift} = 0.5 \text{ m} \quad l_Q = 0.2 \text{ m} \quad G_Q = 20 \text{ T/m} \ .$$

A path-length adjustment of 2 mm implies a change in the bending angle by 4 mrad, which induces in the mid-point of the snake a still tolerable lateral shift by approximately 4.8 cm.

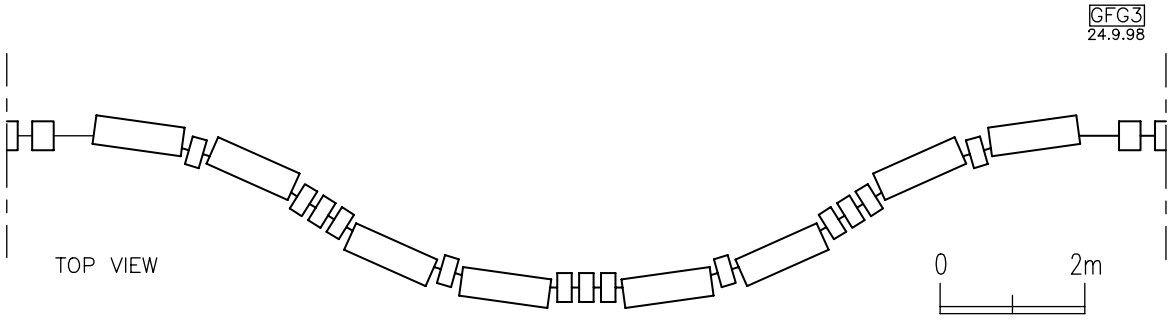

Fig. 3.21: *Layout of the path length module.*

The vertical translation which adds some bunch compression can be obtained by using the same double-bend concept. The coefficient R_{56} should be equal to 0.03 m in order to give a total of 0.16 m together with the path length module. Using the exact geometry, the following set of parameters for the elements of the two double-bends is proposed:

$$l_B = 1.23 \text{ m} \quad \theta_B = 11° \quad B = 0.60 \text{ T} \quad l_{drift} = 0.5 \text{ m} \quad l_Q = 0.2 \text{ m} \quad G_Q = 38 \text{ T/m} \ .$$

The drift in the middle of the module, containing a matching quadrupole triplet, has a total length equal to 1.0 m, adjusted such as to satisfy the translation amplitude required.

Another promising design consists in using the tunable achromats developed for the CTF3 project [3.20]. Its main advantages are its geometrical flexibility, its capability of easily adjusting the coefficient R_{56}, and its much smaller number of magnetic elements.

3.5 Drive-beam decelerator

3.5.1 Lattice and beam stability

The decelerator has to provide the RF power to accelerate the main beam by decelerating the drive beam. To achieve high efficiency, it is necessary that the final drive-beam energy be much smaller than the initial one. As a goal, the lowest-energy particles should have only 10% of the initial beam energy when the beam is dumped. Since the particles in the first bunches are not decelerated significantly, the final energy spread in the beam will be very large, see Fig. 3.22. Transporting this beam, which in addition has a very high current of about 240 A, is thus a challenge.

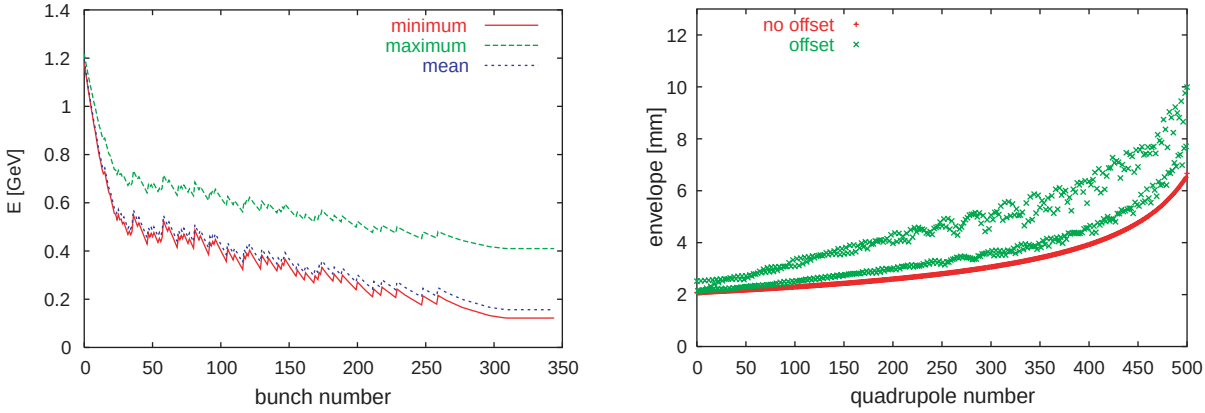

Fig. 3.22: *Left-hand side: The final energy spread of the beam. Right-hand side: The envelope of a four-sigma beam (in both planes) with and without an initial offset of sigma in the vertical plane.*

The beam line consists of a simple FODO lattice with a quadrupole spacing of 1.115 m. One decelerator structure with an active length of 0.8 m is placed between each pair of quadrupoles. A BPM is positioned in front of each quadrupole. The strengths of the quadrupoles are adjusted to keep the phase advance constant for the particles that lose most energy. Owing to the adiabatic energy changes, the particles at higher energies remain at smaller amplitudes [3.21]. It was found that the radius of the structure should be as large as possible in order to improve stability [3.22]. The drive-beam injector can provide a maximum current of about 250 A; together with the required output power this limits the radius to a maximum of about $a = 13$ mm, which was adopted for the structure.

The beam consists of about 1950 bunches separated by 2 cm and each with a charge of roughly 16 nC. To compensate the beam-loading in the main linac, it is necessary to ramp the RF power. This is achieved by delayed switching, therefore some bunches are missing in the first 20 ns of the pulse. The precise pattern will be adjusted for optimum compensation at the real machine and may vary from decelerator to decelerator.

The transverse stability of the beam is of concern due to its very high current. Two programs, WAKE [3.23] and PLACET [3.24], have been developed to simulate it. The PETSs have one dominating transverse and one dominating longitudinal mode. Because of the high group velocity, the power in both modes quickly drains out of the structure. In addition, the transverse mode is damped. In the simulations, particles pass the structure in several steps taking into account the longitudinal field distribution. In the following, the four-waveguide structure is used throughout, the six-waveguide structure is expected to give better results but the simulations of the structure are not

yet finalized (see descriptions of these structures in Section 3.5.2). The group velocity for each of the modes is $\beta = 0.441\ c$, the $R/Q = 41\ \Omega/\mathrm{m}$ (linac convention), the peak transverse wakefield $W = 225\ \mathrm{V/pC/m^2}$ and the damping of the transverse mode about $Q = 200$. This last value is significantly worse than the one assumed in previous simulations [3.25].

The envelope of a four-sigma beam is shown in Fig. 3.22 for an on-axis beam and one that has a very large initial offset of one sigma. The beam passes through the decelerator without problem. Here, a constant pulse current is assumed.

The transverse and longitudinal modes have very similar frequencies. The transverse wakefield produced by a leading bunch is thus minimal at a following one because of the phase difference of $\pi/2$ between the two modes. However, a small difference between the two frequencies leads to large effects.

Figure 3.23 shows the maximum amplification of an initial offset. At least a factor $\sqrt{10}$ is expected from the adiabatic undamping of the oscillation. The factor depends strongly on the transverse frequency, with a minimum at the fundamental. The asymmetry around this point is mainly an effect of the bunch length as simulations with point-like bunches show [3.9]. One can conclude that it is very important that the transverse frequency is tuned to the fundamental, and if it is different it should rather be higher.

Since the structure is not cylindrically symmetric, the deceleration of the particles depends on the transverse position. This non-uniformity of the longitudinal field also gives rise to a transverse kick. For an m-waveguide structure the transverse field can be expressed as

$$\vec{E}_\mathrm{t}(r,\phi) = \sum_\mathrm{i} 2k_\mathrm{i} mi \frac{r^{mi-1}}{a^{mi}} \frac{\lambda}{2\pi} \sin(2\pi s/\lambda)[-\vec{e}_\mathrm{r}\cos(mi\phi) + \vec{e}_\phi \sin(mi\phi)] \quad .$$

Here, r is the distance of the particle from the structure axis and ϕ the azimuth angle. The most important contribution is expected from the term with the lowest order in r.

A simulation with a four-sigma beam (and a normalized emittance of 150 µm·rad) with an initial offset of one sigma shows that the beam will be lost before the end of the decelerator, see Fig. 3.23. The problem can be solved by rotating every other structure by 45 degrees to cancel the effects in lowest order. The second order is also included in PLACET but does not show a significant effect.

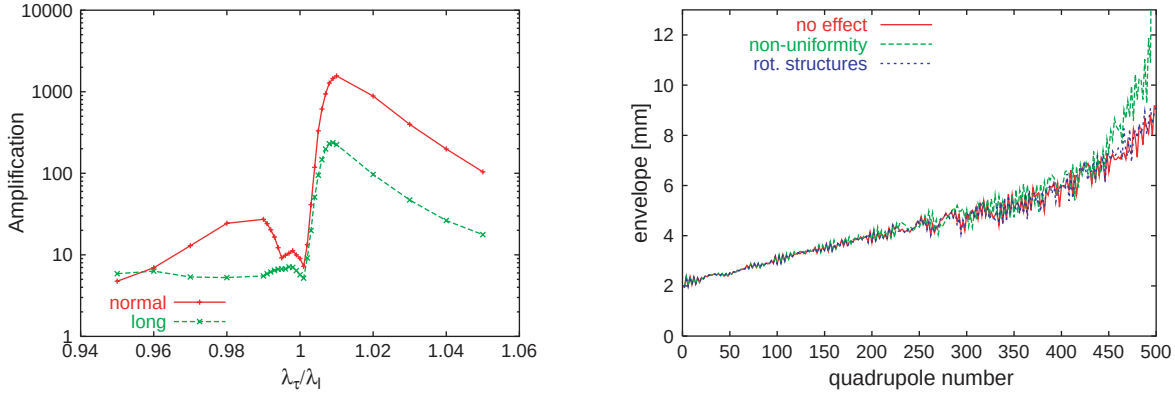

Fig. 3.23: *Left-hand side: The dependence of the maximum amplification of an initial jitter on the frequency of the transverse mode. Right-hand side: The effect of the non-uniformity of the longitudinal field in the four-waveguide structure.*

The drive-beam decelerator needs beam-based alignment. As a goal, an initial position error of the beam line components of 100 µm should be tolerable. The BPMs and quadrupoles are aligned with a low-intensity beam using the ballistic alignment method [3.22]. During this procedure, the beam is not focused over a distance of about 26 m corresponding to 23 quadrupoles that are switched off. To keep the envelope reasonably small, the beam emittance has therefore to be small. It is envisaged to use the main beam after the damping ring at an energy of $E = 1.98$ GeV. This beam has all the necessary properties. After the ballistic correction the quadrupoles are re-aligned with a simple one-to-one correction using the drive beam. The envelopes obtained by this procedure are shown in Fig. 3.24 for 10 different machines. The results are not satisfactory. Possible remedies are an increase in the final energy compromising the efficiency, an improvement in the correction algorithm, an improvement in the structure, and an increase of the decelerator length but with proportional increase of the initial and final energies. It is evident from the

figure that increasing the final energy helps. The correction algorithm can be improved in several ways, e.g., one can make use of the different energies in the pulse ramp to obtain a dispersion-free steering. A structure with six waveguides looks more promising than the one with four, but the calculations are not yet finalized. Increasing the length of the decelerator makes the beam more stable. The initial and final energies are increased to keep the efficiency the same. The 10 cases simulated for a decelerator twice as long as the present one show that the beams are stable in all cases.

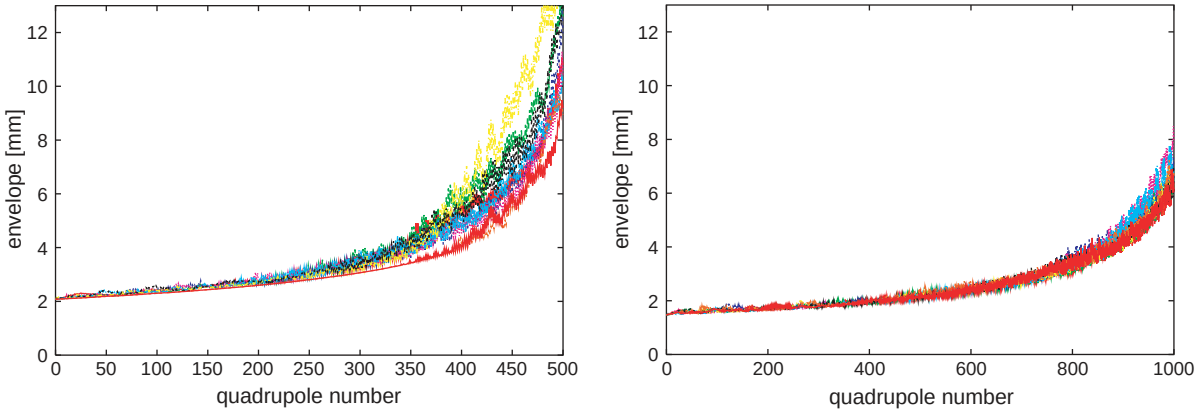

Fig. 3.24: *The four-sigma envelope of the beams in ten different decelerators after beam-based alignment. On the left-hand side for the nominal decelerator length, on the right-hand side for decelerators that are twice as long.*

3.5.2 The Power Extraction and Transfer Structure

3.5.2.1 Definition and function of the PETS

The Power Extraction and Transfer Structure (PETS) [3.26] is a passive microwave device in which the bunches of the drive beam interact with the impedance of periodically loaded waveguides and excite preferentially the synchronous hybrid TM mode at 30 GHz. In the process, the beam kinetic energy is converted into electromagnetic energy at the mode frequency, which travels along the structure with the mode group velocity. The microwave power produced is collected at the downstream end of the structure by means of couplers and conveyed to the main linac accelerating structures by means of rectangular waveguides [3.27]. In its classic configuration, the PETS consists of a cylindrical beam chamber, which is coupled by longitudinal slits to four teeth-loaded waveguides as visible in Fig. 3.25, which shows the PETS model with beam chamber diameter 26 mm.

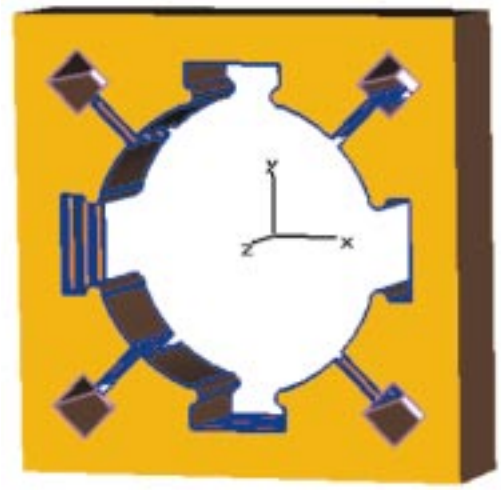

Fig. 3.25: *Four-waveguide PETS.*

3.5.2.2 Principle of operation

When a train of short electron bunches each of charge q_b traverses a section of PETS l_s metres long, it builds up a voltage across the structure of peak value

$$U_{\mathrm{f}} = \frac{\omega}{4}\left(\frac{R'}{Q}\right) l_{\mathrm{s}} q_{\mathrm{f}} \quad , \tag{3.1}$$

where $\omega = 2\pi f$ is the excited mode frequency, R'/Q is the normalized longitudinal impedance per unit length (expressed in linac Ω/m) of the structure at frequency f, q_{f} is the total beam charge in one fill time T_{f} of the structure and l_{s} is the structure length.

The fill time is simply the time it takes for the energy deposited by one bunch in the fundamental mode to travel through the structure:

$$T_{\mathrm{f}} = \frac{l_{\mathrm{s}}}{c}\frac{1}{\beta_{\mathrm{g}}} \quad \text{where} \quad \beta_{\mathrm{g}} = \frac{v_{\mathrm{g}}}{c} \quad \text{is the normalized group velocity.}$$

In order for the mode excitation to be coherent and therefore constructive, the bunch spacing must be a multiple of the mode wavelength which is 10 mm and the mode phase velocity must be equal to the speed of the relativistic bunches. The bunch time separation T_{b}, however, must be much shorter than one fill time T_{f}, so that several bunches contribute to the build up of the voltage U_{f}. The rate of energy deposition by the beam or the RF power generated in the PETS is obtained by multiplying the voltage U_{f} by the average beam current in one filling time $q_{\mathrm{f}}/T_{\mathrm{f}}$:

$$P = \frac{\omega}{4}\left(\frac{R'}{Q}\right)\frac{{q_{\mathrm{f}}}^2}{T_{\mathrm{f}}} l_{\mathrm{s}} F^2(\sigma) \quad . \tag{3.2}$$

The power form factor $F^2(\sigma)$ takes into account the finite length of the Gaussian bunches. For a train of bunches lasting much longer than the structure filling time, the peak power level in Eq. (3.2) stays constant provided that the charge per filling time remains constant. Expression (3.2) therefore gives the steady-state power level at the structure output when the internal wall losses are neglected.

3.5.2.3 The four-waveguide PETS

Structure parameters

Table 3.10 shows the main geometric and RF parameters of the transfer structure with a 26 mm beam chamber aperture which has been adopted as power extracting structure for the drive-beam decelerator [3.28].

Table 3.10: Parameters of the four-waveguide PETS

Beam chamber diameter	26.00 mm
Waveguide width	8.60 mm
Waveguide height	4.00 mm
Slit aperture	7.00 mm
Synch. mode frequency	29.985 GHz
Synch. mode β_{g}	0.441 c
Synch. mode R'/Q	41.0 linac Ω/m
Peak transverse wakefield	0.22 V/pC/mm/m
Transverse mode Q-value	140
Effective structure length	0.80 m
Nominal output power*	530.4 MW

* *The output power is computed for a train of bunches spaced by 20 mm, with charge 16.0 nC and σ = 0.4 mm, which gives a form factor of 0.94.*

Transverse wakefields in the PETS

The transverse wake induced in a 24-cell PETS section by a Gaussian bunch with σ = 0.4 mm and charge 1 pC displaced 1 mm off-centre has a peak value of 0.22 V/pC/mm/m. The wake spectrum shows almost no higher-order modes. It is therefore justified to assume that practically all the transverse deflection of an off-centre beam is caused

by the main deflecting mode, the frequency of which is only a few tens of MHz away from the main longitudinal mode. The value of the peak transverse wakefield, which appears in Table 3.10, is used in the computation of the transverse stability of the drive beam (Section 3.5.1).

Transverse mode damping

The PETS has been equipped with transverse mode dampers, which consist of four corrugated slits oriented at 45 degrees in the transverse plane in order to intercept the image current of the transverse mode. The slits are closed at their outer ends with respect to the beam chamber by RF loads made of silicon carbide (SiC). The position of the dampers is chosen to be in the symmetry planes such that the main mode is not affected by their presence. Extensive simulations have been necessary to optimize the damping channels and the loads in order to obtain the lowest possible Q value for the main deflecting mode [3.29].

PETS integrated longitudinal electric field uniformity

Because of the particular geometry of the PETS, the integrated decelerating field varies as a function of the angular and radial position within the beam chamber. In particular the integrated field increases as one moves towards the waveguides, while it decreases to zero towards the chamber walls. The non-uniform beam deceleration causes the particles to receive transverse kicks, which are functions of the particle position within the PETS chamber. The overall result found in tracking programs is that the drive beam would be unstable if no cure were found for the problem. One possible simple solution consists in rotating by 45 degrees every other PETS in the decelerating linac so that a particle off-centre at $\varphi = 0$ in a structure would be at $\varphi = 45$ degrees in the following one, thus averaging out the field non-uniformity. The useful effect of the alternate PETS rotation is somewhat reduced by the betatron motion of the particles in the drive linac lattice. Tracking programs have shown, however, that the overall result is beneficial to the transverse beam stability and worth the implementation effort [3.28].

3.5.2.4 The six-waveguide structure

One alternative approach to solve the problem of field non-uniformity in the PETS consists in increasing the number of waveguides in the structure. Figure 3.26 shows the six-waveguide structure with beam aperture diameter of 30 mm.

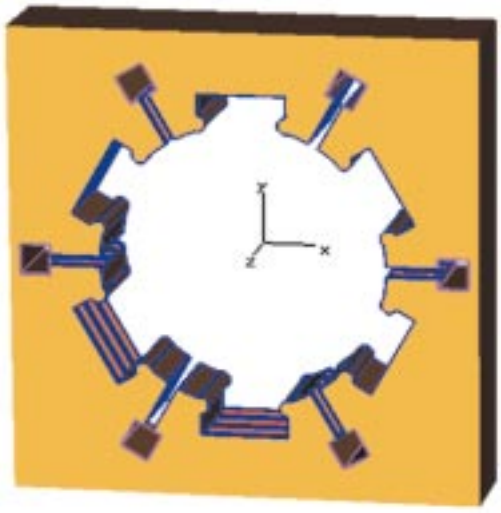

Fig. 3.26: *Six-waveguides PETS.*

The geometric and RF parameters are listed in Table 3.11.

Table 3.11: Parameters of the six-waveguide PETS

Beam chamber diameter	30.00 mm
Synch. mode β_g	0.53 c
Synch. mode R'/Q	50.4 linac Ω/m
Peak transverse wakefield	0.25 V/pC/mm/m
Transverse mode Q-value	170

The radial integrated field distribution is more favourable with respect to the four-waveguide structure with the same chamber aperture. We can take advantage of the alternate rotation (by 30 degrees in this case) of the successive structures and obtain a very uniform averaged integrated field up to a radius of 13 mm. The six-waveguide structure represents a very promising alternative to the four-waveguide structure with one drawback being its mechanical complexity. The output RF couplers for this structure have yet to be designed, but ideas exist on possible solutions. On the positive side, this geometry offers a larger beam aperture than the four-waveguide PETS for a given output power and consequently the transverse mode loss factor is lower.

3.6 Power transfer efficiency

One of the most important features in a high-energy linear collider is the power transfer efficiency. A list of efficiencies for different components of the design considered is shown in Table 3.12, although it is too early to know the precise values for all of the subsystems. The target efficiencies are listed in the Table together with the more conservative values which have been assumed in the present report. Figure 3.27 shows the power flow of the whole CLIC complex, from the wall plug to the main beam.

Table 3.12: Component efficiencies (%)

Item		Assumed	Target
Modulator	η_M	90	92
Klystron	η_K	65	70
drive-beam acceleration*	$\eta_S\,\eta_A$	93	94
Decelerator	$\eta_{D,extr}$	82	85
Power extraction	η_{PETS}	95	97
Power transfer	η_{transf}	95	97
Wall plug to RF	$\eta_{plug/RF}$	40.3	48.4
RF to main beam	$\eta_{RF/main}$	24.4	24.4
Overall	η_{tot}	9.8	11.8

* *Product of the efficiency of the structures η_S by the acceleration efficiency itself η_A (for off-crest acceleration and feedback overhead).*

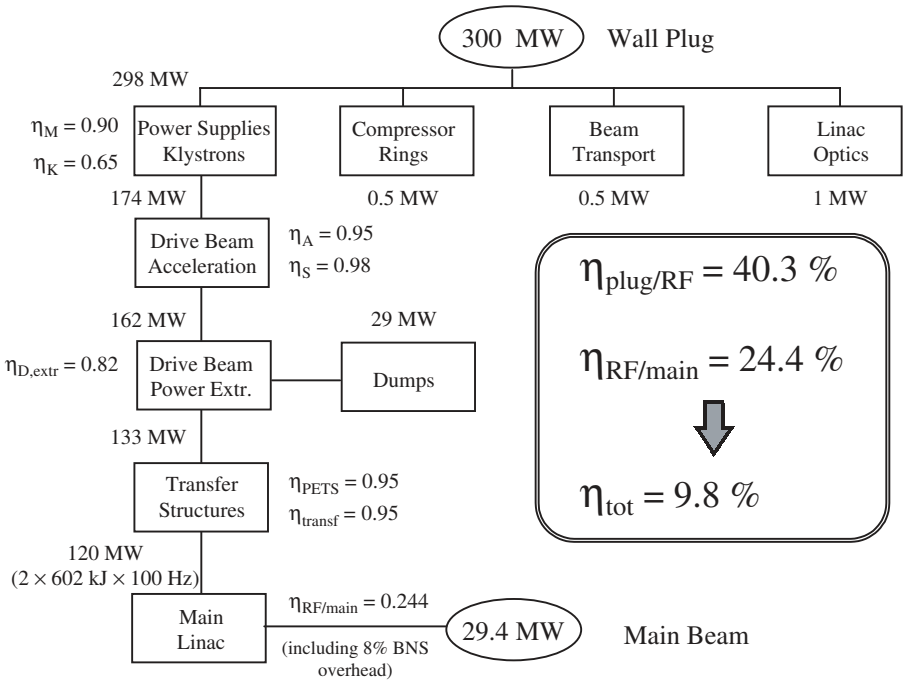

Fig. 3.27: *Power flow diagram for CLIC (3 TeV c.m. energy), from wall plug to main beam.*

This diagram does not take into account the power needed for the cooling of the beam dumps, of the accelerating structures, and of all the other components. Typically, direct cooling with water consumes about 3% of the dissipated power, while air cooling is more expensive (about 40%). Assuming the use of water cooling whenever possible without additional costs, one obtains an additional wall-plug power of about 16 MW (280 MW water-cooled, i.e. 8.4 MW consumption, plus 20 MW air-cooled, corresponding to 8 MW consumption). The total installed cooling capacity (cooling towers) naturally does not need to be larger than the total wall-plug power, but depending on the specific mode of operation, the water flow may need to be shunted to particular loads or dumps. This requires a redundant plumbing, a cooling control, and an interlock system. Each installed load must be able to handle the maximum power possible at this location [3.30].

Another issue, which is not covered here, is the need for some operational overhead in the drive-beam accelerator. Additional klystrons could be needed for a fast substitution of failing tubes. If these klystrons feed structures permanently installed in the beam line, they should constantly provide power to compensate for the local beam loading. Depending on the expected failure rate and on the scenario chosen for the overhead, the additional power needed could be as high as 40 MW [3.30].

References

Introduction (Section 3.1)

[3.1] A.M. Sessler, The FEL as a power source for a high gradient accelerating structure, AIP Conf. Proc. 91 (Ed. P.J. Channel), p. 154 (1982).

[3.2] H.H. Braun et al., The CLIC RF Power Source. A Novel Scheme of Two-Beam Acceleration for Electron–Positron Linear Colliders, CERN 99–06 (1999).

[3.3] R. Corsini and J.-P. Delahaye, The CLIC multidrive-beam scheme, CERN/PS 98–008 (LP) (1998) and CLIC Note 331 (1998).

Drive-beam injector (Section 3.2)

Overview of the system (Section 3.2.1)

[3.4] L. Rinolfi, O. Kester and R. Rao, Beam emittance measurements from CERN thermionic gun, Proc. 3rd Eur. Part. Accel. Conf. (EPAC92), Berlin, 1992, Eds. H. Henke, H. Homeyer and C. Petit-Jean-Genaz (Edition Frontières, Gif-sur-Yvette, 1992) and CERN/PS/92–12 (LP) (1992).

Beam dynamics simulations (Section 3.2.3)

[3.5] B. Mouton, The PARMELA program, Report LAL-SERA 93–455, Laboratoire de l'Accélérateur Linéaire, Orsay, France (1993).

Drive-beam accelerating linac (Section 3.3)

The accelerator beam dynamics (Section 3.3.1)

[3.6] K. Bane, M. Timm and T. Weiland, DESY-M-97-02 (1997).

[3.7] L. Thorndahl *in* H.H. Braun et al., The CLIC RF Power Source, CERN 99–06 (1999).

[3.8] D. Schulte, Stability of the CLIC drive-beam accelerator, Proc. 19th Int. Lin. Accel. Conf. (LINAC'98), Chicago, 1998 and CERN-PS-98–042-LP (1998).

[3.9] D. Schulte, The Drive-Beam Accelerator of CLIC, Proc. of VIIIth Int. Workshop on Linear Colliders (LC99), Frascati, 1999, Eds. J.-P. Delahaye, G. Guignard, K. Hübner et al., URL: http://wwwsis.lnf.infn.it/talkshow/lc99/Schulte2b/talk.pdf

Description of the accelerator cavities (Section 3.3.2)

[3.10] M. Luong, private communication.

[3.11] R.H. Siemann, Linear colliders: the last ten years and the next ten years, SLAC-PUB-6417 (1994).

[3.12] L. Thorndahl, private communication.

Drive-beam power systems (Section 3.3.3)

[3.13] A. Beunas, Thomson Tubes Electroniques, Paris, private communication.

[3.14] P.D. Pearce et al., A klystron-modulator RF power system for the CLIC drive-beam accelerators, 24th International Power Modulator Symposium, Norfolk, Virginia, June 2000.

Frequency multiplication and pulse compression (Section 3.4)

Design of the delay line and combiner rings (Section 3.4.1)

[3.15] J.B. Murphy, S. Krinsky and R.L. Gluckstern, *Longitudinal wakefield for an electron moving on a circular orbit,* Part. Accel. **57** (1997) 9.
[3.16] L. Thorndahl, private communication.
[3.17] G. Guignard and E.T. D'Amico, A new family of isochronous arcs, CERN/SL 95–24 (AP) and CLIC Note 280 (1995).
[3.18] R.C. York and D.R. Douglas, Optics of the CEBAF CW superconducting accelerator, Proc. 12th Particle Accelerator Conference, Washington, DC, 1987 (IEEE, New York, 1987).
[3.19] Ph. Bernard, H. Lengeler and V. Vaghin, New Disk-Loaded Waveguides for the CERN RF Separator, CERN 70–26 (1970).

Transfer lines, compressors, path-length chicanes and loops (Section 3.4.2)

[3.20] E.T. D'Amico and G. Guignard, Tunable achromats and CLIC applications, Proc. EPAC2000, Vienna, June 2000.

Drive-beam decelerator (Section 3.5)

Lattice and beam stability (Section 3.5.1)

[3.21] A. Riche, Maximum energy transfer efficiency in CLIC drive beam and proposal for a method of focusing, CLIC Note 266 (1994)
[3.22] A. Riche and D. Schulte, The drive-beam decelerator of CLIC, Proc. 19th Int. Lin. Accel. Conf. (LINAC98), Chicago, 1998 and CERN-PS 98–043-LP (1998).
[3.23] A. Riche, To be published.
[3.24] D. Schulte, PLACET: a program to simulate drive beams, Proc. EPAC2000, Vienna, June 2000.
[3.25] A. Millich, A. Riche and D. Schulte, Beam stability in the CLIC drive-beam decelerator using structures of high-order symmetry, Proc. Part. Accel. Conf. (PAC99), New York, 1999, Eds. A. Luccio and W. MacKay (IEEE Computer Soc. Press, Piscataway, N. J., 1999) and CERN-PS 99–028-LP (1999).

The Power Extraction and Transfer Structure (Section 3.5.2)

[3.26] W. Schnell, The study of a CERN linear collider, CLIC, Linear Accelerator Conference, Williamsburg, 1988.
[3.27] G. Carron and L. Thorndahl, Impedance and loss factor measurements on a CLIC Transfer Structure (CTS), Proc. 3rd Eur. Part. Accel. Conf. (EPAC92), Berlin, 1992, Eds. H. Henke, H. Homeyer and C. Petit-Jean-Genaz (Edition Frontières, Gif-sur-Yvette, 1992).
[3.28] G. Carron, A. Millich and L. Thorndahl, The 30 GHz transfer structure for the CLIC study, International Computational Accelerator Physics Conference (ICAP 98), Monterey, 1998.
[3.29] M. Luong and I. Syratchev, Simulations of the damping of the power extraction and transfer structure, Proc. EPAC2000, Vienna, June 2000.

Power transfer efficiency (Section 3.6)

[3.30] R. Pitthan, private communication.

4 Auxiliary Systems

4.1 Machine protection system

The two beams of the CLIC complex carry a very high amount of energy (about 296 kJ and 1624 kJ for the main beams and drive beams, respectively) which is large enough to induce severe damage in terms of heat deposition, shock wave and melting of structure even if only a fraction of their intensity is accidentally lost. The power of the drive beams is almost two orders of magnitude greater than for any existing electron linac. Thus great care should be taken during the design of the machine to assess any potential damage.

The purpose of the Machine Protection System (MPS) is to provide the means of protecting the equipment from abnormal beam behaviour. The extent of the MPS depends on the compromise between accepted risk and financial constraints. Three major types of components should be considered: i) intrinsically secure devices; ii) a fast interlock like system, which could handle abnormal pulses in order to reduce significantly possible damage; iii) the hardware and software required by MPS to ensure the overall level of safety of the CLIC complex. In addition, all these components can be classified independently of their type on the basis of their action on the beam, as proposed in Table 4.1.

Table 4.1: Proposed definition of component classes

Class number	Description
1	No direct or indirect action on the beam.
2	Possible action, but not directly observable. Statistical indicators like Mean Time Between Failure and Mean Time To Repair may be used.
3	Static equipment (not pulsed) acting on the beam. Access to its status is available. Intrinsic safety should be preferred. If it is not possible then at least preventive maintenance and evaluation of statistical indicators (as in class 2) should be provided.
4	Pulsed equipment acting on the beam. Check-point readings are available. Slow drift and peak-to-peak fluctuations should be monitored and kept within a given range.
5	Fast-pulsed equipment acting strongly on the beam. No significant information available at check-point time. Actual parameter must be acquired at beam time, and pulse-to-pulse fluctuation should be within acceptable boundaries.
6	Fast-pulsed equipment. No significant data can be directly acquired. Indirect parameters have to be defined. Same treatment as for class 5.
7	MPS itself. Redundancy can be requested in the system. Acceptance and validation test of the system must be defined and executed by an independent body. Regular no-regression test must be done. Any upgrade must be treated as a new installation.

The MPS must also ensure a safe transition from the rest state (shutdown or no beam) to the nominal regime expected by the physics experiments.

Beam damage by stray beam

The energy stored in a drive beam (812 kJ) is sufficient to melt 1.5 kg of copper, or to pierce a hole of 10 mm diameter and 2 m length. At a momentum of 1.18 GeV/c the range of electrons in copper is about 150 mm and the beam size should be enlarged up to at least a diameter of 35 mm to avoid the melting of any copper structure. In each decelerator section the energy, although divided by 22, is large enough to melt 30 g of copper. Even if the beam is only partially lost and no melting occurs, the thermal shock and the induced stress and deformations would be such that the structure will be unable to work correctly.

Machine protection principle

The machine protection is a set of passive, active, and predictive systems, which will ensure that the complex will not approach the boundary of the safe region for the current working point. The safe region is a hypervolume (n dimensions in CLIC complex equipment parameters) in which the damage risk is declared to be acceptable. This volume is a function of the instantaneous working point defined by the beam momentum, beam total charge, beam structures for each of the beams in the complex. The predictive system will assess the state of the complex at a certain time before the beam runs, and decide on a 'Go, No-Go' for the next pulse. It should use all the data available on the complex and carry out sophisticated treatments such as statistical analysis or determination of trend evolution. The active systems should avoid that a too large amount of energy is lost in an uncontrolled way, once an abnormal situation is detected. The passive systems are built in such a way that they cannot accidentally endanger the CLIC complex.

Passive systems

The typical example of a passive system is the magnet for which large enough yoke lamination will ensure a long enough magnetic field decay time whatever the state of the coil and the power supply. Another case is the dynamic alignment system which should ensure that the mechanical inertia is large enough to maintain any movements in an acceptable range even if the maximum torque is applied by accident to the driving motor.

Active systems

For the main beams, a fast beam-kill system must be provided at the exit of the damping rings. It will be used when the beam parameters become abnormal during the damping process (which take a few milliseconds), or when bad beam conditions are detected in the drive beams during the combining process. Action can probably be taken only on a pulse-to-pulse basis because the duration of the main beam pulse itself (102 ns) is too short to permit a partial dumping of the beam when an abnormal state is detected in the head of the beam during the acceleration process. Beam collimation can also be used to reject off-momentum beam pulses. Chicanes and combiner rings can be used to measure the momentum of the drive beams and fast feedback can react on the gun or on the kickers to partially dump the beam. Fast beam-intensity-measurement devices can be useful to reject beam pulses with charges out of tolerance. The second combiner ring, where the drive beam remains for about 4 μs, is the last point where it is possible to decide to dump the beam during the extraction process. A detailed analysis of the instrumentation and actuators will be needed in order to decide on the best methods to use. The time required by the measurement, discrimination of the results, and the decision process are very sensitive parameters of the efficiency of the system.

Predictive system

The main duty of the system is to obtain all the elements required to take the 'Go No-Go' decision before any pulse. This decision will be taken after data sampling and collection of the state of every sensitive system in the complex and after assessing the margin between the current position in the CLIC complex state hypervolume and the boundary of the safe domain according to the current working point. The second aim of this system is to ensure that any action (by operators or any automated process) will never drive the complex outside the current safe domain. The processing complexity is such that very fast networking and digital data processing will be required. It is very important to observe that the sampling of the state of the system cannot be done later than 200 μs before the decision has to be taken. This system must also inform the operation crew about the safety margin, and provide early warning when slow drift in a subsystem becomes dangerous. For any 'No-Go' decision the system will force the complex to fall back immediately into the safe regime. From then on it will guarantee that the checklist is applied and successfully gone through before restarting the ramping procedure to restore the nominal working point. The loss of physics time due to a 'No-Go' decision can be of the order of one hour. Thus it is essential to keep down the number of wrong decisions. Sophisticated techniques and methods like those developed in the aerospace industry have to be studied.

The CLIC operation case

The main aim of the CLIC operation is to maintain the parameters of the CLIC complex in the nominal domain. It must also ensure that the phase transition from the no-beam situation to the nominal working point, or from this one to another one according to the physics schedule, is correctly carried out. These transitions must follow a very controlled and stable path. To be able to define these transition procedures, the overall stability of the CLIC

complex should be carefully studied. The stability margin must be quantified, and fast and sure procedures should be developed. These could be validated by a global simulation system, which will also be very valuable for the training of the operation crew.

4.2 Beam dumps

The CLIC complex is equipped with two classes of beam dumps.

Beam dumps for normal operation:

1) After the experimental collision point for the main beams (a pair in each detector zone). These dumps must be able to absorb the full main-beam power at the nominal repetition rate (14.8 MW). Given the proximity of the interaction area, the control of the vibrations generated by such dumps is a critical issue. A possible solution to prevent excessive acoustic emission in the dumps could be to make them out of water at 4°C [4.1].
2) Beam dumps for the remaining portion of drive beams at the exit of the deceleration section (1–2 MW each). A possible layout of such a beam dump is given in Fig. 3.20 [3.2]. The beam must be diverted into a water-cooled dump placed in an excavated niche. For this purpose, the beam is first deflected using a dipole of angles ranging from say 25 to 250 mrad, which generates a large spatial dispersion. After the dipole, a string of half-quadrupoles could be used to give more deflection and to allow the beam to continue to the dump without excessive transverse growth. The dump itself could be of the SLAC type in which the beam power is absorbed in a water-cooled bed of aluminium spheres [4.2].

Beam dumps for abnormal pulses:

1) For the main beams at the exit of the damping rings, and within, or close to the collimator in the final focus region. These dumps do not need to function at the nominal repetition rate.
2) For the drive beams: at the exit of combiner rings, possibly at the exit of the delay loop and at the end of the transfer line in the main tunnel. Their exact number and positions must be defined according to the chosen active protection systems.

The total energy deposited in the operation dumps is quite large (in the range 75–100 MW) and energy recycling should be envisaged.

References

Beam dumps (Section 4.2)

[4.1] J.-B. Jeanneret and E. Wildner, Thermal and acoustic effects in CLIC beam absorbers, CLIC Note 421 and CERN/SL–99–072 (1999).

[4.2] D.R. Walz and L.R. Lucas, SLAC–PUB–555 (1969).

5 CLIC Test Facilities and the Route to CLIC

5.1 The various stages and a possible schedule

The basic principles of the two-beam acceleration technique have been established in the first two CLIC test facilities, i.e. CTF1 [5.1], which is now out of operation, and CTF2 [5.2], which is still running. It is now proposed to demonstrate the overall feasibility of the many key issues which are specific to the CLIC scheme in two distinct successive stages.

The first stage, which would take five years, would be to build and exploit a new test facility (CTF3) which would demonstrate the feasibility, and test all the critical components of the RF power generation scheme albeit on a much smaller scale and with the drive linac at a different (higher) frequency. This facility would be housed in the present LPI (LIL+EPA) buildings.

The second stage, which would come immediately after CTF3 and which would take about five years, would be to build a limited, first-phase version (CLIC1) of the real CLIC power source to produce just one single-drive-beam unit rather than the multiple drive-beams it would ultimately be required to produce. This drive-beam would have the nominal CLIC energy and current, and would provide enough power in a ~ 624 m long section of the CLIC linac to accelerate a multibunch beam to 68 GeV. Since this is a final test of the CLIC scheme, all components will be definitive ones and, given a positive outcome of the test, would be used for the final construction.

Details of future CLIC studies and the new test facility (CTF3) are described in Ref. [5.3].

5.2 CLIC Test Facilities

5.2.1 CTF1 overview and results

The technical feasibility of two-beam acceleration was first demonstrated in the CLIC Test Facility CTF1 [5.1] which was built to (i) study the production of short, high-charge electron bunches from laser-illuminated photocathodes in RF guns, (ii) generate high-power 30 GHz RF pulses by passing bunch trains through energy extraction cavities for testing CLIC prototype components, (iii) test beam-position monitors. A layout of CTF1 is shown in Fig. 5.1. A 3 GHz 1.5-cell RF gun equipped with a laser-driven photocathode and operating at 100 MV/m produced a bunched beam with a momentum of 4.5 MeV/c. A solenoid at the outlet of the gun provided some focusing of the beam before it was accelerated to 12 MeV/c in a four-cell standing wave gun-booster cavity. Final acceleration to 65 MeV/c was obtained using a 1 m long travelling-wave section — provided by LAL. Energy was extracted from the beam by a 30 cm long travelling-wave section (CAS1) to provide short high-power 30 GHz RF pulses. This power was in turn fed to a second identical CLIC structure (CAS2) to produce high accelerating gradients. The decelerated beam then either went to a dump, or was turned through 180° by bending magnets at the end of the line and re-accelerated by the second high-gradient CLIC section. The facility was operated in either single-bunch or multi-bunch mode at a repetition rate of 10 Hz. Multiple bunches were made by splitting the laser pulse into a train of pulses each spaced by one 3 GHz wavelength. The synchronized laser system had been optimized at the fourth harmonic (262 nm) providing a maximum energy of 0.5 mJ per pulse (before splitting) and a pulse length of 8 ps FWHH. After an initial period of operation with CsI photocathodes, Cs_2Te photocathodes were later used. These photocathodes were prepared in the laboratory and transported under vacuum and installed in the gun using a specially designed transfer system. The RF gun produced 35 nC in a single bunch and 450 nC in a train of 48 bunches. Only a small fraction of this charge, however, could be transported to the dump. The maximum 30 GHz RF power produced was 76 MW for 3 ns. The highest average accelerating field in the second CLIC accelerating structure was 94 MV/m.

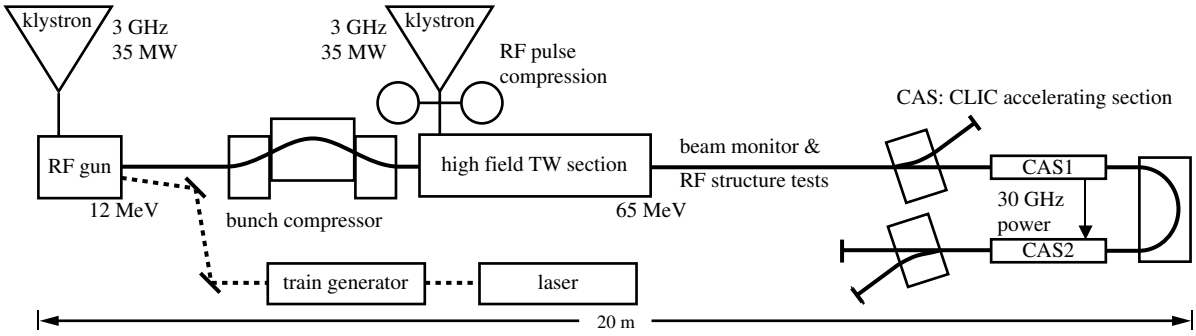

Fig. 5.1: *Layout of the facility CTF1, which is now out of operation.*

5.2.2 CTF2 overview and results

With the second CLIC Test Facility, CTF2 [5.2], a real two-beam accelerator, with separate drive and main beams, was built and successfully operated. A string of 30 GHz, low-impedance, power-extracting structures is used to decelerate the high-charge drive beam. The extracted 30 GHz power is transferred to a string of high-impedance structures accelerating the low-charge probe beam. A layout of CTF2 is shown in Fig. 5.2. The 30 GHz part of this facility is equipped with an active-alignment system with a few-microns precision. The 48-bunch 450 nC drive-beam train is generated by a laser-driven S-band RF gun with a Cs_2Te photocathode (PC). It is accelerated to 40 MeV average by two travelling-wave structures (TWS) operating at two slightly different frequencies to provide beam-loading compensation along the train. After bunch compression in a magnetic chicane, the bunch train passes through four Power Extraction and Transfer Structures (PETS) each of which powers one 30 GHz accelerating structure (CAS) (except the third which powers two) with 16 ns long pulses. The single-probe beam bunch is generated by an RF gun with a CsI+Ge PC. It is pre-accelerated to 45 MeV at S-band before being injected into the 30 GHz accelerating linac. The drive-beam RF gun produced a single-bunch charge of 112 nC and a maximum charge of 755 nC in 48 bunches. The maximum charge transmitted through the 30 GHz modules is 450 nC. A series of cross-checks between drive-beam charge, generated RF power, and main-beam energy gain have shown excellent agreement. A consistent set of values are given in Table 5.1 for two 30 GHz modules with one PETS feeding one CAS. The highest accelerating gradient obtained is 59 MV/m and the energy of an 0.7 nC probe beam has been increased by 55 MeV. Extremely high gradients [5.4] were obtained by powering a 30 GHz single-cell resonant cavity directly by the drive beam. The cavity operated without breakdown at a peak accelerating gradient of 290 MV/m. When pushed further, the cavity started to break down at surface-field levels around 0.5 GV/m. The breakdown manifested itself as a field extinction of the decaying pulse at different times in the pulse. At the end of the test, when the cavity was breaking down continuously, surface-field levels as high as 750 MV/m were obtained.

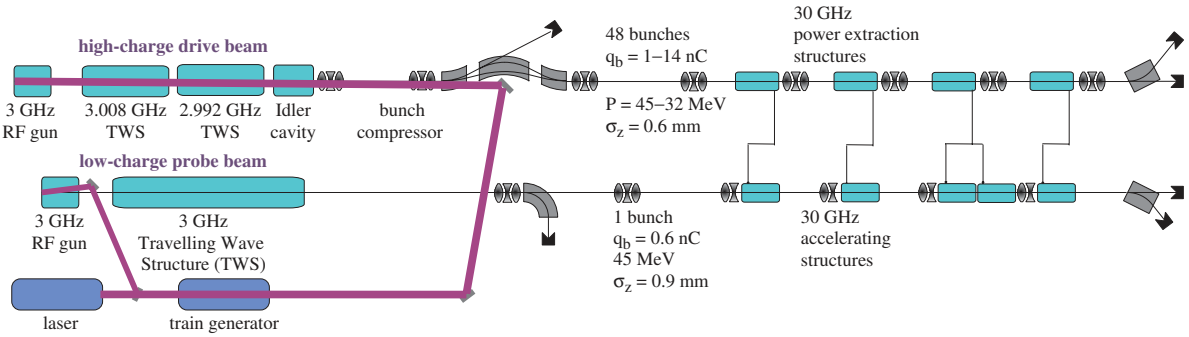

Fig. 5.2: *Layout of the present facility CTF2.*

Table 5.1: A consistent set of measured values from two 30 GHz modules in CTF2

Q_{train}	375 nC
Q_{bunch}	7.8 nC
Power out of PETS1 and PETS2	27 MW and 22 MW
Power into CAS1 and CAS2	21 MW and 17 MW
Field in CAS1 and CAS2	57 MV/m and 51 MV/m
Total probe beam acceleration	30.5 MeV

5.2.3 CTF3 description

5.2.3.1 Outline of the proposed CTF3

Since CLIC1 is a very large and expensive installation, a much smaller facility (CTF3) [5.3] is proposed as a first intermediate step to demonstrate the technical feasibility of the key concepts of this new RF power source, e.g., generation of interleaved bunch trains, operation with a fully-loaded drive-beam accelerator, and generation of accelerating gradients of 150 MV/m. The new CLIC Test Facility (CTF3) is shown in Fig. 5.3. To reduce costs, CTF3 differs from the RF power source proposed for CLIC in the following ways (Table 5.2).

The frequency of the drive-beam accelerator is chosen to be 3 GHz instead of 937 MHz. This enables the 3 GHz klystrons, modulators, RF power compression units, and waveguides from the LEP Injector Linac (LIL) Complex to be used for power production which is always very costly. With 10 of these modulator/klystron units the drive-beam energy for a current of 3.5 A (~ half the nominal CLIC current) is 184 MeV — this is very low compared to the 1.18 GeV for CLIC and obviously makes operation more difficult, but simulations indicate that it works. CTF3 only has the first two stages of the beam combination scheme, namely the times-2 Delay Line Combiner and the first Combiner Ring. The second (×4) large circumference Combiner Ring is very expensive and since it has the same scheme of combination it is not considered to be essential for this first demonstration test facility. The compression factor for the first Combiner Ring has, however, been increased from 4 for CLIC, to 5 for CTF3, to obtain an overall compression of 10. This gives a final bunch spacing of 2 cm (the same as in CLIC) for production of power at 30 GHz. Because of space limitations, it is unlikely that the circumference of the Combiner Ring can be made smaller than 84 m. This results in a final pulse length of 140 ns rather than the nominal CLIC value of 130 ns. The modulators produce a maximum RF pulse of 6.7 μs which after power compression with LIPS (×2.3) becomes ~1.6 μs. This beam pulse is long enough after a (×10) frequency multiplication to produce the required final 140 ns pulse. The drive-beam decelerator is limited to a total length of about 10 m (four transfer structures) compared to 624 m for CLIC. To limit the radiation produced by CTF3 it is proposed to run at 5 Hz instead of 75 Hz.

The new facility will be housed in the existing LIL and EPA buildings and use will be made of many of the LIL and EPA components. As mentioned above, an 84 m circumference ring appears just to fit in the EPA.

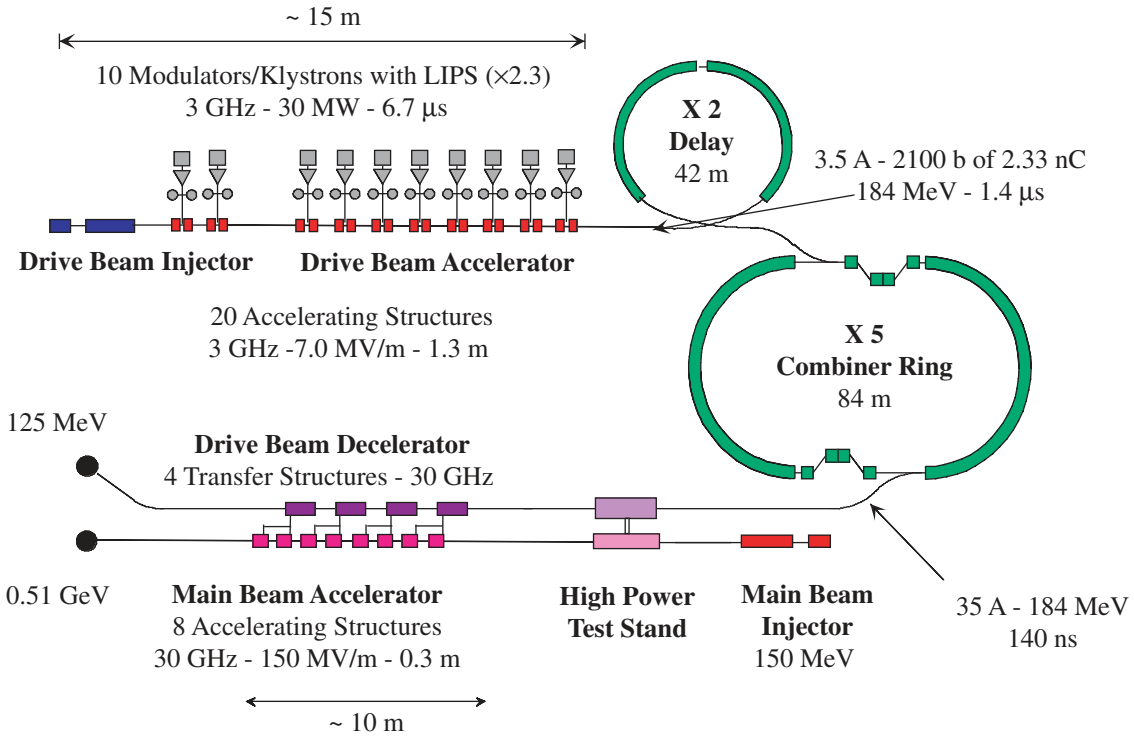

Fig. 5.3: *Schematic layout of nominal phase of CTF3.*

Table 5.2: Comparison of CTF3, CLIC1 and CLIC (3 TeV) parameters

		CTF3	CLIC1	CLIC
Accelerating frequency	(GHz)	30	30	30
Main linac accelerating gradient	(MV/m)	150	150	150
Number of accelerating structures per linac		8	976	22×976
RF pulse length	(ns)	140	130	130
Main beam acceleration per drive beam	(GeV)	0.36	68	68
Number of transfer structures per linac		4	488	22×500
Number of drive beams per linac		1	1	22
Frequency of drive-beam accelerator	(MHz)	3000	937	937
Drive-beam energy	(MeV)	184	1180	1180
Average drive-beam current before compression	(A)	3.5	7.5	7.5
Number of klystrons		10	46	182
Number of RF power compressors		10	46	0
Drive-beam pulse length before compression	(μs)	1.40	4.16	92
Interval between bunches before compression	(cm)	20	64	64
Delay line combiner		42 m (×2)	39 m (×2)	39 m (×2)
First combiner ring		84 m (×5)	78 m (×4)	78m (×4)
Second combiner ring		NO	312 m (×4)	312 m (×4)
Overall frequency multiplication		10	32	32
Final average drive-beam current after compression	(A)	35	240	240
Interval between bunches	(cm)	2	2	2
Drive-beam energy per pulse	(kJ)	0.8	37	814
Repetition frequency	(Hz)	5	100	100
Average beam power	(kW)	4.1	3690	81×10^3
Drive-beam energy on beam dump	(MeV)	125	118	118

5.2.3.2 The main CTF3 subsystems

Injector

The injector consists of a pulsed thermionic gun followed by one or two subharmonic (1.5 GHz) pre-buncher cavities, two 3 GHz pre-buncher and buncher cavities, and two 3 GHz damped/detuned accelerating structures (see section on drive-beam accelerator below). All the injector components sit in a solenoidal-focusing field. The final beam energy is about 26 MeV. The pre-buncher creates bunches with a spacing of 20 cm. Depending on the phase of the subharmonic pre-buncher, these bunches fall into either even or odd RF buckets of the 3 GHz system where they are trapped and accelerated. With the phase set at 0 degree, most of the charge (the process is not 100%) goes into bunches occupying only even 3 GHz buckets (in fact every other even bucket). As the phase of the subharmonic cavities is varied from 0 degree to +180 degrees, the intensity of the charge of the bunches in the even buckets is reduced and that in the odd buckets increased until there is charge in the bunches in the odd buckets only. This produces the drive-beam structure shown in Fig. 5.4. It is hoped that the phase switch can be done within 4 ns. A very broad-band power supply and a low-Q (~10) subharmonic buncher cavity are required in order to be able to switch in such a short time. This may not be feasible but it will only be known when the hardware has been tested. A longer switching time makes the system less efficient. The normalized emittance of the bunched beam at the exit (~26 MeV) is required to be <100 mm·mrad with an r.m.s. bunch length <1.5 mm.

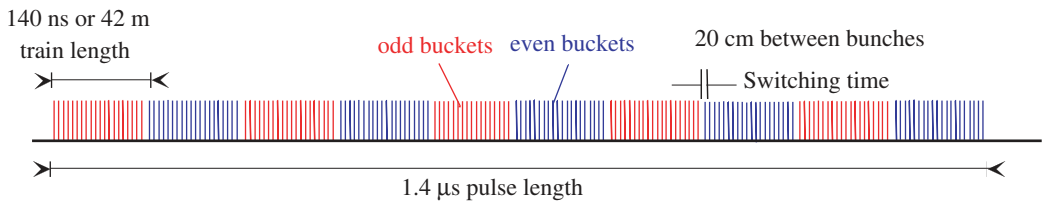

Fig. 5.4: *Bunch train structure.*

An interesting alternative is to use a photo-injector consisting of a laser-illuminated photocathode in a high-gradient RF gun. This has the advantage of producing very short, low-emittance bunches. The bunch train structure could be generated directly by a suitable phasing of the laser pulses. The present CTF2 gun design with some modifications would be suitable for the RF gun, but the laser required for such a system has a specification which is beyond anything that exists today and an intense R&D programme would be necessary to determine if such a laser is indeed feasible and at what cost.

Drive-beam accelerator

The 3 GHz drive-beam accelerator increases the beam energy from ~26 MeV to 184 MeV using 16 out of 20 normal-conducting TW structures operating at 7.0 MV/m (4 structures being included in the drive-beam injector with solenoid focusing). This linac has a conventional quadrupole FODO focusing. To maintain beam stability in both this linac and the 26 MeV injector linac the transverse wakefield levels have to be damped to Q-values of $\tilde{<}$ 100. This will be done by building new structures with waveguide damping and detuning [the accelerating structures of the LEP Injector Linac (LIL) cannot be used because of beam instabilities above 50 mA, and excessive beam loading effects]. The structure design will be based on one developed for the CLIC 30 GHz main-linac accelerating structures. The RF power is supplied by 30 MW klystrons. After compression by a factor 2.3 by the existing RF pulse compression system (LIPS) and splitting of the power, ~34.5 MW are provided at the input to each 1.3 m long structure. Operating this linac in the fully-loaded condition results in an RF-to-beam efficiency of ≈96%. Since the bunch train charge is essentially constant along the 1.4 μs pulse, the beam-induced energy spread is very small. A correlated single-bunch energy spread is introduced in the drive-beam accelerator by a combination of off-crest running and beam loading for BNS stabilization, and so that the bunches can be compressed at a later stage. At the end of the accelerator there are ~2100 bunches of 2.33 nC per bunch, this corresponds to a current of 3.5 A averaged over the train. The total single-bunch energy spread is expected not to exceed 1% approximately, and the bunch-to-bunch energy spread must remain an order of magnitude smaller. The length of the accelerating structure (1.3 m) has been chosen to give maximum RF-to-beam efficiency with a current of 3.5 A when powered with 30 MW klystrons. Since this is also the optimum length of structure for 4 A when powered with 40 MW klystrons, it is proposed to replace 30 MW klystrons when they fail with 40 MW klystrons so that there will be a natural progression towards higher currents (4 A) and slightly higher energies (200 MeV).

Delay line combiner

The continuous train of bunches is split by the combiner delay line into a series of 42 m long bunch trains with 42 m gaps. It also produces a frequency multiplication (×2) by interleaving the bunches in the even buckets with the bunches in the odd buckets to produce a bunch spacing of 10 cm. The two RF transverse deflectors in this line are short, 1.5 GHz, travelling-wave, iris-loaded structures whose fundamental mode is a deflecting hybrid mode. To prevent bunch lengthening, the lattice has to be isochronous. At the exit of the delay line the pulse current is 7 A.

Ring combiner

A further frequency multiplication (×5) is obtained in the 84 m circumference combiner ring corresponding to a final bunch spacing of 2 cm. This ring is more like a transport line than a storage ring because there is no RF acceleration and the bunch trains make at the most a few turns (the first train makes $4\frac{1}{2}$ turns and the fourth train makes only half a turn). Since the CTF3 and CLIC frequency multiplication factors are different, the way in which the trains are combined is also slightly different (see the caption of Fig. 5.5).

Injection into the ring is made using a septum and two transverse RF deflectors (Fig. 5.5). The existing injection septum of EPA can be used for this purpose. The injection and extraction systems are located at a distance of half the ring circumference from each other. Beam loading and transverse wakefields in the 3 GHz transverse deflecting structures are a concern because the decrease of the transverse kick along the train will produce variations in transverse position of the bunches.

To prevent bunch lengthening, the combiner ring lattice has to be isochronous. In fact, since the fifth bunch train makes only half a turn in the ring, each half-ring also has to be isochronous. The suitability of using existing bending and quadrupole magnets of the LPI Electron Positron Accumulator (EPA) in the ring is being studied. The bunch length is kept relatively long in the combiners (~1.5–2.5 mm r.m.s.) to prevent the emission of coherent synchrotron radiation which increases the single-bunch energy spread as well as decreasing the average energy. The 140 ns bunch train is extracted from this ring using a pulsed kicker and a septum magnet both of which can be taken from EPA. At the ring-exit the peak current is 35 A.

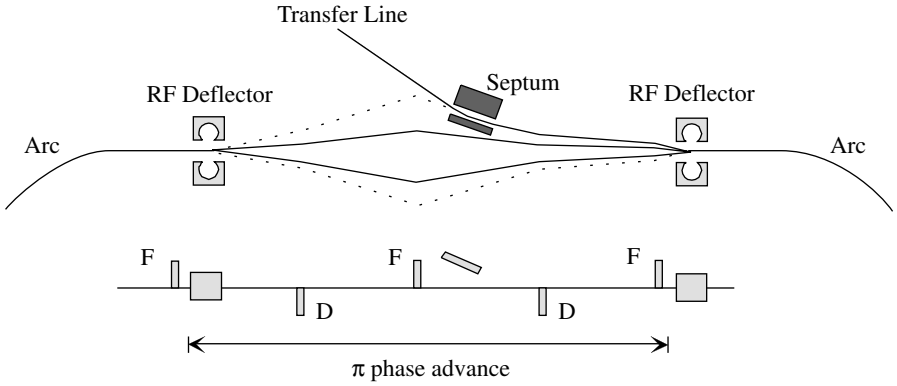

Fig. 5.5: *RF deflector injection insertion layout and lattice. Circulating bunches travel on the full-line orbits while the injected bunches are kicked by the second deflector onto the equilibrium orbit of the ring. The maximum outer trajectory (shown dotted and intercepting the septum) is never followed, since the whole bunch train is ejected before any of the circulating bunches reach the corresponding phase in the first deflector. The maximum inner trajectory (also shown dotted) is not used either.*

Bunch-length tuning module

The bunch length will be tunable in the transfer line between the drive-beam accelerator and injection into the combiner ring so that coherent synchrotron radiation effects in the ring produced by the high-charge short bunches can be both controlled and studied. A design has been found [5.5] which incorporates this bunch-length tuning which is able to compress or stretch the bunches, in the strong-bending modules of the transfer line.

Bunch compressor

Owing to the unusual bunch energy correlation, the final bunch compression after extraction from the ring cannot be done with a simple three bending-magnet chicane because its optics does not have the correct sign of the R_{56} matrix element, so a more complicated design has to be worked out which will certainly take up more space. The final r.m.s. bunch length for efficient production of 30 GHz RF power is ~0.5 mm.

5.2.3.3 Main tests planned in CTF3

Two-beam test accelerator

The final 35 A drive beam will have an energy of 184 MeV and will consist of bunches with a charge of 2.33 nC/bunch with a spacing of 2 cm. It is proposed to use this drive beam either to power the four 30 GHz modules that have been built for CTF2, or to drive a high-power RF test stand (see later) for the testing of prototype CLIC components. To be able to produce sufficient power to generate the nominal CLIC accelerating gradient of 150 MV/m with only 35 A requires a slightly modified power extraction structure which couples more strongly to the beam, so four new power extracting structures will have to be built. After deceleration from an initial energy of 184 MeV to a final energy of 125 MeV the drive beam is sent to a dump. There is space in the modules for eight 86-cell 30 GHz accelerating structures with the potential to accelerate a beam from 150 MeV to 510 MeV. The main beam to probe the accelerating fields generated will be produced by a photo-injector which will be able to run in either a single-bunch or a multi-bunch mode. In the multi-bunch mode there will be about 50 short bunches of about 0.64 nC/bunch (the exact number of bunches will be determined by beam loading considerations). One of the two CTF2 RF guns can be used for the photo-injector but a new laser and pulse train generator will be required. The beam will be accelerated to an energy of ~150 MeV by four 4.5 m long LIL accelerating sections operating at a gradient of about 9 MV/m. When operating with the 30 GHz modules, a single-bunch main beam will be used because the constant impedance sections are not designed for multi-bunch operation.

High-power RF test stand

It is proposed to operate a high-power RF test stand driven by the CTF3 beam in series with the four 30 GHz modules (see Fig. 5.3). The test stand would be a highly flexible experimental facility with a 1–2 m long test bed to measure a wide range of CLIC prototype components quickly, easily and accurately. This is in contrast to the modules where integration of prototype components into the very compact layout would always be problematic. The

test stand would require instrumentation to allow precise measurements of beam energy spectra, beam profiles before and after interaction with RF structures, transverse wakefields (if feasible), RF power, dark-current spectra and X-ray emission.

Preliminary beam tests using the LIL/EPA complex

It is proposed to use the LIL/EPA complex to carry out preliminary beam combination tests at very low currents as a first-stage CTF3. The transformation of the LIL/EPA complex into CTF3 would be carried out progressively. Recent studies and experiments have shown [5.6] that the EPA lattice can be modified (without making any hardware changes) to make it isochronous. It is foreseen to use the complex with small modifications to try out the (×5) beam combination scheme. The idea is to combine five short (6 ns) pulse trains spaced at a distance equal to the circumference of EPA (~125.6 m or 420 ns) into a single 6 ns pulse. The total pulse train length is 2.1 μs. The initial bunch spacing will be 10 cm (3 GHz) and after the combination will be 2 cm (15 GHz). The combination will only be possible with very low pulse currents (0.3 A), the limitation being beam loading in LIL. The beam energy (~350 MeV) will be higher than that for CTF3 (~184 MeV) and should therefore make operation somewhat easier. To produce five useable pulses at a spacing of 420 ns will, however, require a major modification of the present LIL gun pulse-forming network. The new gun foreseen will be able to deliver seven pulses in order to take into account the transient beam loading in the structures and get five pulses for recombination into EPA. In the next stage, longer pulses and higher currents will be possible when the new CTF3 linac is installed. This will again require either major modifications to the present injector or a new injector. Operation of this first-stage facility would enable the RF deflectors and RF diagnostic equipment to be tried out and debugged, and should result in an earlier first demonstration of the overall scheme, albeit at a low current. The fast switching of the subharmonic buncher between even and odd RF buckets is only required when the delay line combiner is installed. Until this moment CTF3 will operate with one bunch every 3 GHz RF bucket and in consequence one-half of the nominal charge (the nominal current is always constant at 3.5 A).

5.3 CLIC1 – A single-drive-beam unit

Although quite a number of issues concerning the technical feasibility of the CLIC scheme can be addressed with CTF3, a full-scale prototype (CLIC1) to test one complete CLIC drive train will almost certainly be required before the community is convinced that the overall scheme will work. A layout of CLIC1 is shown in Fig. 5.6.

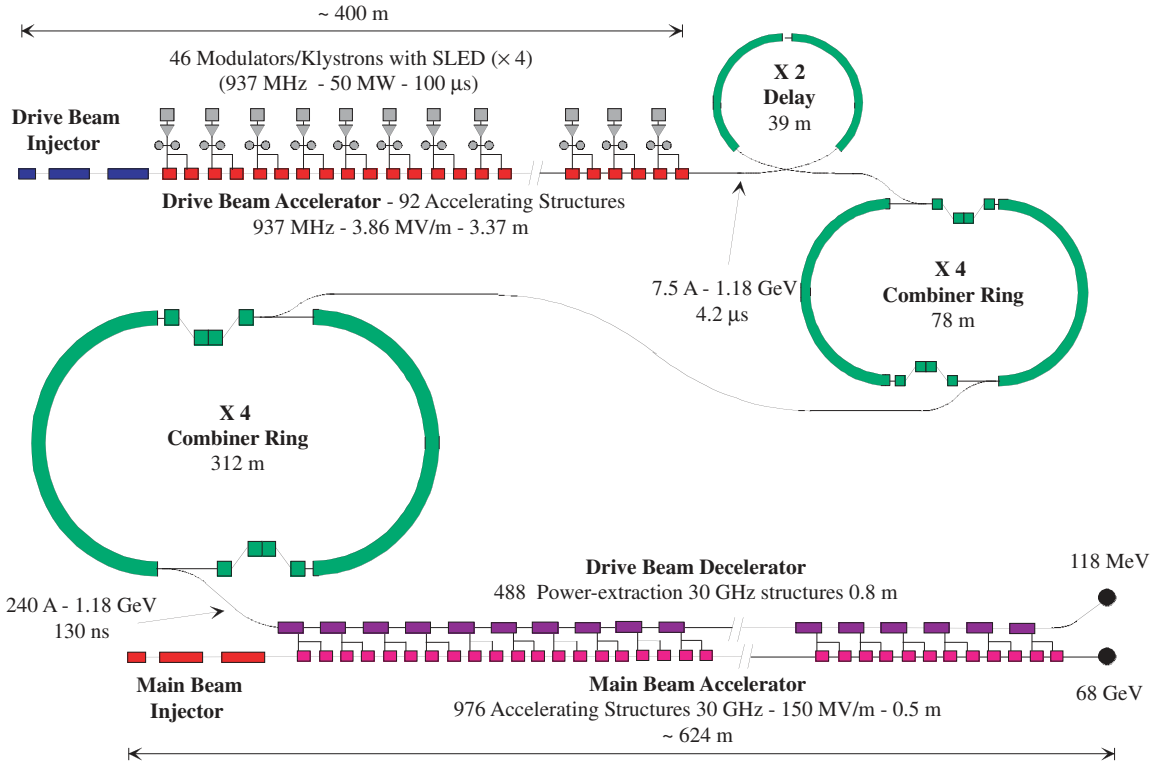

Fig. 5.6: *Schematic layout of CLIC1.*

The drive-beam generator for CLIC described above will produce 22 drive trains per linac for a 3 TeV centre-of-mass collider. All major problems associated with this scheme can, however, be studied by generating only one drive train. To obtain the nominal beam energy with only 46 klystrons installed requires building forty-six 937 MHz RF power compressors (these compressors are not required for the final CLIC scheme). Klystrons working with a much reduced RF pulse (~25 μs) could be used at this stage instead of the CLIC nominal value of 100 μs. This first-phase CLIC installation would produce beams with the nominal current and would be able to accelerate a multibunch beam to 68 GeV at the nominal accelerating gradient of 150 MV/m. CLIC1 and CLIC (3.0 TeV) drive-beam parameters are compared in Table 5.2.

References

[5.1] K. Aulenbacher et al., Results from the CLIC Test Facility (CTF1), CERN/PS/96-28 (LP) and CLIC Note 310 (1996).

[5.2] H.H. Braun for the CTF Team, Experimental results and technical research and development at CTF2, Proc. 7th Eur. Part. Accel. Conf. (EPAC2000), Vienna, 2000.

[5.3] CLIC Study Team, Proposals for future CLIC studies and a new CLIC Test Facility (CTF3), CLIC Note 402 (July 1999).

[5.4] H. Braun, W. Wuensch, I. Wilson and M. Luong, A very high gradient test of a 30 GHz single cell resonant cavity, Proc. 7th Eur. Part. Accel. Conf. (EPAC2000), Vienna, 2000.

[5.5] E.T. D'Amico and G. Guignard, Tunable achromats and CLIC applications, Proc. 7th Eur. Part. Accel. Conf. (EPAC2000), Vienna, 2000.

[5.6] R. Corsini, J.-P. Potier, L. Rinolfi, T. Risselada and J.C. Thomi, First micro-bunch measurements in EPA as isochronous ring at 500 MeV, PS/LP Note 99–03 (MD) (1999).

Appendix
Parameter summary and general layout of the CLIC complex

Table A.1: CLIC parameters associated with the main beam at various energies

			Centre-of-mass energy (TeV)			
Parameter	**Symbol**	**Unit**	**0.5**	**1**	**3**	**5**
Beam at IP						
Luminosity (with pinch)	L	(10^{34} cm $^{-2}$ s^{-1})	1.4	2.7	10.0	10.0
Luminosity (in 1% of energy)	$L_{1\%}$	(10^{34} cm^{-2} s^{-1})	1.0	1.5	3.0	2.4
Beamstrahlung mom. spread	δ_B	(%)	4.4	11.2	31	36.6
Beamstrahlung parameter	Υ	(–)	0.3	1.0	8.1	18.8
No. of photons/electron	N_γ	(–)	0.7	1.1	2.3	3.2
Linac repetition rate	f_{rep}	(Hz)	200	150	100	50
No. of particles/bunch	N_b	(10^9 e$^{\pm}$)	4.0	4.0	4.0	4.0
No. of bunches/pulse	k_b	(–)	154	154	154	154
Bunch spacing	Δ_b	(cm)	20	20	20	20
Transverse emittances	$\gamma\varepsilon_{x/y}$	(10^{-8} rad·m)	200/2	130/2	68/2	78/2
Beta functions	$\beta_{x/y}$	(mm)	10/0.15	10/0.15	8/0.15	6/0.15
r.m.s. beam size (no pinch)	$\sigma_{x/y}$	(nm)	202/2.5	115/1.75	43/1	31/0.78
Bunch length	σ_z	(μm)	30	30	30	25
Enhancement factor	H_D	(–)	1.81	1.86	2.24	2.53
Beam power per beam	P_b	(MW)	4.9	7.4	14.8	12.3
Main linac						
RF frequency of main linac	$\omega/2\pi$	(GHz)	30	30	30	30
Acceleration field (loaded)	G_a	(MV/m)	150	150	150	172
Energy overhead	ovh	(%)	8	8	8	8
Active length per linac	L_A	(km)	1.74	3.54	10.74	15.64
Total length of two linacs	L_{tot}	(km)	5	10	27.5	40
RF power at section input	P_{st}	(MW)	229	229	229	301
No. of drive beams/linac	N_D	(–)	4	8	22	32
No. of structures per linac			3470	7070	21470	31282
AC-to-RF efficiency	η_{RF}^{AC}	(%)	40.3	40.3	40.3	40.3
RF-to-beam efficiency (incl. ovh)	η_b^{RF}	(%)	24.4	24.4	24.4	21.3
AC-to-beam efficiency	η_b^{AC}	(%)	9.8	9.8	9.8	8.5
AC power for RF generation	P_{AC}	(MW)	100	150	300	290

Table A.2: Parameters associated with the RF power source for the 3 TeV CLIC

Parameter	Symbol	Value
Main linac		
C.M. energy	E_{CM}	3 TeV
Gradient	G_{main}	150 MV/m
Total length/linac	L_{tot}	13.75 km
Frequency	ν_{RF}	30 GHz
Repetition rate	f_{rep}	100 Hz
Bunch charge	Q_{main}	0.64 nC
No. of bunches/pulse	N_{main}	154
Bunch separation	Δ_{main}	0.67 ns
RF pulse duration (flat-top)	$\tau_{\mathrm{RF,ft}}$	102 ns
RF pulse duration (FWHH)	$\tau_{\mathrm{RF,FWHH}}$	130 ns
RF peak power/structure	P_{RF}	229 MW
No. of structures/linac	$N_{\mathrm{struct,main}}$	21470
Total RF peak power/linac	$P_{\mathrm{RF,tot}}$	4.92 TW
Total RF energy/pulse	$W_{\mathrm{RF,tot}}$	602 kJ
Drive-beam (in the accelerator)		
Energy	$E_{\mathrm{fin,acc}}$	1.18 GeV
Current	I_{acc}	7.5 A
Bunch charge (max.)	Q_{b}	16 nC
No. of bunches/pulse	$N_{\mathrm{b,acc}}$	42944
Bunch separation	$\Delta_{\mathrm{b,acc}}$	2.13 ns
Pulse duration	τ_{pulse}	91.6 µs
Total charge	Q_{total}	688 µC
Total energy	W_{tot}	812 kJ
Average beam power	$P_{\mathrm{acc,ave}}$	81 MW
Drive-beam (in the decelerator)		
Energy (initial)	$E_{\mathrm{in,dec}}$	1.18 GeV
Energy (final)	$E_{\mathrm{fin,dec}}$	118 MeV
Current	I_{dec}	240 A
Bunch charge (max.)	$Q_{\mathrm{b,dec}}$	16 nC
No. of bunches/train	$N_{\mathrm{b,dec}}$	1952
Bunch separation	$\Delta_{\mathrm{b,dec}}$	0.067 ns
Train duration (FWHH)	τ_{train}	130 ns
Train number	N_{trains}	22
Charge/train	Q_{train}	31.25 µC
Total energy/train	W_{train}	36.9 kJ
Average beam power	$P_{\mathrm{dec,ave}}$	3.7 MW
Drive-beam accelerator		
Length (active)	L_{acc}	306 m
Frequency	ν_{acc}	937 MHz
Loaded gradient	G_{acc}	3.86 MV/m
Structure length	$L_{\mathrm{struct,acc}}$	3.4 m
No. of structures	$N_{\mathrm{struct,acc}}$	91
Shunt impedance	r'_{acc}	1214 Ω/m (linac)
Quality factor	Q_{acc}	26660
Group velocity	$\beta_{\mathrm{g,acc}}$	0.039 c
Filling time	τ_{fill}	288 ns
Power/structure	P_{acc}	100 MW
RF pulse duration	τ_{acc}	91.6 µs

Parameter	Symbol	Value
Drive-beam decelerator		
No. of units	N_{unit}	22
Unit length (total)	$L_{\mathrm{unit,tot}}$	624 m
Unit length (active)	$L_{\mathrm{unit,act}}$	390 m
No. of PETS/unit	$N_{\mathrm{PETS,unit}}$	488
Decelerating gradient	G_{dec}	2.8 MV/m
PETS length (active)	L_{PETS}	0.8 m
PETS shunt imp.	r'_{PETS}	41 Ω/m (linac)
Group velocity	$\beta_{\mathrm{g,dec}}$	0.441 c
Drain time	τ_{drain}	3.4 ns
Efficiency (%)		
Modulators	η_{M}	90
Klystrons	η_{K}	65
DB acceleration	$\eta_{\mathrm{D,acc}}$	93
DB power extraction	$\eta_{\mathrm{D,extr}}$	82
PETS extraction	η_{PETS}	95
PETS to CAS transfer	η_{transf}	95
Wall-plug-to-RF	$\eta_{\mathrm{plug,RF}}$	40.3
RF-to-main-beam (with 8% overhead)	$\eta_{\mathrm{RF/main}}$	24.4
Wall-plug-to-main	η_{tot}	9.8

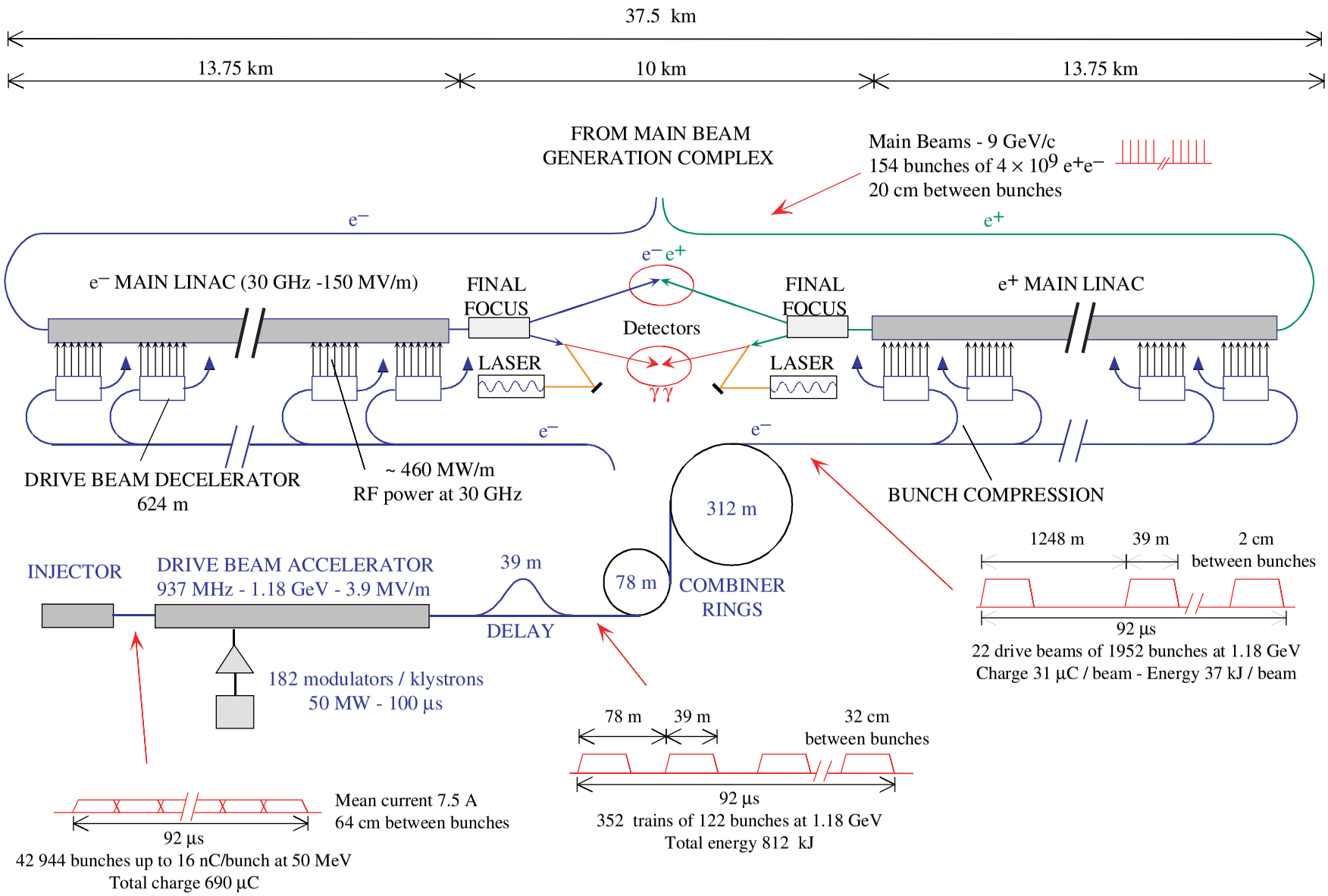

Fig. A.1: *Overall layout of the CLIC complex at 3 TeV centre of mass.*